AFSWC-TR-61-82

SWC
TR
61-82

HEADQUARTERS
AIR FORCE SPECIAL WEAPONS CENTER
AIR FORCE SYSTEMS COMMAND
KIRTLAND AIR FORCE BASE, NEW MEXICO

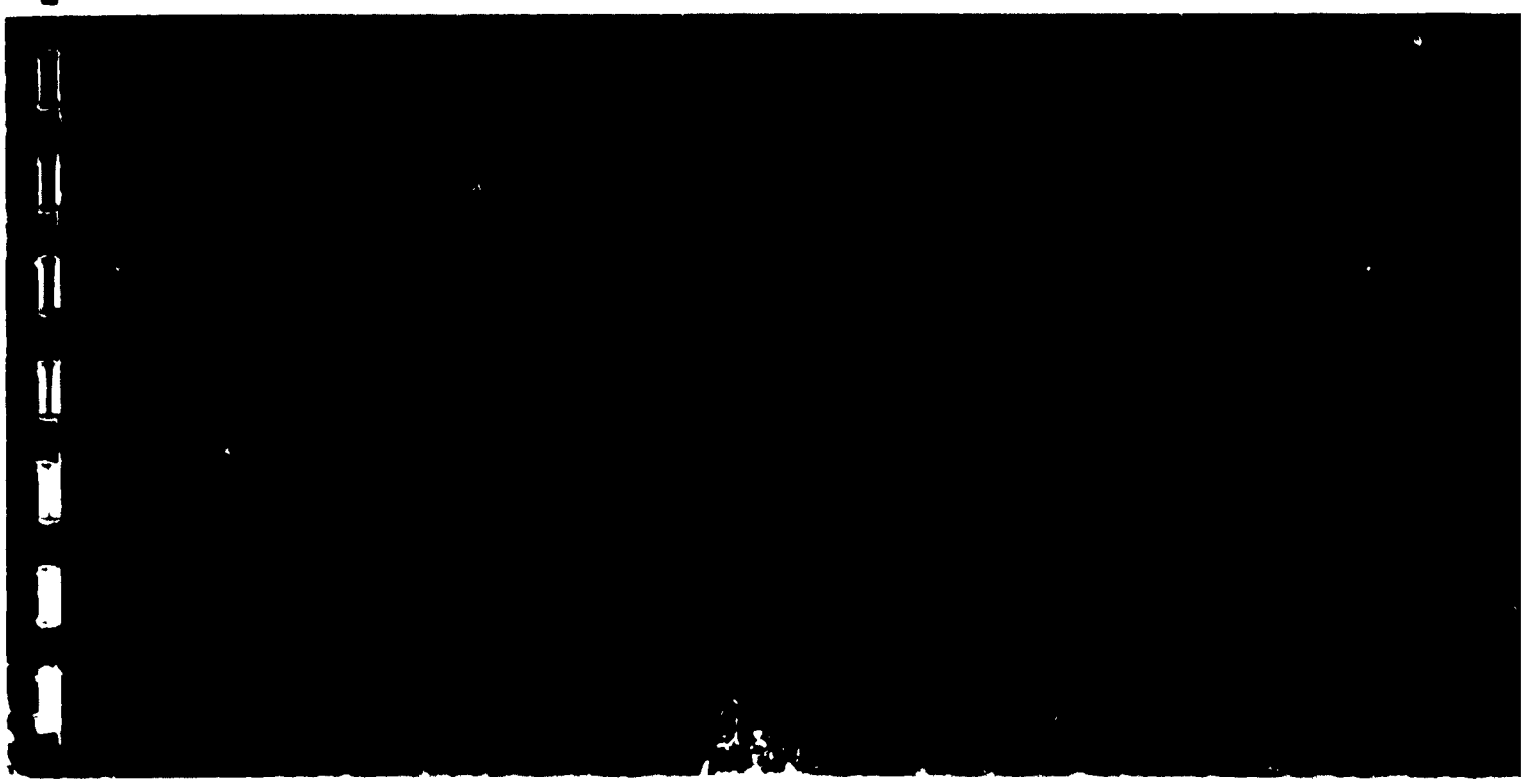

AFSWC-TR-61-82

Final Report

ANALYSIS OF JASON DATA

October 1961

Lockheed Aircraft Corporation
Missiles and Space Division
Sunnyvale, California

Research Directorate
AIR FORCE SPECIAL WEAPONS CENTER
Air Force Systems Command
Kirtland Air Force Base
New Mexico

Approved:

DONALD I. PRICKETT
Colonel USAF
Director, Research Directorate

Project 7811
Task 781106
Contract AF 29(601)-2862

ABSTRACT

This report describes recent investigations of the data obtained by the Jason sounding rockets during the Argus tests. These instrumented rockets detected electrons which were injected into the geomagnetic field by the detonation of nuclear devices at high altitudes. The original analysis of the data has been published in the open literature; the further investigations reported here yielded: (1) the orientations of the detectors with respect to a plane perpendicular to local magnetic lines of force, (2) the calibration of the detectors in a planar flux of electrons as functions of electron energy and orientation of the detectors with respect to the electron plane, and (3) a re-evaluation of the Jason data based on items (1) and (2) and on recent data on characteristics of the natural radiation. The conclusions verified the results of the initial analysis regarding the location, width, and stability of the electron "shell" produced by the Argus II detonation, as well as the presence of a less intense electron flux in wide regions (wings) away from the shell. A point of departure was that the electron spectrum was much more in agreement with the fission beta spectrum than that resulting from the initial analysis. Within the accuracy of the data, the spectrum was found to be independent of the spatial locations of the rockets or of the passage of time. The decay of the flux appears to follow a time dependence of $t^{-1.15\pm.03}$, and a lower limit to the injection efficiency appears to be 0.013.

PUBLICATION REVIEW

This report has been reviewed and is approved.

John J. Dishuck

JOHN J. DISHUCK
Colonel USAF
Deputy Chief of Staff for Operations

CONTENTS

CONTENTS

LIST OF ILLUSTRATIONS

LIST OF ILLUSTRATIONS

LIST OF ILLUSTRATIONS

LIST OF TABLES

1. INTRODUCTION

The Jason data refer to the information on the geomagnetic trapping of electrons obtained by sounding rockets during the Argus tests. These instrumented rockets detected electrons which were injected into the geomagnetic field by the detonation of nuclear devices at high altitudes. Project Jason was directed by the Air Force Special Weapons Center, and personnel of the Physics Division of the AFSWC performed the initial analysis of the data.[1]

A more thorough analysis of these data, however, was dictated by the military and geophysical importance of the Argus experiment and the restriction on the continuation of similar experimental investigations. In particular, analytical work was needed to compute the body motions of the rockets in free flight in order to correlate the counting rates of the detectors with the orientations of the detectors. Also, experimental work was required to determine the response of each detector as a function of electron energy and as a function of the orientation of the detector with respect to the distribution of the electron flux. By establishing these essential characteristics of the measurement system, and also by utilizing relatively recent information[2] on the spectral and spatial properties of the natural radiation, a better deduction of the results of the Argus experiment was expected.

This further analysis of the Jason experiment is given in this report.

1.1 REVIEW OF EXPERIMENT

In the Jason program, nineteen four-stage solid-propellant rockets were launched from Wallops Island, Virginia, Cape Canaveral, Florida, and Ramey Air Force Base, Puerto Rico. Table 1-1 gives a summary of the rocket program.

---

1. "Project Jason Measurement of Trapped Electrons from a Nuclear Device by Sounding Rockets," by Lew Allen, Jr., James L. Beavers II, William A. Whitaker, Jasper A. Welsh, Jr., and Roddy B. Walton, Proceedings of the National Academy of Sciences, August 1959; and Journal of Geophysical Research, 64, 893, 1959.

2. "Energy Spectrum and Angular Distributions of Electrons Trapped in the Geomagnetic Field," by J. B. Cladis, L. F. Chase, W. L. Imhof, and D. J. Knecht, Journal of Geophysical Research, 66, 2297, 1961.

TABLE I-I

Launch coordinates for the Jason Flights were: Wallops (75°29'W, 37°50'N); Partick (80°32'W, 28°27'N); Ramey (67°7'W, 18°32'N)

EVENT/FLIGHT	LAUNCH SITE	DATE	After Burst (Launch Time) hr:min	PERFORMANCE	APOGEE, KM	SPLASH LATITUDE	SPLASH LONGITUDE
Pacific I	Johnston I	1 Aug	..	..	..	..	.
Pacific II	Johnston II	12 Aug	..	..	..	..	..
1822	Patrick	15 Aug	65:46	OK	693	27.91°N	76°49'W
1841	Ramey	20 Aug	182:57	Failure	..	..	..
1859	Wallops	25 Aug	319:43	Failure	..	..	..
Event 1	..	27 Aug	..			..	..
1909	Patrick	27 Aug	1:03	OK	937	30.62	74.01
1914	Ramey	27 Aug	1:54	Failure	..	..	..
1917	Ramey	27 Aug	4:12	OK	817	25.40	68.49
1913	Wallops	27 Aug	4:59	Failure	..	..	..
Event 2		30 Aug	..	..	..	..	..
2019	Wallops	30 Aug	0:28	OK	817	29.90	74.88
2022	Patrick	30 Aug	1:11	OK	878	28.19	70.21
2021	Wallops	30 Aug	1:58	OK	830	31.51	80.30
2023	Ramey	30 Aug	2:32	OK	825	25.51	70.86
2025	Patrick	30 Aug	3:16	OK	699	27.32	70.52
2024	Wallops	30 Aug	4:01	OK	815	27.56	72.56
2027	Wallops	30 Aug	18:42	OK	745	30.08	71.08
2026	Ramey	30 Aug	19:43	Failure	..	..	..
2020	Patrick	31 Aug	20:47	OK	800	25.96	67.47
2041	Ramey	2 Sep	87:42	Failure	..	..	..
2042	Wallops	2 Sep	88:43	OK	739	29.61	70.19
2043	Patrick	2 Sep	90:55	OK	789	27.96	67.27

Rockets which performed properly generally reached altitudes of 700 to 800 km. Six of the rockets failed to operate as planned. Ten of the remaining rockets were launched successfully following the second nuclear detonation. Of these, only the five rockets which were launched from Wallops Island, Virginia, traversed the electron shell. These rockets were launched at time intervals after the burst ranging from 28 minutes to about 89 hours.

The radiation-detection instruments consisted of eight geiger tubes with various absorbers and collimators. A diagram of the instrumentation package is shown in Figure 1-1. The detectors in Channels 1, 5, 7, 3, and 6 are referred to in the text as the long detectors. Each of these detectors utilized the same type of geiger tube, an Anton 106-C. Of these, only the detectors in Channels 1 and 5 were rather highly collimated, as shown in Figure 1-1. The detectors in Channels 2, 8 and 4 are referred to in the text as the short detectors. These also utilized a single geiger tube type, but it was an end-window Anton 222R. All of the 222R detectors were highly collimated, each in the manner shown for the detector of Channel 2 in Figure 1-1. Roughly, the absorbers were selected such that the detectors in Channels 7 and 8 had thresholds at about 440 kev; the detectors in 3 and 4 had threshold energies of about 1 Mev, and the detector in Channel 6 was alone with a threshold energy of 4.3 Mev. The detectors are described more fully in Section 3.

The output pulses of the geiger tubes were sequentially sampled for a time duration of about 1/75 sec with a multi-segment commutator, and the pulses were transmitted directly to ground stations. In the telemetry records, regularly spaced synchronization pulses appeared, followed by pedestal-shaped signals, each of which corresponded to a sampling of the output of a particular detector. The geiger tube pulses appeared at the top of the pedestals. For each Channel, the counts per pedestal were determined visually by personnel of the Air Force Special Weapons Center and recorded as a function of time.

These data, together with the trajectories of the rockets and the telemetry signal strength records received by the six ground stations of the Air Force Missile Test Center range were used in this study.

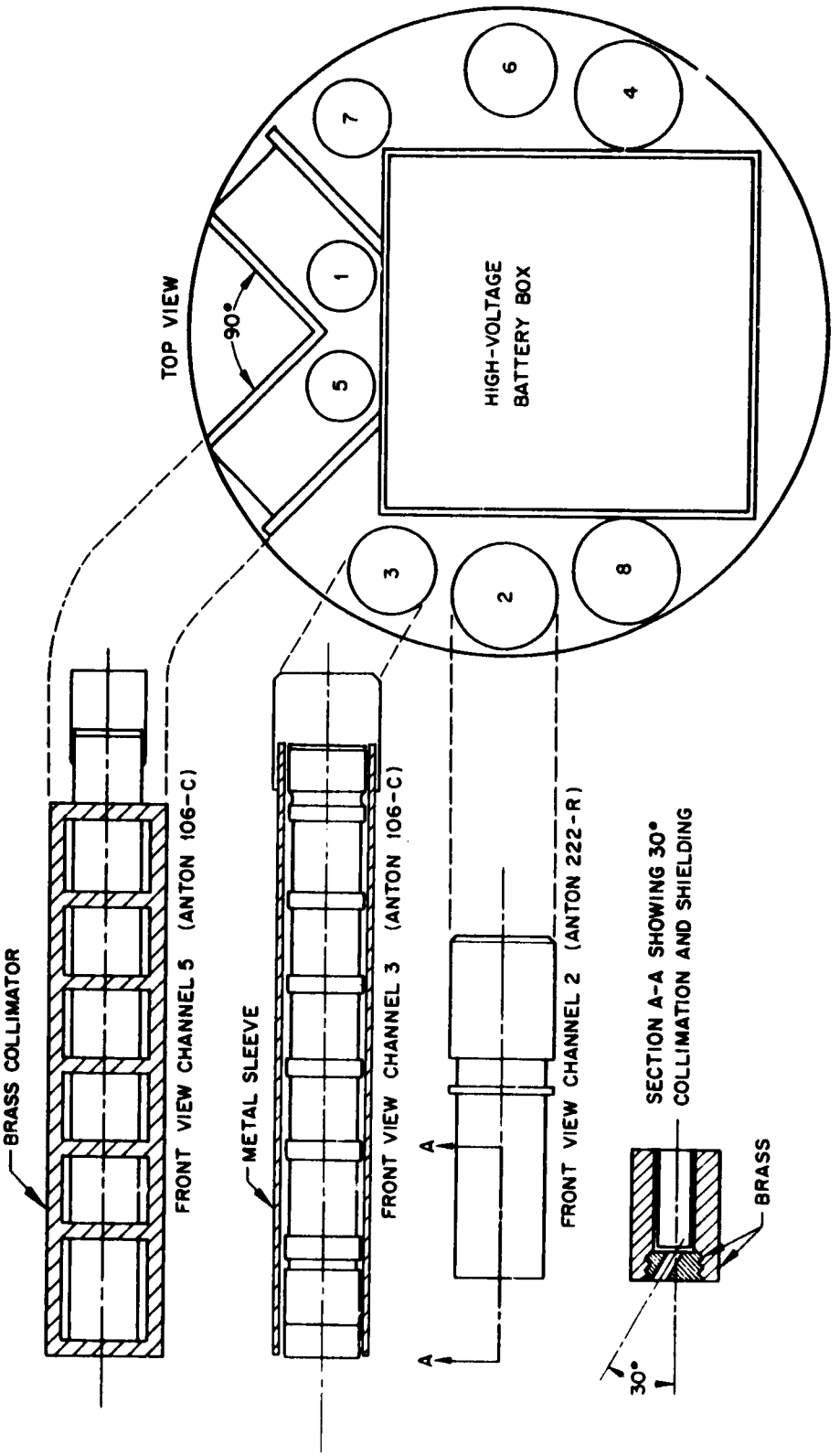

Fig. 1-1 Geiger Tube Instrumentation Package

1.2 GENERAL METHOD OF ANALYSIS

A correlation of the counting rates of the detectors with the orientation of the longitudinal axis of the rocket in space, as described in the following section, revealed that the distribution of the electron flux was symmetrical about a plane perpendicular to the local geomagnetic lines of force. Moreover, the angular "spread" of the electron paths about this plane (pitch-angle distribution) was found to be narrower than the angular apertures of the collimated detectors (half-angle at half-height of about 15^{o}).

It was unfortunate that the detectors were not collimated sufficiently to permit a measure of the pitch-angle distributions of the electrons and hence obtain the distribution of the flux along magnetic lines of force. But an initial experiment in an unknown area rarely yields all that is desired!

However, since the distribution of the electron flux about the normal plane fell within the collimation apertures of the detectors, the total flux and the spectrum of the electrons along the paths of the rockets could be determined by relating the counting rates and the response functions of the detectors to the orientation of the detectors with respect to this normal plane.

This method of analysis yields a planar flux; that is, a flux distribution such that the electron velocity vectors are uniformly distributed about every point in planes normal to geomagnetic lines of force but have no components out of these planes. If a planar flux is given in units of number $\cdot$ cm^{-2} $\cdot$ sec^{-1}, the numerical value of the flux equals the number of electrons/second which traverse a spherical detector of 1 cm^{2} cross sectional area. Since such a detector would be traversed by the same number of electrons per second if located in an omnidirectional flux numerically equal to that of the planar flux and given in the same units, the planar flux evaluated by the analysis discussed below is numerically identical to the omnidirectional flux. The plane of the flux (normal to geomagnetic line of force) is referred to in this report as the radiation plane.

Now, if the angles η and ψ are used to specify the orientation of a detector with respect to the radiation plane, then the corresponding geometric function of the detector will be defined by means of the equation,

$$R_i(\eta, \psi) = \int f(E) G_i(\eta, \psi, E) dE, \qquad (1\text{-}1)$$

where

$R_i(\eta, \psi)$ = corrected counting rate of geiger tube in Channel i, oriented at angles η and ψ to the radiation plane,

$f(E)$ = planar flux of electrons in units of number $cm^{-2} \cdot sec^{-1} \cdot Mev^{-1}$.

$G_i(\eta, \psi, E)$ = geometric function of detector in Channel i (units of cm^2 for detection of planar flux of electrons of energy E when oriented at angles ψ and η to the radiation plane. Note that G includes the detection efficiency of the geiger tube.

With the counting rates, R_i, correlated with η and ψ as described in the following section and the geometric function $G(\eta, \psi, E)$ determined experimentally as described in Section 3, the planar flux f(E) was "unfolded" with a digital computer from the integral equations (1-1). The computer program used to deduce the flux is described in Section 4.

A digital computer was used to correlate the counting rates, R_i, with the orientation angles η and ψ. These orientation angles were computed for each time at which a detector output was sampled. The read-out record from the computer listed the following information for each sampling of a detector output: the time of the sampling; the counts per pedestal; the corrected counting rate; and the orientation angles η and ψ. A "dead time" correction of 70 microseconds was applied to the counting rates. This "dead time" for the detection system was estimated from the time resolution of the geiger-tube pulses in the oscillograms from which the counts per pedestal were read.

The values of R_i used in Equations (1-1) were those which were averaged over certain intervals of time and angles η and ψ. This was done to improve the overall accuracy of the results.

2. BODY MOTIONS OF ROCKET IN FREE FLIGHT

The body motions of the rockets in free flight were determined by using both the counting rates of the detectors as a function of time and the antenna signal strength records. The analysis conducted to evaluate the time-dependent angles η and ψ which gave the orientation of each detector with respect to the radiation plane is described in the section below. In the following section, the evidence is given that this radiation plane was normal to the local geomagnetic lines of force.

2.1 ORIENTATION OF DETECTORS WITH RESPECT TO RADIATION PLANE

The analysis of the motions of the detectors with respect to the radiation plane will be described with reference to the diagram shown in Figure 2-1. Here, a sphere is depicted with its center at the center-of-mass of the rocket. The labelled dots on the sphere represent the points at which the following vectors intersect the surface of the sphere: $\bar{S}$ is aligned with the spin axis of the vehicle, $\bar{A}$ is the constant angular momentum vector, $\bar{B}$ is the local geomagnetic field vector, $\bar{C}$ is a vector in the plane normal to $\bar{S}$ and directed along the center of the angular apertures of the detectors in Channels 1, 3, 5, 6 or 7 (for the detectors in Channels 2, 4, or 8, $\bar{C}$ is along the projection of the collimator axis in the plane normal to $\bar{S}$). As shown in the diagram, θ is the angle between $\bar{A}$ and $\bar{B}$, η is the angle between $\bar{B}$ and $\bar{S}$, and ζ is the angle between $\bar{A}$ and $\bar{S}$. Three lines of nodes are also shown: $n(\bar{B},\bar{A})$ is drawn normal to $\bar{B}$ and $\bar{A}$, $n(\bar{B},\bar{S})$ is normal to $\bar{B}$ and $\bar{S}$, and $n(\bar{A},\bar{S})$ is normal to $\bar{A}$ and $\bar{S}$.

The vector $\bar{C}$ rotates in a clockwise sense about $\bar{S}$ with the constant angular velocity ω_s (spin rate). The angular displacement of $\bar{C}$ will be represented by $\Theta_s(t) = \omega_s t + d_s$, measured from the $\bar{S},\bar{A}$ plane. The spin axis $\bar{S}$ rotates in a cone about $\bar{A}$, in the clockwise sense, and with the constant angular velocity ω_p (precession rate). The angular displacement of the $\bar{A},\bar{S}$ plane will be designated by $\Theta_p(t) = \omega_p t + d_p$, measured from the node $n(\bar{B},\bar{A})$.

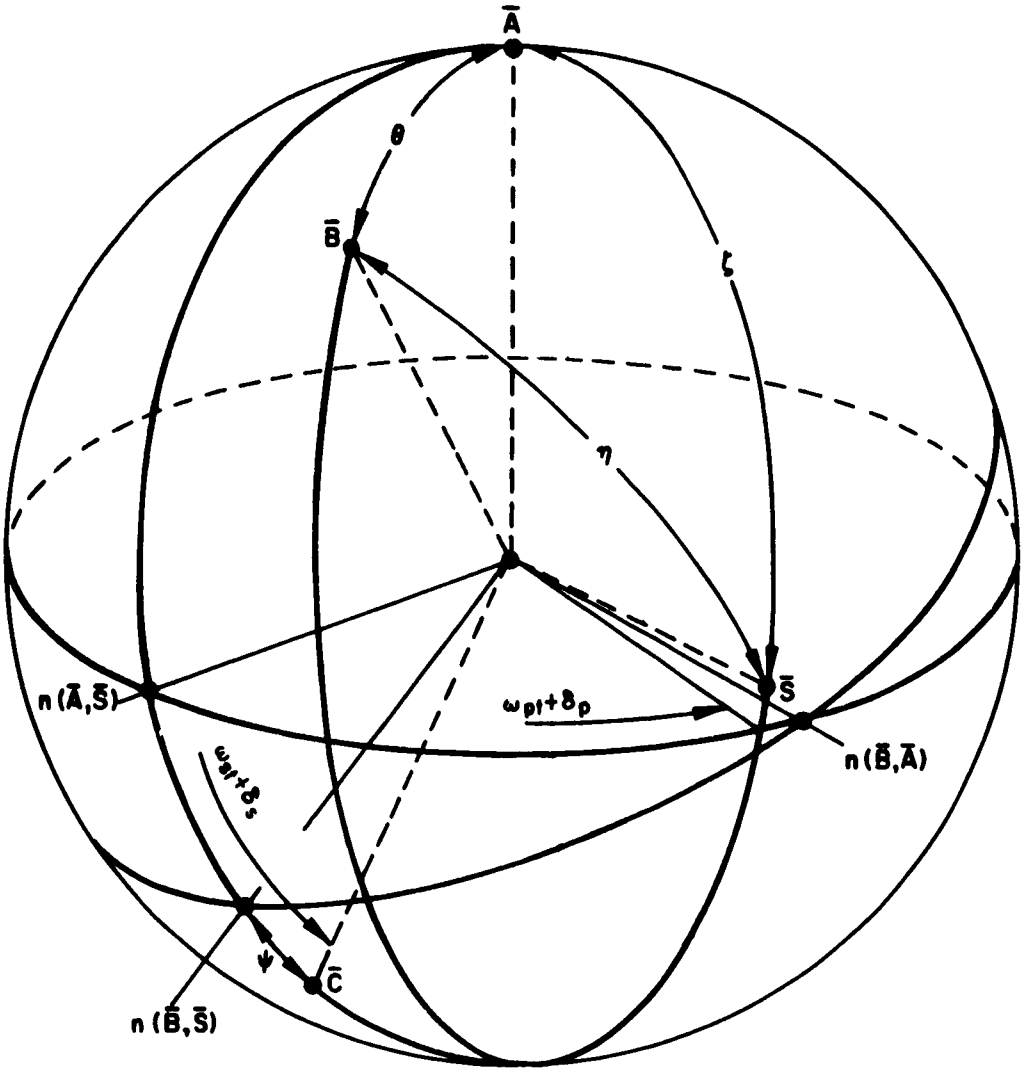

Fig. 2-1 Coordinate System for Determination of Rocket Motion From Geiger Tube Count Rate Data

From this diagram the following relationships can be obtained:

$$\cos\eta = \cos\Theta\cos\zeta - \sin\Theta\sin\zeta \sin(\omega_p + d_p), \quad (2\text{-}1)$$

$$\psi = \omega_s t + d_s - \nu(t), \text{ where} \quad (2\text{-}2)$$

$$\nu(t) = \pi - \tan^{-1}\left\{ \left[\sin\zeta \operatorname{ctn}\Theta + \cos\zeta \sin(\omega_p t + d_p)\right] \cdot \sec(\omega_p t + d_p) \right\} \quad (2\text{-}3)$$

Hence, the orientation angles η and ψ can be determined as functions of time by evaluating the constants ω_p, ω_s, d_p, d_s, Θ and ζ. Fortunately, not all of these constants are mutually independent. The interdependencies of these constants and the methods used to evaluate them are discussed below.

2.1.1 DETERMINATION OF PRECESSIONAL ANGULAR VELOCITY

The constant ω_p was determined from the telemetry signal strength information which was recorded by a number of ground stations. A rotation of $\bar{S}$ in a cone about $\bar{A}$ was discernable in the record because the signal strength varied in accordance with the aspect of the antenna pattern (quadrupole) to the receiving station. Hence, the period of precession, $T_p = 2\pi/\omega_p$, was given by the time duration of a recurrent modulation pattern in the record.

In order to avoid errors in this measurement due to a rapid azimuthal motion of the line-of-sight between the rocket and the ground station, the signal strength record of a station which was most nearly in the plane of the rocket trajectory was used. The records of six ground stations, located south of the rocket trajectory and spanning a longitude range from 80° 32' W (Patrick) to 61° 45' W (Antigua), were available for this purpose.

The examination of the signal strength records revealed that, for every flight except 2027, the precession period, T_p, was essentially constant over the entire portion of the trajectory above the "sensible" atmosphere of the

earth. The rocket on 2027 exhibited an appreciable diminution of rotational energy during the course of the flight: The precession period increased by nearly 1% and the spin period increased by about 20%. There is also some evidence of such a draft on Flight 2024, but the magnitude of the drift was smaller by an order of magnitude. A rough calculation indicates that the decrease of the rotational velocity of the vehicle in free flight was caused by the interaction of the geomagnetic field with the rotating conductive structures and components of the rocket, dissipating the rotational energy in the form of eddy currents.

The value of T_p given by this analysis are listed in the second column of Table 2-1.

TABLE 2-1

Flight No.	Precession Period, T_p (sec)	Spin Period, T_s (sec)	θ Degrees	ζ Degrees
2019	3.793 ± .001	4.861 ± .004	5 ± 2	89.5
2021	30.00 ± .02	6.654 ± .005	16.2 ± 1.5	87.1
2024	17.41 ± .01	1.97 ± .02	20.5 ± 1.6	84.5
2027	1.818 to 1.830	1.440 to 1.756	5 ± 3	89
2042	9.958 ± .003	4.292 ± .002	4 ± 2	88.5

2.1.2. DETERMINATION OF ROTATIONAL ANGULAR VELOCITY

The angular velocity, ω_s, of the rocket about its longitudinal axis, S, was obtained from the "radiation signal," defined as the curve obtained by plotting the counts per pedestal of a channel versus time. (Principally, Channels 1 and 5 were used for this purpose.) By measuring N, the number of cycles (including fractions of a cycle) of the radiation signal which occurred in an integral number, n, of precession periods, the value of ω_s was deduced from the relation,

$$\omega_s = (N/2n)\,\omega_p. \qquad (2\text{-}4)$$

This equation was appropriate because, for every rocket flight, the angle ζ was found to be greater than θ as described below. If ζ had been smaller than θ, then the equation,

$$\omega_s = (N/2n - 1)\,\omega_p, \tag{2-5}$$

would have been used.

The equations above can be verified in the following manner: Differentiation of Equation (2-2) with respect to time gives,

$$\dot{\psi} = \omega_s + \omega_p\,(\cos\zeta - \cos\theta\cos\eta)/\sin^2\eta\ . \tag{2-6}$$

Since ψ is measured from the radiation plane while $\omega_s t + d_s$ is in the first or second quadrants, as shown in Figure 2-1, $\dot{\psi}$ equals one-half the angular frequency of the radiation signal. Hence, the average value of over the integral number n of precession periods is,

$$\langle\dot{\psi}\rangle = (1/2)\cdot 2\pi\ N/nT_p$$

$$= (1/nT_p)\int_0^{nT_p}\left[\omega_s + \omega_p\,(\cos\zeta - \cos\theta\cos\eta)/\sin^2\eta\right]\,dt$$

By substituting in this equation the value of $\cos\eta$ given by Equation (2-1) and performing the integration, equations (2-4) and (2-5) can be obtained. (After substituting Equation (2-1) for $\cos\eta$, the second term in the integral above can be integrated by partial fractions.)

The measurements of the spin periods, $T_p = 2\pi/\omega_s$, of the rockets are listed in the third column of Table 2-1.

2.1.3 DETERMINATIONS OF θ AND ζ

In principle, three independent methods can be used to obtain the value of ζ, and two independent methods can be used to evaluate θ. First, the angle ζ can be evaluated by considering the vehicle to have the configuration of a "symmetrical" top. Then if R represents the ratio of the small to

the large principal moments of inertia of the vehicle, ζ is given by the equation

$$\cos \zeta = R \omega_s / \omega_p . \tag{2-7}$$

The angle ζ can also be determined by analyzing the signal strength records. This method is discussed in the following section. The angle θ can be obtained in this way by using available geomagnetic dip and declination information.

Finally, the angles ζ and θ, as well as the precessional phase angle, d_p, can be determined by measuring the time variation of the period of the radiation signal within a precession period. Equation (2-6) gives the time dependence of one-half the angular frequency of the radiation signal; it varies from a minimum value of

$$\dot{\psi}_{min} = \omega_s - \omega_p \sin \theta / \sin (\zeta - \theta) \quad \text{for } \omega_p t + d_p = - \pi/2, \tag{2-8}$$

to a maximum value of

$$\dot{\psi}_{max} = \omega_s + \omega_p \sin \theta / \sin (\zeta + \theta), \quad \text{for } \omega_p t + d_p = \pi/2. \tag{2-9}$$

Hence, a graph of the time interval between the peaks of the radiation signal gives the precessional phase angle, d_p, and the extreme values of $\dot{\psi}$. Equations (2-8) and (2-9) can then be solved simultaneously to yield θ and ζ.

Actually, the extreme values of $\dot{\psi}$ could not be measured sufficiently well to determine both ζ and θ with good accuracy. A graph of some of the measurements of the period of the radiation signal within a precession period of the rocket is shown in Figure 2-2. The time marked 0 on the abscissa corresponds to the time 0745 seconds recorded on the data read-out

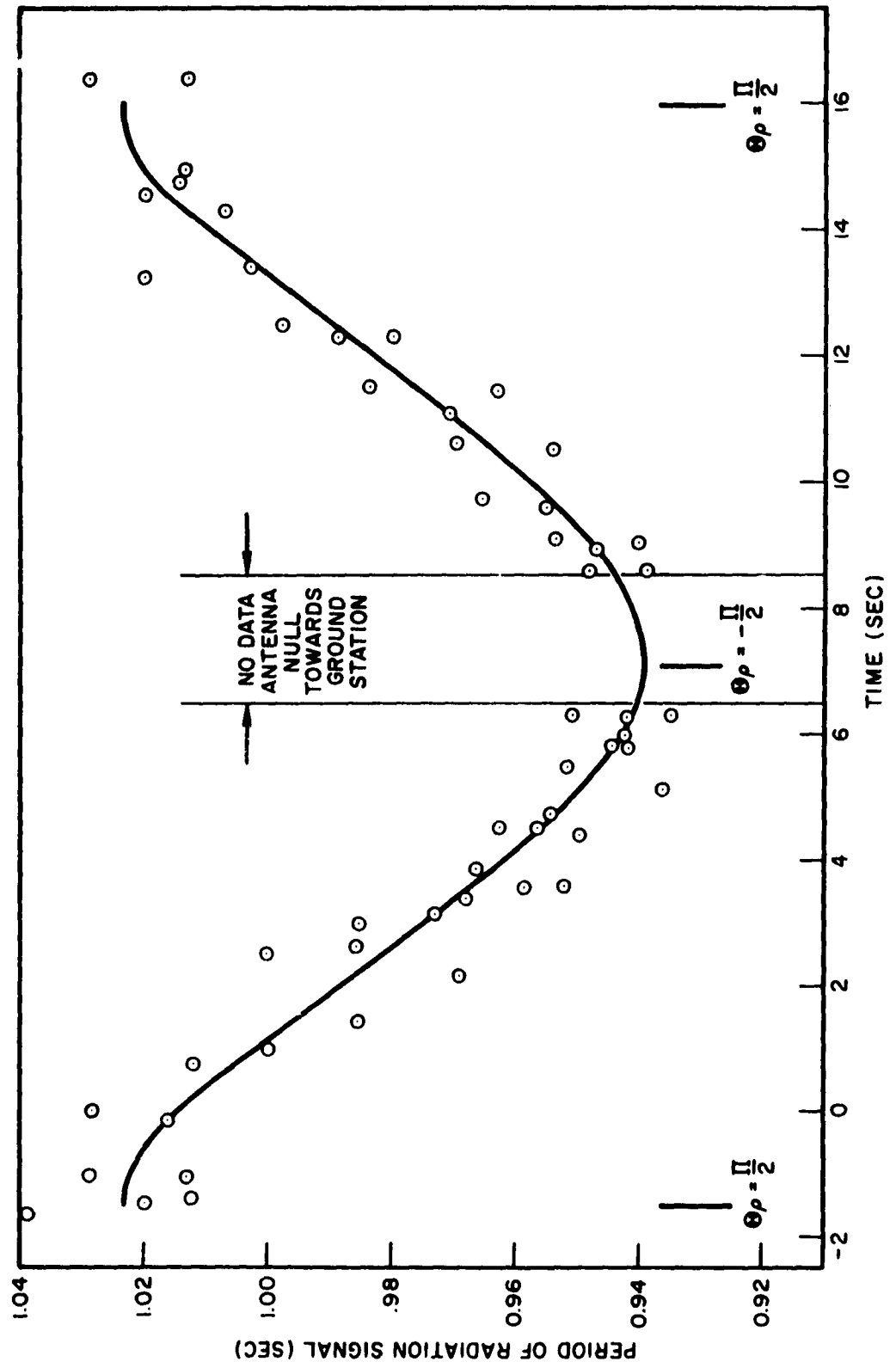

Fig. 2-2 Measurements of Period of "Radiation Signal" Within Precession Period of Rocket

sheets. From this point on, differences in the times of occurrence of the peaks were plotted against the time between the peaks given by the "read-out" time minus the sum of 0745 sec and an integral number of precession periods (17.41 sec.). The scatter of the measurements shown in the graph are representative of the data taken throughout the flight.

The value of ζ given by the signal strength analysis for flight 2024 agreed with the value of ζ given by Equation (2-7) to within 1°. The value R = 1/90 was used for the ratio of the moments of inertia. Therefore Equation (2-7) was used to compute the values of ζ for the other flights. These values are listed in the last column of Table 2-1.

For each of the flights 2021, 2024, and 2042, the angle Θ, listed in the fourth column of Table 2-1, was then obtained by averaging the values of Θ given by Equations (2-8) and (2-9). (The angle ζ computed as indicated above was used in these equations.) The extreme values of $\dot{\psi}$ were obtained by averaging over the entire flight the period measurements of the radiation signal which occurred at the appropriate times within the precession period.

On flights 2019 and 2027, the precession and rotation periods of the rocket were comparable in magnitude. Hence, the method used above to determine the $\dot{\psi}$ variation was not applicable. The following method was used to determine the values of Θ for these flights: Starting at a time T_o, where the counting rate of the detector in Channel 1 was high, each value of the counts per pedestal given in the data sheets was recorded against the time of occurrence of the pedestal minus the sum of T_o and an integral number of precession periods. The number of precession periods used in this subtraction was that which yielded a net time interval which was greater than zero but less than a full precession period. Also, the rotational angle was computed for each of these data points by multiplying the rotational angular velocity by the time of occurrence of the pedestal minus the starting time T_o. A deduction of 360° from the rotation-angle computations was made whenever a complete rotation was exceeded. After about 300 data points were recorded in this manner, the precession period was divided into 12 equal intervals of time, and the counts per pedestal which fell into each of these time intervals were plotted against the rotation angle corresponding to that data point. Each of

these graphs therefore yielded the contour of the radiation plane (actually the fold with the angular response of the detector) for a small angular range of the precession angle. Then a graph was prepared giving the rotational angle at which the peak of each of these distributions occurred versus the time increment of the precession period. This graph yielded a sinusoidal curve; the difference between the maximum and minimum values was equal to 2θ (strictly true only for $\zeta = 90^{\circ}$, see Figure 2-1).

A very small displacement of the peaks was observed in these distribution curves for the flights 2019 and 2027, and the resulting estimates of the angles θ are given in Table 2-1: (This method of analysis was verified by applying it to flight 2024.)

2.1.4 DETERMINATION OF PHASE ANGLES d_p AND d_s.

The precessional phase angles d_p were obtained by fitting the curve given by Equation (2-6), with the values of ζ and θ computed as indicated above, to the measurements of the periods of the radiation signal within a precession period. Such a curve is drawn to the data in Figure 2-2.

The rotational phase angle was determined for each group of data which were read-out consecutively (for each "roll" of data read), by preparing graphs of the counts per pedestal versus time. These phase angles were determined in this manner to avoid the large accumulative errors.

2.2 ROCKET ORIENTATION FROM ANTENNA RADIATION PATTERN

It was not necessary to use the telemetry signal strength records to get the orientation of the rocket with respect to the radiation plane, except for the determination of the precession period, as shown by the above analysis. These records were used, however, to establish the orientation of the radiation plane in space, and to verify the calculations, based on the above methods, of the angles which describe the motion of the spin axis of the vehicle.

Figure 2-3 depicts a right-handed coordinate system, x, y, z, whose origin is at the center of mass of the vehicle. The x-z plane lies in a meridian plane with the z-axis directed towards the local zenith and the x-axis towards the south. $\bar{V}$ represents a vector which points towards a particular ground receiving station. Its direction cosines with respect to the x, y, and z axes are designated by the symbols α , β , and γ , respectively. Again $\bar{A}$ and $\bar{S}$ represent the constant angular momentum vector and the spin axis of the vehicle; and ζ is the constant angular displacement of $\bar{S}$ and $\bar{A}$. The angular displacement of the $\bar{S}$, $\bar{A}$ plane from the node $n(\bar{A},Z)$ is given by the angle $\omega_p(t-t_o)$. The location of the node is given by the angle ϕ, measured from the x-axis, and K represents the angular displacement of $\bar{A}$ with respect to the z-axis.

Now, the intensity of the electromagnetic radiation recorded by the ground station during the time interval of a precession cycle depends on the inclination of the longitudinal axis of the vehicle with respect to $\bar{V}$. This angle will be represented by the symbol, χ . It is given by the equation,

$$\cos\chi = (\alpha\cos\varphi + \beta\sin\varphi)\sin\zeta\cos\omega_p(t-t_o) + (\alpha\sin\varphi - \beta\cos\varphi)\sin K \sin\left[(\cos^{-1}\sin\zeta\cos\ _p(t-t_o)\right] + \gamma\left[\cos\zeta\cos K + \sin\zeta\sin K\sin\omega_p(t-t_o)\right] . \quad (2\text{-}10)$$

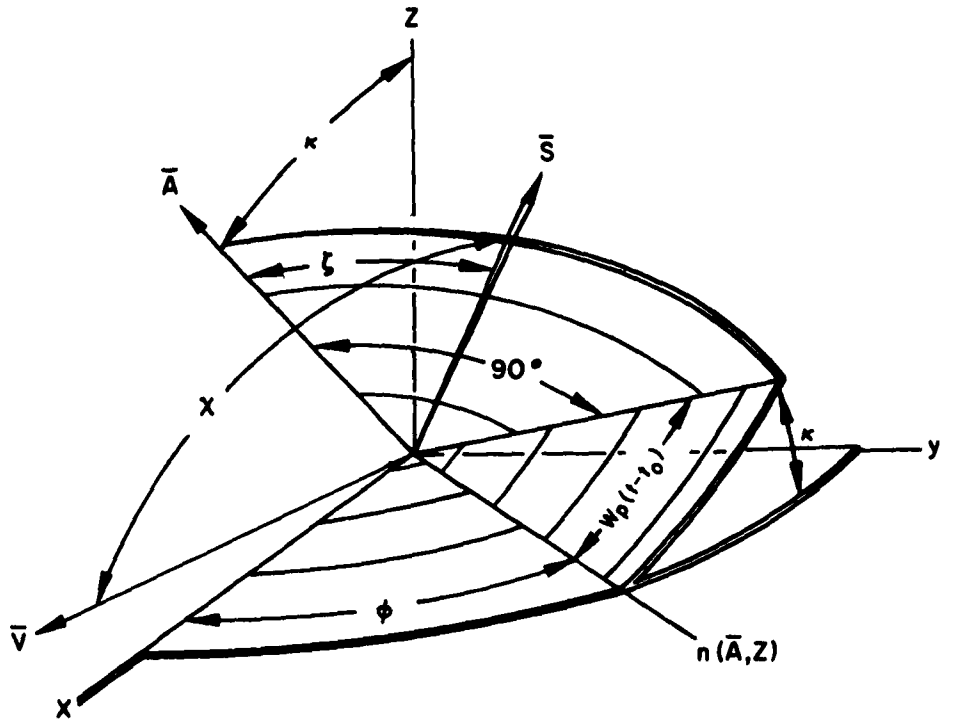

Fig. 2-3 Coordinate System for Determination of Rocket Motion From Antenna Signal Strength Data

The direction cosines, α , β , γ , can be computed from the known geographical locations of the ground stations and the rocket. A relationship between ζ and K be obtained as follows: By correlating the signal strength record received by a particular ground station with the antenna radiation pattern, χ can be determined as a function of time. Hence, an integration of cos χ (t) over a precession period t_p gives,

$$\int_{t_1}^{t_1 + T} \cos\chi(t)\ dt = \gamma T_p \cos\zeta \cos K ,$$

since the oscillatory terms of Equation (2-10) do not contribute to this integral.

Three additional equations are required to evaluate the constants ζ , K , φ , and t_o. These equations can easily be obtained by writing equations of the form of Equation (2-10) for each of three ground receiving stations, utilizing the times at which nulls occur (cos χ = 0) in the signal strength records of these stations.

An analysis of this type was conducted for Test 2024. By utilizing the magnetic dip and declination values, at the surface of the earth below the rocket, given by the Smithsonian Physical Tables, excellent agreement was obtained with the results given by the analysis described in Section 2.2. The angles Θ, ζ , and d_p calculated by these independent methods, were all in agreement to within 2 degrees. Therefore, at the positions of the rockets in space which were used in these analyses, the radiation plane was found to be perpendicular to the direction of the local geomagnetic field.

3. CALIBRATION OF DETECTORS

The geometric functions of the detectors, $G(E, \eta, \psi)$, described in Section 1 were determined by irradiating the detectors with an electron beam of known energy and intensity in a large vacuum chamber. A 180 degree beta-ray spectrometer was used to obtain a beam of monoenergetic electrons. With a SrY source at the spectrometer entrance, the output beam energy could be adjusted to any value up to about 2 Mev. The entire Jason instrumentation package was placed in the beam to take into account the scattering of electrons from exposed surfaces into detection channels. Although the electron beam was highly collimated, a combination of rotational and translational motions of each detector under calibration in the beam simulated the effect of a broad planar flux covering the extent of the detector. A special gimbal mechanism was constructed to support the instrumentation package at all possible spatial orientations. This mechanism facilitated the calibration of the detectors as functions of the angles η and ψ which give the orientations of the detectors with respect to the radiation plane.

The radiation plane was simulated by rotating the gimbal support mechanism on a turntable at constant angular velocity. To avoid twisting cables connected to the geiger tubes, the turntable motor was stopped and reversed in direction each time the geiger tube under calibration was rotated to an angular position where the collimation of the tube reduced its counting rate to zero. The "thickness" of the radiation plane was effectively extended to cover each long detector (Anton 106C geiger tube) by moving the tube through the beam along the long dimension of the collimator. This translational motion was provided during the calibration by a motor-driven carriage mounted on the gimbal support.

A translation of the Anton 222R geiger-tube detectors through the beam was not required because the collimator apertures of these detectors were smaller than the cross sectional area of the beam.

Figure 3-1 illustrates the manner in which the orientation angles η and ψ of the long detectors were adjusted in the laboratory. The angle η, which gives the displacement of the spin axis of the rocket from the local geomagnetic line of force, was adjusted by inclining the geiger tube axis to an angle $\pi/2 - \eta$ with respect to the horizontal plane (plane of the turntable). The angle ψ, which denotes the displacement of the "central-aperture" vector of the detector from the radiation plane, measured in a plane perpendicular to the spin axis of the rocket, was set in the laboratory by rotating the detector about the line L L. This line is shown in Figure 3-1. It is located in the entrance plane of the collimator, and it bisects the aperture along the long dimension of the collimator.

Figure 3-1 also depicts the proper relative locations of the beam, the turntable axis, and the geiger tube. As shown in the figure, they were arranged such that the line L L of the detector, the axis of the turntable, and the center-line of the beam intersected at the single point marked O. This point will be referred to as the central irradiation point.

Preparation for a calibration run consisted of adjusting the angles η and ψ, setting the beam energy E, and running the translation carriage to one of its extreme positions. (The detector was out of the beam at the extreme positions of the carriage.) The run was begun by turning on a scaler which recorded the geiger tube pulses and a special electronic unit which controlled the rotational and translational motions of the detector. The motions were fully automatic, with the carriage advancing a small distance Δ S along line L L for each rotation of the turntable. After the carriage traversed the beam and reached its other extreme position, the detector motions were stopped and the scaler was turned off automatically. The total number of counts, C_T, accumulated during the run was recorded. To obtain the background counts, C_B, the run was repeated with the beam off (zero magnet current).

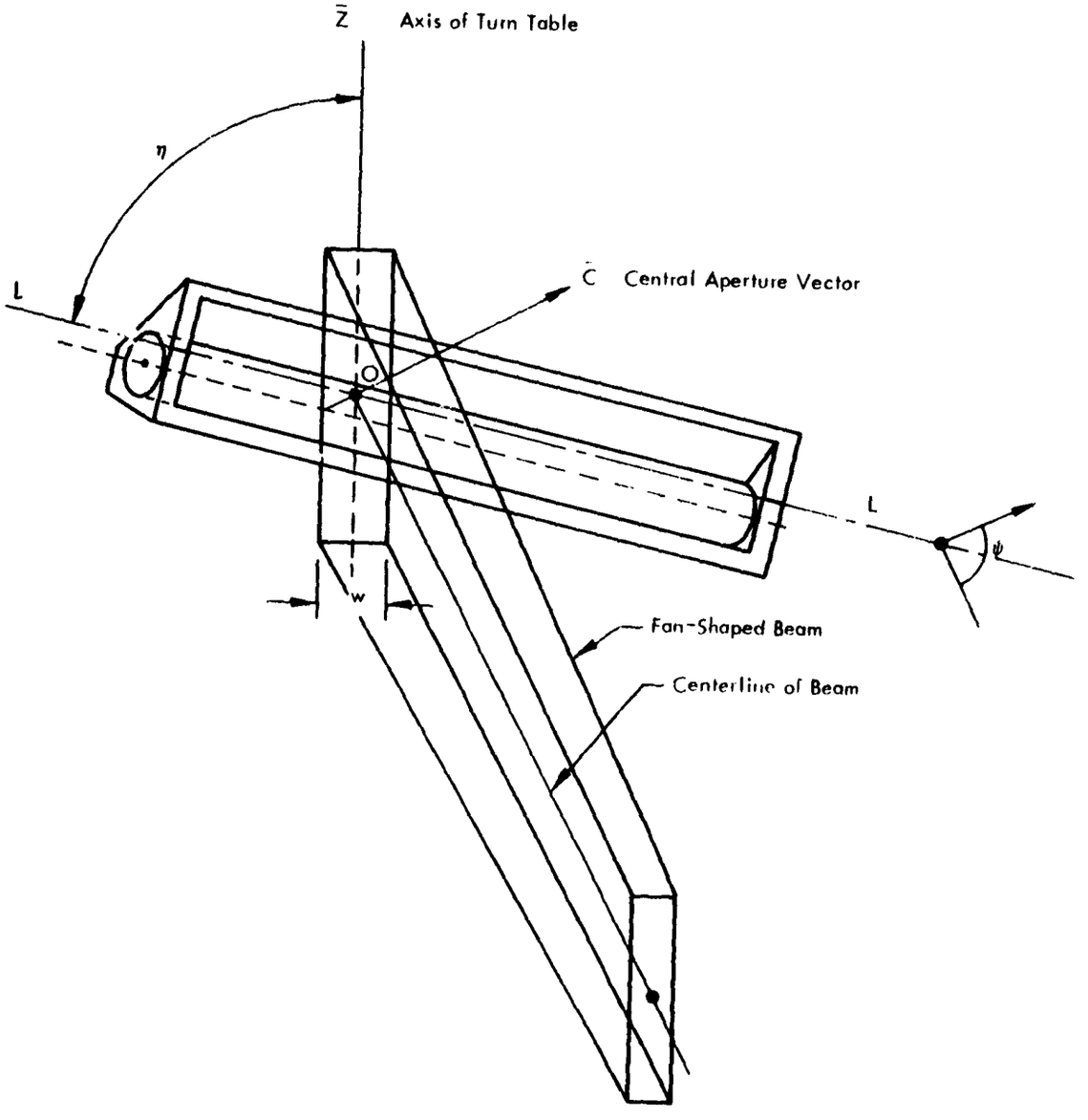

Fig. 3-1 Schematic Diagram Showing Orientation of Detector in Electron Beam. The dashed line LL is the axis about which the detector is rotated to determine the ψ -angle response. This line bisects the collimator of the detector in the entrance plane as shown

The geometric function was then computed by means of the equation,

$$G(\eta, \psi, E) = \frac{\Delta S \cos \eta}{w} \cdot \frac{(C_T - C_B)}{I(E)T} , \qquad (3\text{-}1)$$

where

ΔS = linear displacement of detector per rotation of turntable

w = width of beam

C_T = total counts during run

C_B = background counts

$I(E)$ = electron beam intensity (number . cm^{-2} . sec^{-1})

T = period of rotation of turntable

This equation can easily be derived formally, but it is somewhat more direct and instructive to verify the equation purely on the basis of physical considerations. In Section 1 the geometric function of a detector was defined by the equation,

$$R(\eta, \psi) = \int G(\eta, \psi, E)\, f(E)\, dE, \qquad (3\text{-}2)$$

where $R(\eta, \psi)$ is the counting rate of the detector oriented at angles η and ψ to a planar flux $f(E)$. The function G has units of cm^2 when $f(E)$ is given in units of number • cm^{-2} • sec^{-1}.. Mev^{-1} and R is expressed in counts • sec^{-1}. If the planar flux consists essentially of electrons of energy E_o within a small energy spread ΔE, then an integration over ΔE yields

$$R(\eta, \psi, E_o) = G(\eta, \psi, E_o)\ F(E_o),$$

where $F(E_o)$ represents the intensity of the planar distribution of electrons of energy E_o within ΔE in units of number • cm^{-2} • sec^{-1}. Moreover, if the counter is maintained in this position for a time T, its counts, C, would be given by the equation

$$C = RT = G(\eta, \psi, E_o)\ F(E_o)\ T. \qquad (3\text{-}3)$$

Now, during the calibration process, the linear motion of the detector through the beam effectively widens the beam to the extent of the tube and beyond. The total number of electrons per unit area of this "effective" beam to which the detector is exposed is given by the number of electrons which traverse a differential area moving through the width, w, of the actual beam at the rate of $(\Delta S \cos\eta)/T$. (See Figure 3-1). Since the beam intensity of the actual beam is $I(E_o)$, this number is $I \cdot w \cdot (T/\Delta S \cdot \cos\eta)$. But since the tube was rotated during the calibration, this areal density of electrons was uniformly distributed in angle around the detector. It is therefore equivalent to an irradiation of the detector with a planar flux of F electrons $\cdot$ cm^{-2} . sec^{-1} for a time duration T. Or,

$$FT = I w T/(\Delta S \cos\eta). \qquad (3\text{-}4)$$

When this value of F is put into Equation (3-3), the validity of Equation (3-1) is verified.

Since the apertures of an Anton 222R detectors were much smaller than the cross sectional area of the beam, each of these detectors was calibrated by locating the center of the entrance aperture of the collimator at the central irradiation point and rotating the detector turntable while scaling the counts. The geometric function was then computed by using Equation (3-3) in the form,

$$G(\eta, \psi, E) = \frac{C_T - C_B}{NI(E)T} , \qquad (3\text{-}5)$$

where N is the number of times the detector was rotated in the beam to obtain good statistics ($N \approx 100$).

3.1 EXPERIMENTAL APPARATUS

The experimental equipment used in the calibration of the detectors, except for a rack of electronics equipment, is shown diagrammatically in Figure 3-2 and pictorially in Figure 3-3. The equipment can be grouped into three principal categories: the beta-ray spectrometer; the planar-beam simulation platform, which includes the gimbal support mechanism as well as the turntable and translation carriage mechanisms; and the electronics equipment.

3.1.1 THE BETA-RAY SPECTROMETER

The beta-ray spectrometer is shown at the left of the chamber. This consisted of a 180-degree magnetic deflection spectrometer using a one millicurie Sr-Y source. The spectrometer was mounted on an adjustable platform and located on the small table shown in Figure 3-2. The beta-decay source and the collimation slits which selected the radii of curvature ($\rho \approx 3$ cm) of the electrons were mounted in an aluminum vacuum tight housing of outside dimensions 2-1/2" x 3-1/2" x 1/2", and this "wafer" was inserted into the gap of the magnet. A silphon link was used to connect the wafer to the vacuum tank. In order to rapidly suppress the stray field of the magnet along the path of the electron beam, a one-inch thick cylinder of cold-roll iron was sealed between the wafer housing and the silphon, as shown in Figure 3-2. A window was cut through the iron shield to enable the electron beam to enter the vacuum chamber. The flexible link and the adjustable magnet-support platform facilitated the positioning of the beam in the tank.

After the beam entered the vacuum chamber, it was further collimated to limit its cross section to 3" x 9/16" at the central irradiation point "0" shown in Figure 3-1. A schematic diagram of the spectrometer and the beam is shown in Figure 3-4. The spatial and energy distributions of the beam are described in Section 3.2

A special variable-current power supply was constructed for the magnet of the spectrometer. This supply delivered up to 7 amps at 24 volts, which was more than sufficient to reach the end-point energy of the SrY source. The desired magnet current was adjusted by reading the potential across an 80-mil nichrome-wire shunt with a Rubicon portable potentiometer.

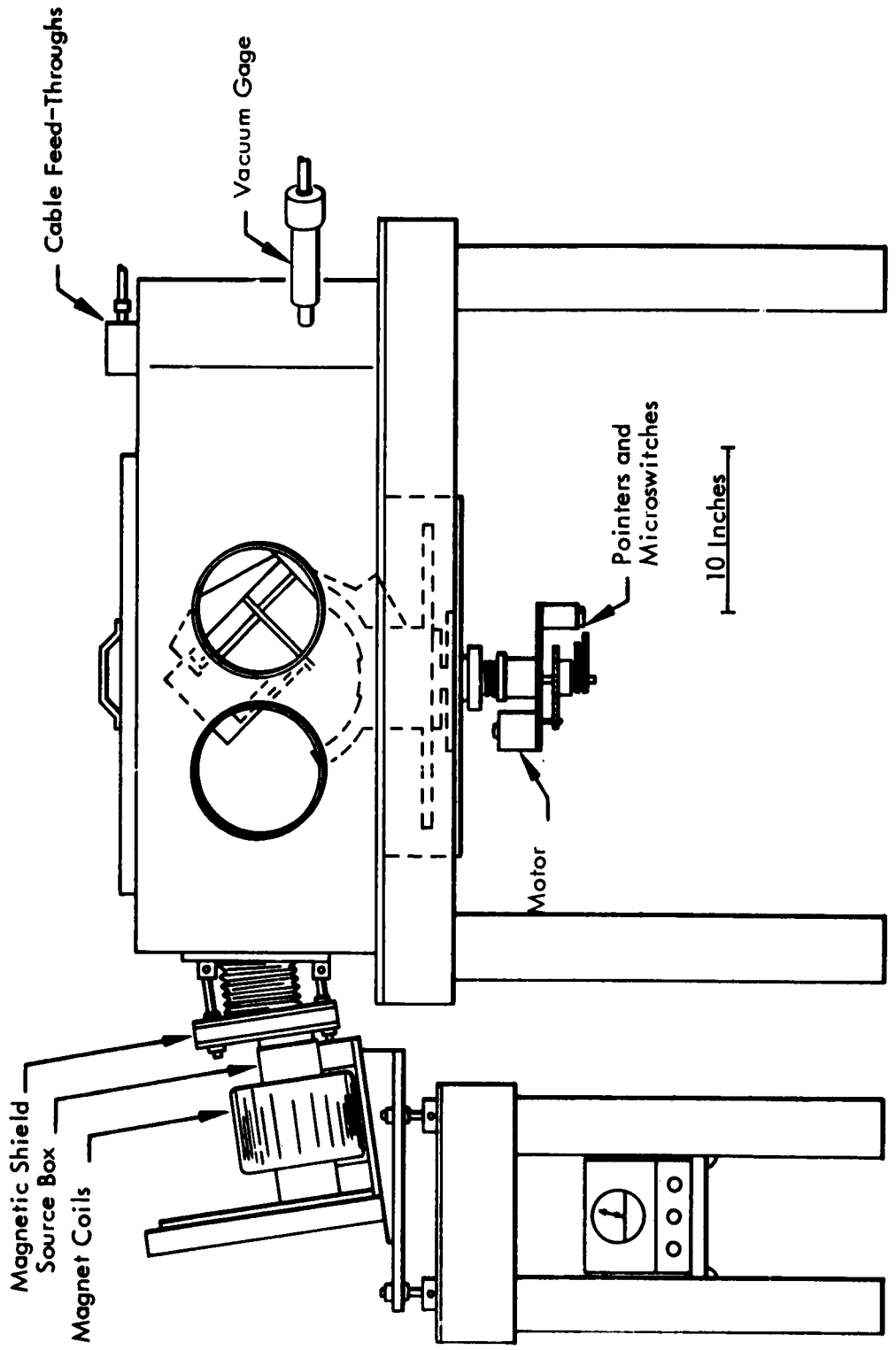

Fig. 3-2 Diagram of Experimental Setup

Fig. 3-3 Experimental Apparatus

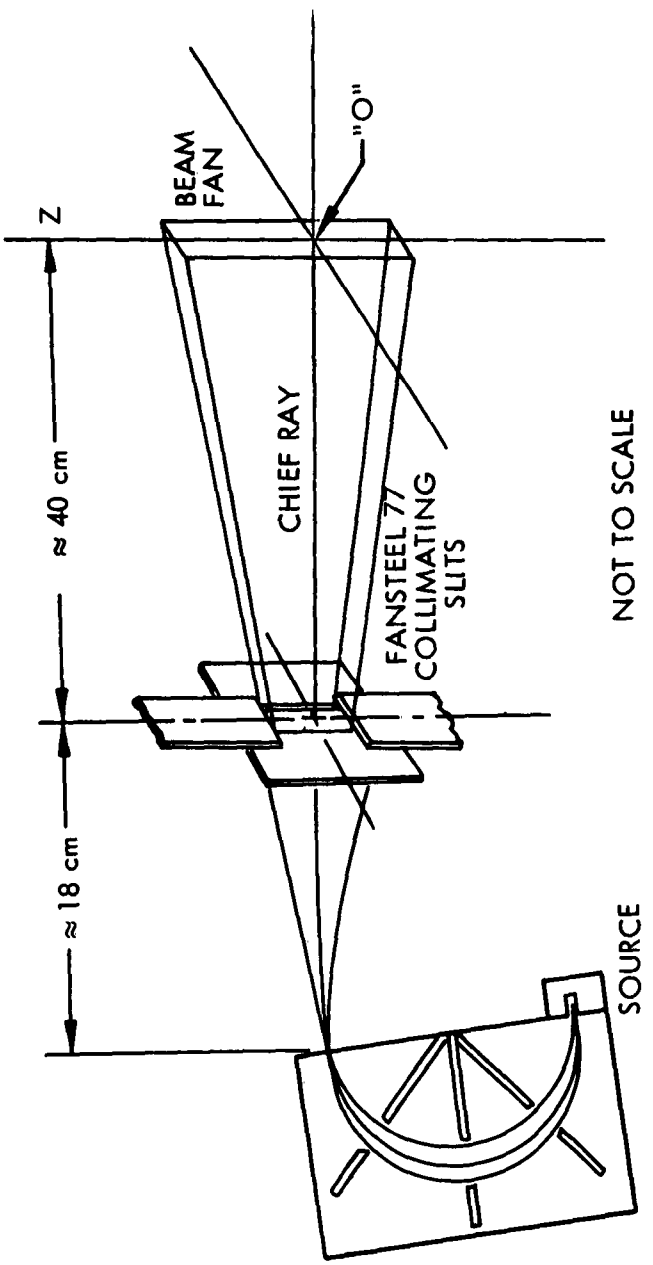

Fig. 3-4 Schematic Diagram of Beta-Ray Spectrometer and Collimation of Electron Beam

3.1.2 PLANAR-BEAM SIMULATION PLATFORM

In this section a description is given of the "target" platform which is depicted at the center of the vacuum chamber in Figure 3-2. This platform serves a dual function: it supports the detectors at the required orientations with respect to the simulated radiation plane, and it rotates and translates the detectors in the electron beam to effect an irradiation of the detectors by a planar flux. A diagram of this assembly is shown in Figure 3-5.

The turntable was located at the bottom of the cylindrical "well" of the vacuum chamber as indicated in Figure 3-2. An O-ring seal was used to feed the shaft of the turntable through the base plate of the chamber. The turntable drive mechanism together with a cam-microswitch arrangement which controlled the maximum angle of rotation of the turntable in either direction were located beneath the chamber. A Bodine synchronous-capacitor motor drove the turntable through reducing gears at the uniform rate of 0.25 rpm. This equipment under the chamber is shown in Figure 3-6.

The gimbal mechanism, which rides on the turntable and supports the translation carriage to which the instrumentation package is attached, is illustrated in Figure 3-5. Also, pictures of this device are shown in Figures 3-7a and 3-7b. Figure 3-7a affords a good view of the motor and screw-drive mechanism which move the detector package across the electron beam. A study of Figures 3-5, 3-7a, and 3-7b reveals the manner in which the detector-orientation adjustments were made. The angle η was set by adjusting the positions of the clamps on the two C-bars mounted to the base plate. The angle ψ was adjusted by rotating the carriage mount structure about a shaft fixed to the brace which rides on the C-bars.

The carriage-drive motor was a Bodine two-phase servomotor which had an output of 22 revolutions/minute through a gear-reducer system. Since it was necessary to operate this motor in the vacuum system, special precautions were taken: the original oil in the motor was replaced with Silicon grease, and a heat sink for the motor was constructed. The heat sink provision consisted of constructing good thermal paths for the conduction of the motor heat to the structure of the gimbal mechanism.

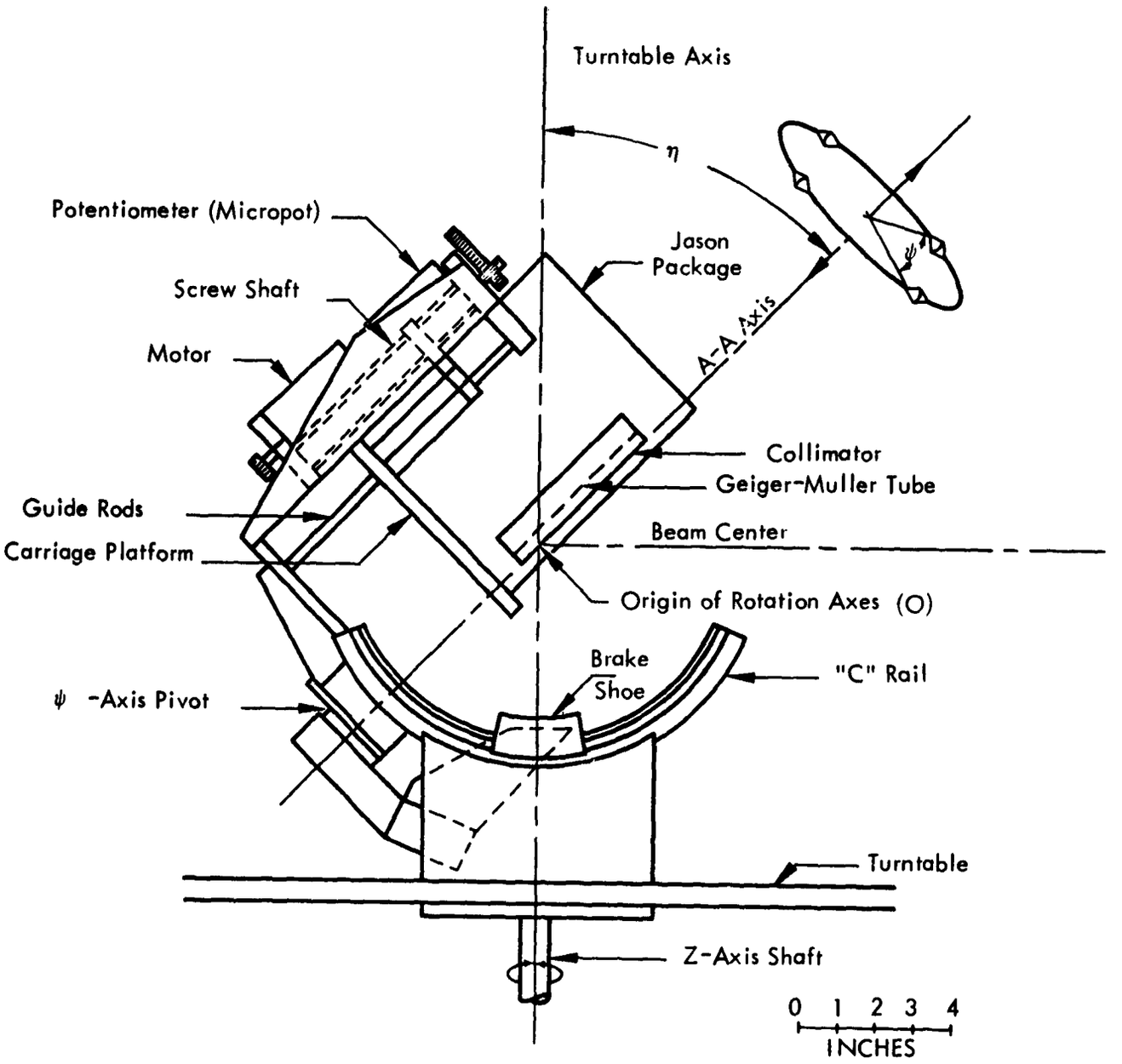

Fig. 3-5 Diagram of Gimble Support Mechanism

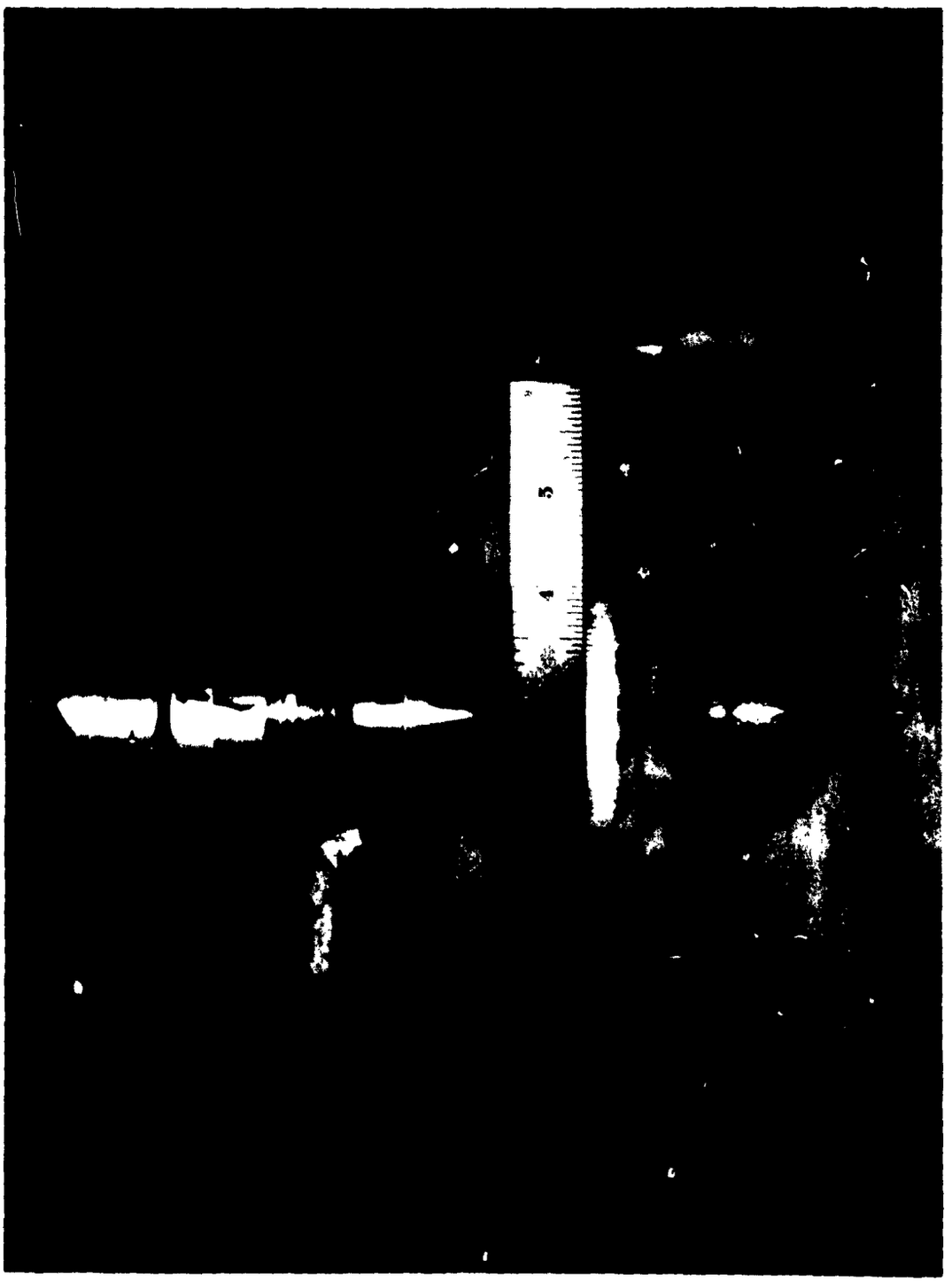

Fig. 3-6 Turntable Drive Mechanism and Limit Microswitches Under Vacuum Chamber

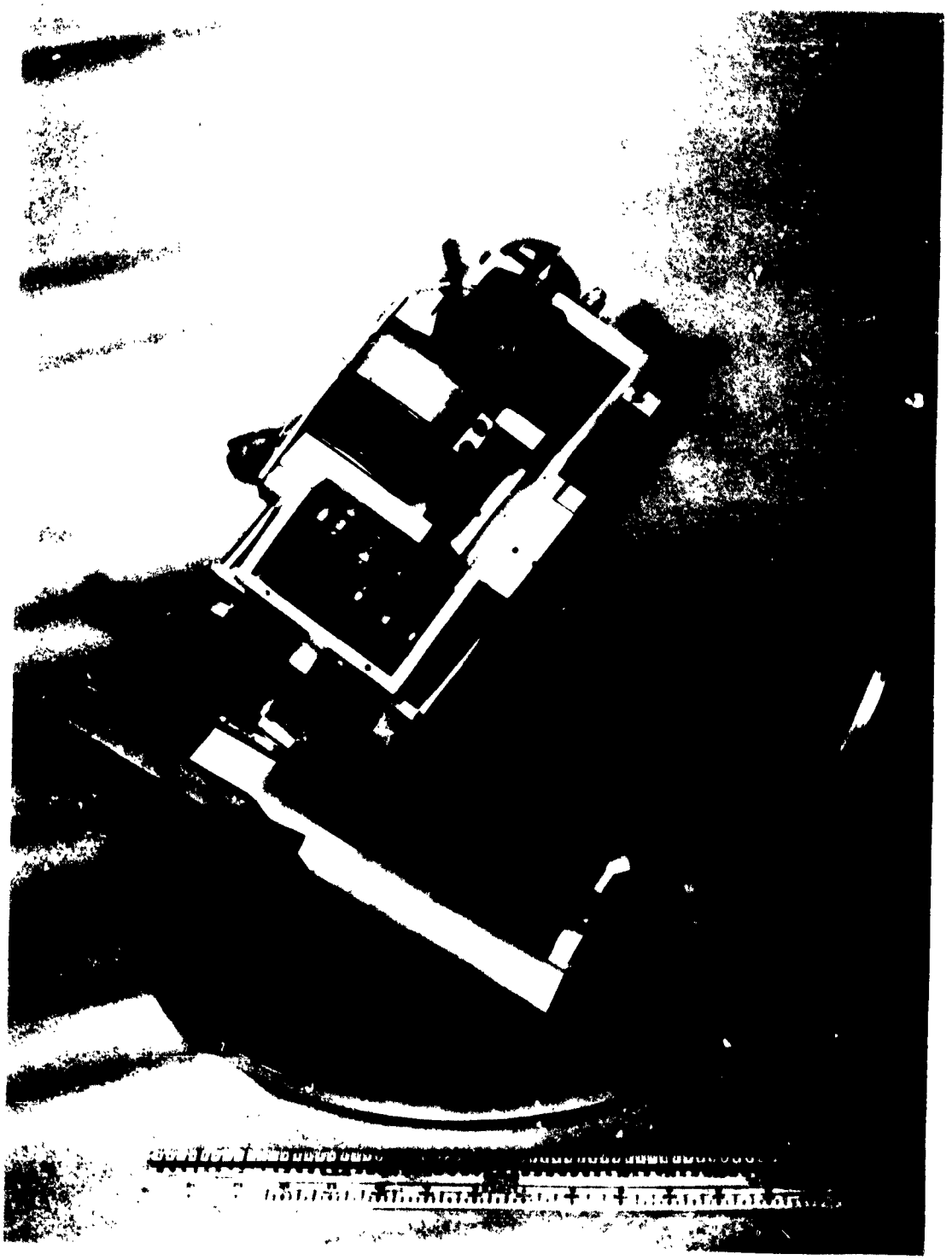

Fig. 3-7a Gimble Support Showing Carriage-Drive Mechanism

Fig. 3-7b Additional View of Gimble Support

3.1.3 ELECTRONICS EQUIPMENT

The automatic operation of the rotation-translation motions of the detectors was controlled by a master control unit. The operation was such that the carriage was moved in preselected movements of 1/16-inch, 1/8-inch, or 1/4-inch every time a turntable limit switch was hit by the pre-set cams on the turntable axis. A block diagram of the logic of the automation system which performed this function is shown in Figure 3-8, and the operation of the equipment during a calibration run is outlined below.

(1) The cams on the axis of the turntable were adjusted for the desired limit of rotation of the turntable in each direction. These limits were set by observing the rotation angles at which the counting rate of the detector under calibration dropped to its cosmic-ray background level.

(2) The "Electrical Overrride" on the master control unit was then operated to move the carriage to the starting position. At this position the detector was just out of the beam.

(3) The translation movement of the carriage (1/16", 1/8", or 1/4") for the run was selected by adjusting the "Stepping Device Preselector" switch.

(4) The run was then started. The turntable rotated in a certain direction until a limit switch was hit.

(5) The actuation of the limit switch initiated the following sequence of events:

- The turntable motor was stopped.
- The stepping switch was energized, and it applied a step voltage to the input of a servo-amplifier. The magnitude of this voltage controlled the incremental motion of the carriage.

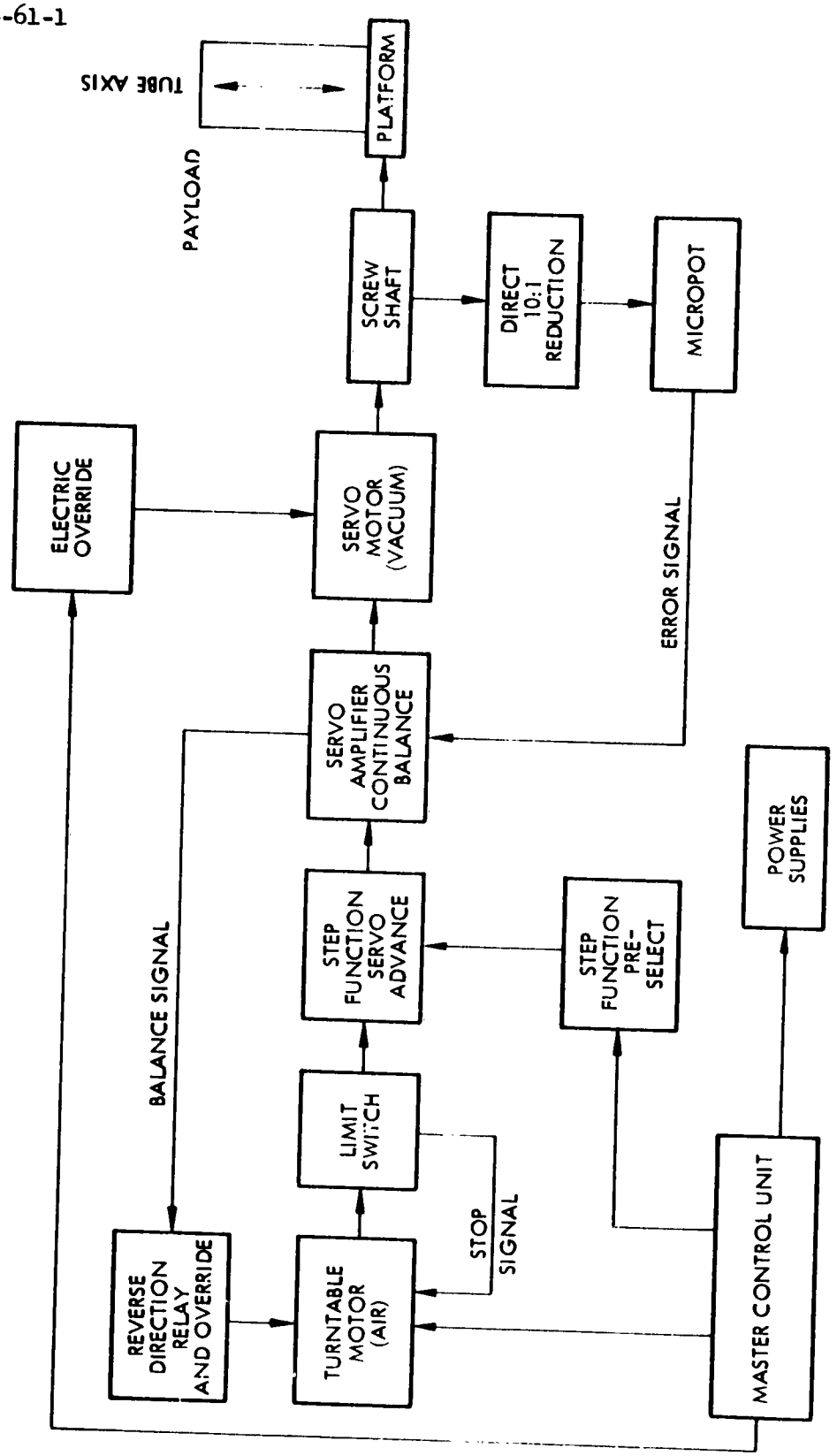

Fig. 3-8 Block Diagram Showing Operation of Master Control Unit

- The output of the servo-amplifier energized the carriage motor until the new position of the carriage was reached.
- The correct position of the carriage was sensed by the balancing of the voltage applied to the servo-amplifier by the stepping switch and a voltage controlled by a micropot connected to the screw-drive shaft of the carriage.
- After the correct carriage position was reached, the turntable motor was again actuated, but with reversed polarity, effecting the rotation of the detector in the opposite direction.

(6) This process was repeated each time a limit switch was actuated until the carriage reached its opposite limit position across the beam.

(7) After this position was reached, the detector motions were stopped, and the scaler which recorded the total number of detector pulses during the run was disengaged.

Thirty to seventy rotations through the beam were made during a run. The time duration of a run varied from 30 to 60 minutes.

3.2 ALIGNMENT AND CALIBRATION OF ELECTRON BEAM

In preparing the spectrometer for the detector calibration work, the fan plane of the beam (the medium plane through the spectrometer magnet gap) was first aligned with the center-line of the turntable axis. This alignment was accomplished by adjusting the position of the spectrometer outside the chamber while monitoring the location and distribution of the beam inside the chamber.

Energy spectra of the electrons were measured throughout the cross section of the beam by means of a plastic scintillation spectrometer. Pulse height distributions from the spectrometer were recorded by a 100-channel pulse height analyzer. Spatial distributions of the intensity as well as the spectra of the electrons in the beam cross section were measured by mounting a collimating slit in front of the plastic scintillator and moving the spectrometer through the beam with the translation carriage mechanism. By setting the gimbal settings to $\eta = 90^{\circ}$ and $\psi = 0$, horizontal cuts through the beam were taken. Such traversals were made at various elevations with respect to the central irradiation point to test the vertical alignment of the fan plane of the beam. With the gimbal settings at $\eta = 0$ and $\psi = 0$, vertical cuts through the beam were taken.

With no external collimation of the beam, the results of these measurements revealed the following information:

(1) The edges of the beam were quite sharp, being "smeared" over a distance which was well within the width of the detector slit (3/16").

(2) The cross section of the beam had a width of about 5/8" and a height of 6".

(3) The energy spectrum was quite uniform over the entire cross section: the greatest departure from uniformity was observed at the lowest electron energy of interest (E 150 kev); here, the displacement of the peaks of the pulse-height spectra over the 6" height of the beam was about 5%, and

(4) The intensity distribution along the height of the beam was far from being uniform: it varied rather linearly along the height, differing by nearly a factor of two from one end to the other.

The non-uniform vertical distribution of the electron beam intensity was unfortunate, and it was necessary to restrict the height of the beam to a region where the linear approximation of the intensity variation was good. A linear variation was not considered to be troublesome since the detectors were symmetrical above and below the central irradiation point "0".

Since it was necessary for the beam to cover the entire aperture of the detector in the vertical direction, the minimum height of the beam was dependent on the orientation angle η and on the width of the beam. This height was found to be about 1-1/4" for the maximum range in η (69° to 111°) given by the analysis of the body motions of the rockets and for a beam width of 9/16". Hence, the external collimator shown in Figure 3-4 was arranged to restrict the width of the beam to 9/16" and the height of the beam to about $\pm$1" from the central position.

The horizontal distribution of the beam across the central position was then measured, and the result is shown in Figure 3-9. The solid-line trapezoid drawn in the figure depicts the fold of a 3/16" slit with a 9/16" wide pedestal-shaped beam distribution. The vertical distribution of the beam is shown in Figure 3-10. The origin, point 0, of the abscissa corresponds to the central irradiation point.

After the beam was aligned and calibrated, the intensity and energy of the beam versus magnet current were measured with a plastic scintillation spectrometer. A collimator with an aperture 3/4" wide and 1-1/2 high was placed in front of the 2" diameter plastic scintillator, and the spectrometer was mounted on the gimbal mechanism such that the center of the aperture coincided with the central irradiation point "0" shown in Figure 3-1 and Figure 3-5. In this condition, therefore, the entire width of the beam and

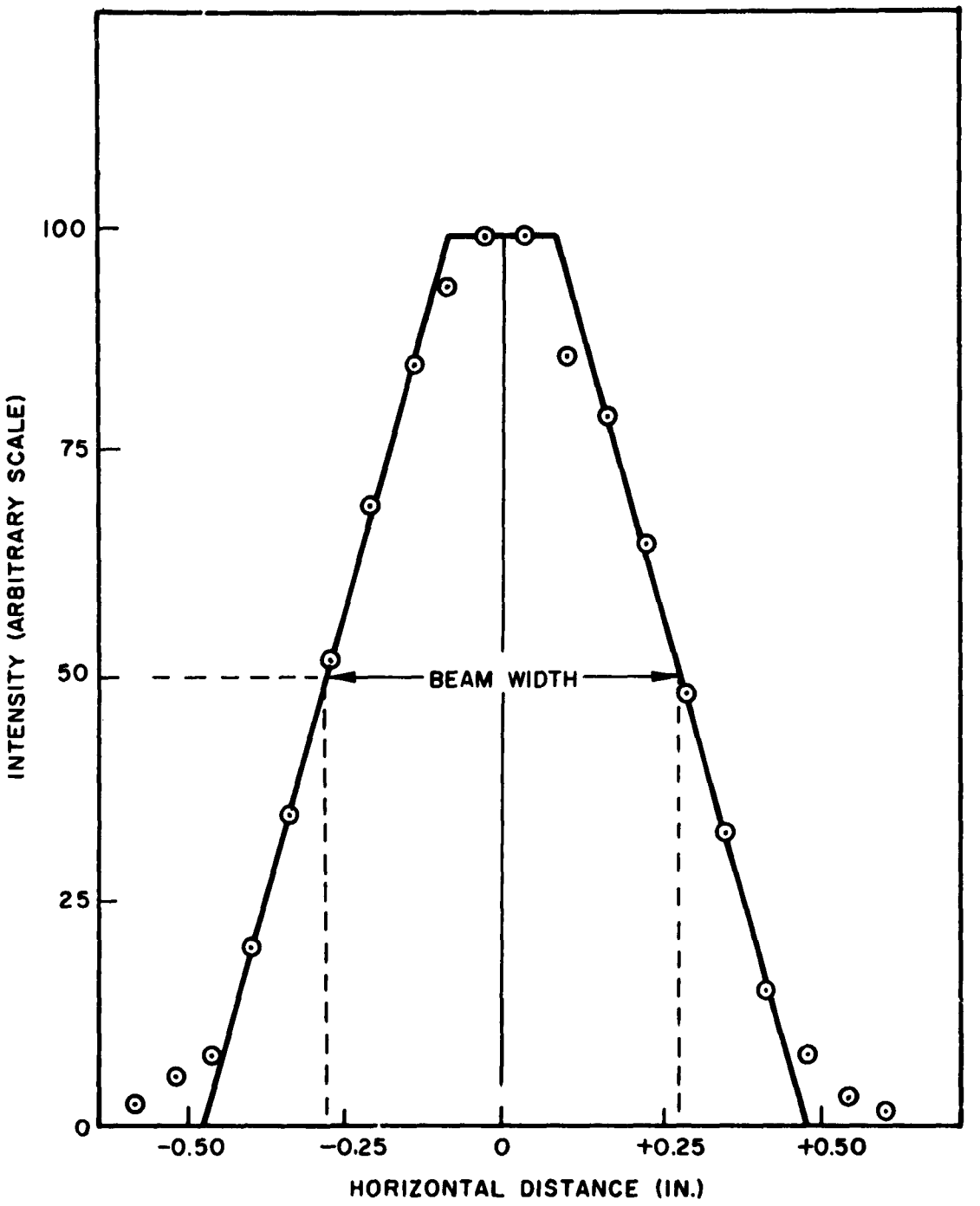

Fig. 3-9 Horizontal Intensity Distribution of Beam

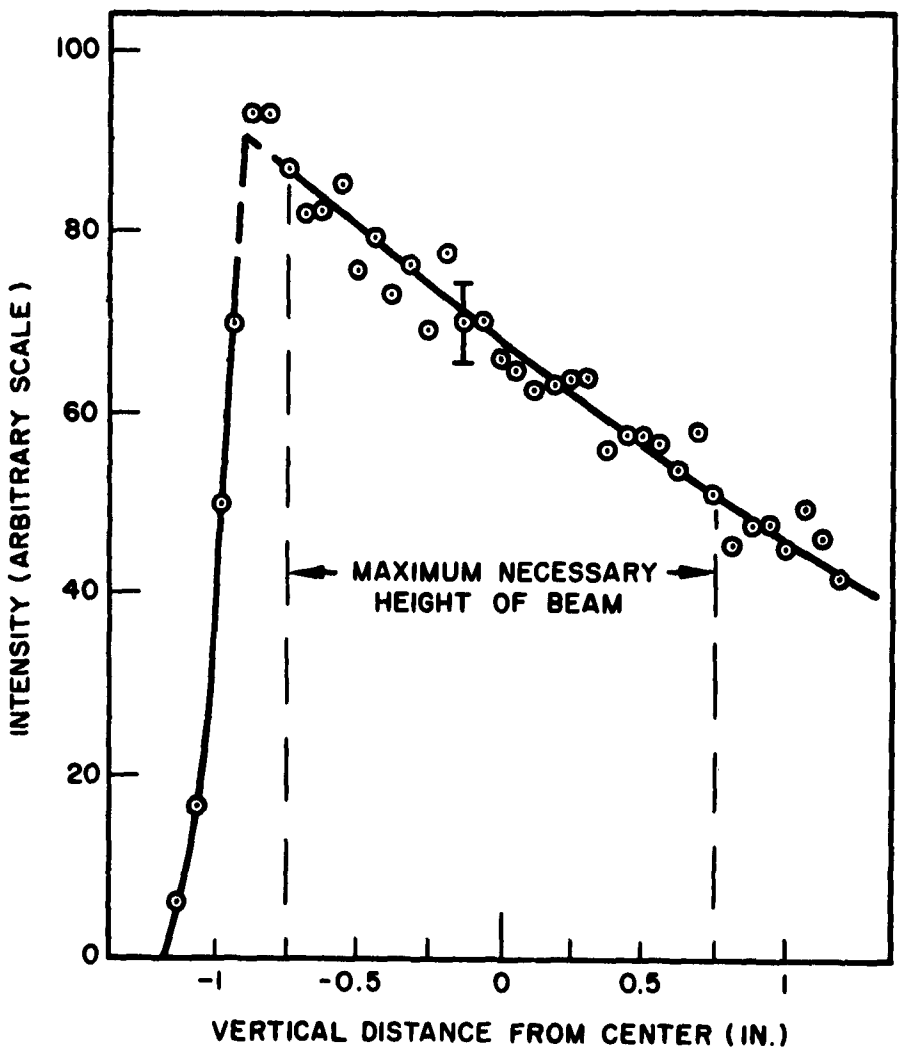

Fig. 3-10 Vertical Intensity Distribution of Beam

the height of the beam from -3/4" to +3/4" shown in Figure 3-10 fell within the aperture of the spectrometer. Pulse-height spectra were then obtained with a 100-channel analyzer as a function of magnet current. For each value of the magnet current used, the beam energy was taken to be that given by the peak of the pulse-height spectrum after the background spectrum was subtracted. Various γ-emitting radioactive sources were used to calibrate the scintillation spectrometer. The intensity of the beam was computed from the total number of counts in the distribution above the background. The energy of the beam as a function of the potentiometer reading of the voltage across a standard shunt is given in Figure 3-11. The intensity of the beam, also as a function of the potentiometer reading, is given in Figure 3-12.

By cycling the magnet current before adjusting the current to the desired value, the beam energy was found to be reproducible to about 2%. A recalibration of the beam after a month of operation revealed a negligible change in the beam characteristics.

The beam energy as a function of magnet current was also computed by measuring the magnetic field in the center of the magnet gap with a 1% flip-coil magnetometer and the mean radius of curvature allowed by the spectrometer stops. These computations agreed well with the spectrometer measurements when a radius of 2.90 cm was used rather than the measured value of 3.00 cm. This error probably resulted from the fact that the peak field intensity rather than the mean intensity along the path of the electrons was used. Further agreement with the energy calibration of the beam was observed by preparing a Fermi plot of the intensity distribution data. This plot, shown in Figure 3-13, is seen to define a straight line which yields the end-point energy of the SrY source used in the spectrometer to within a few percent.

3.3 DETECTOR CALIBRATION RESULTS

The method used in the analysis of the data obtained with the Wallops-Island launched rockets required knowledge of the geometric functions of the detectors in the orientation range $69^{\circ} \leq \eta \leq 111^{\circ}$ and $-20^{\circ} \leq \psi \leq 20^{\circ}$.

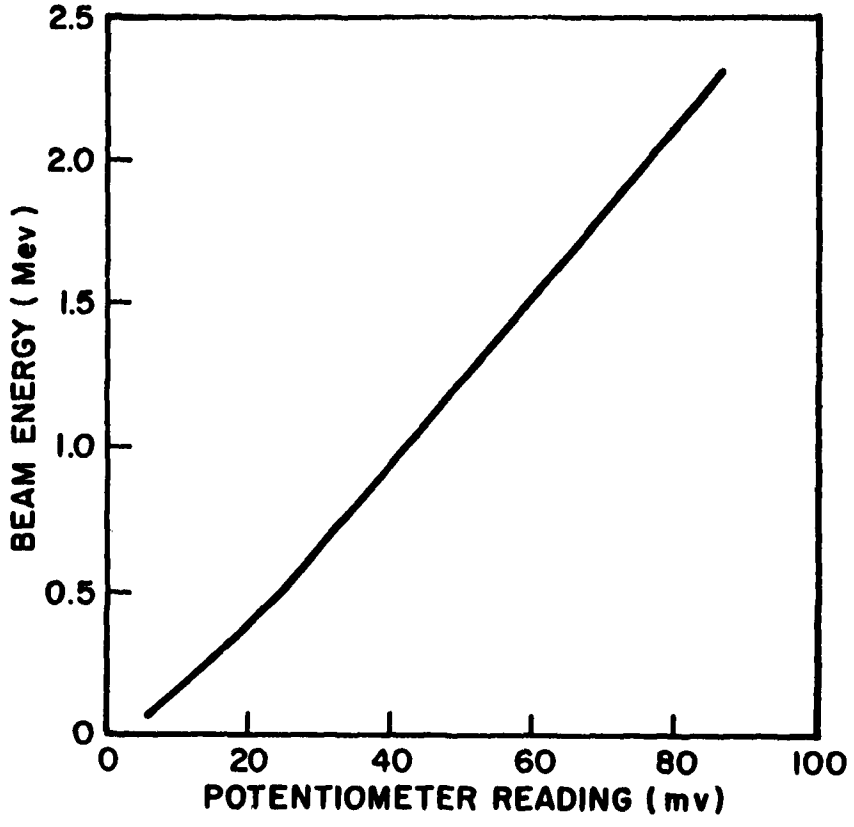

Fig. 3-11 Electron Beam Energy as Function of Magnet Current. Current reading is in terms of the potentiometer reading

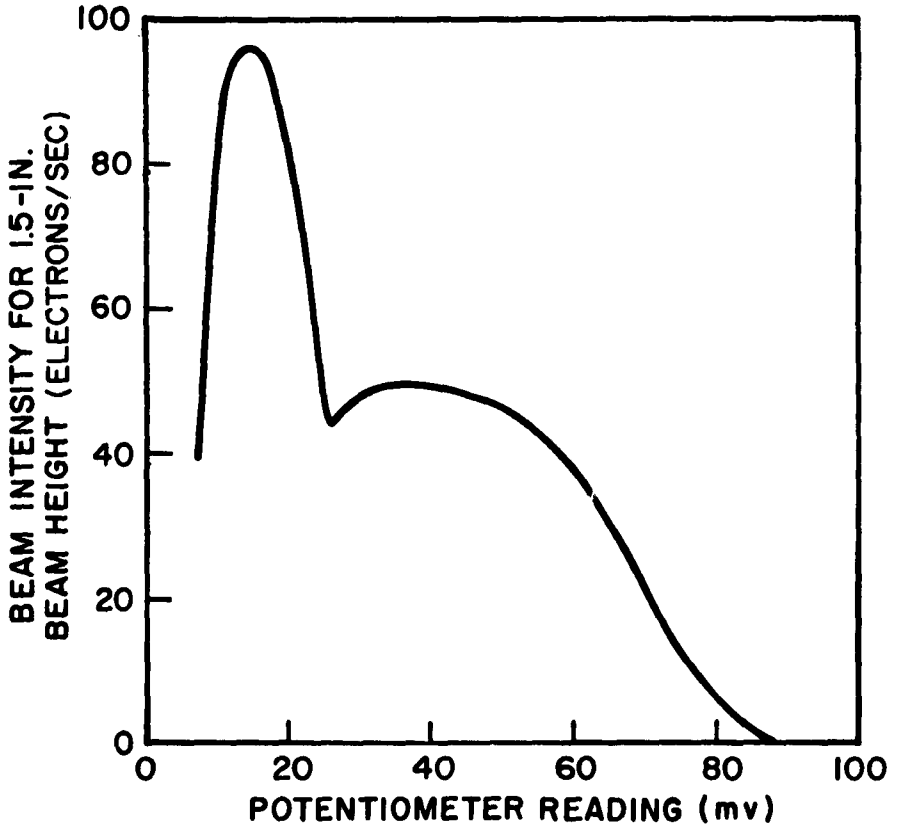

Fig. 3-12 Electron Beam Intensity Over 1.5-in. Beam Height (Electrons/Sec) as a Function of Magnet Current (Potentiometer Reading)

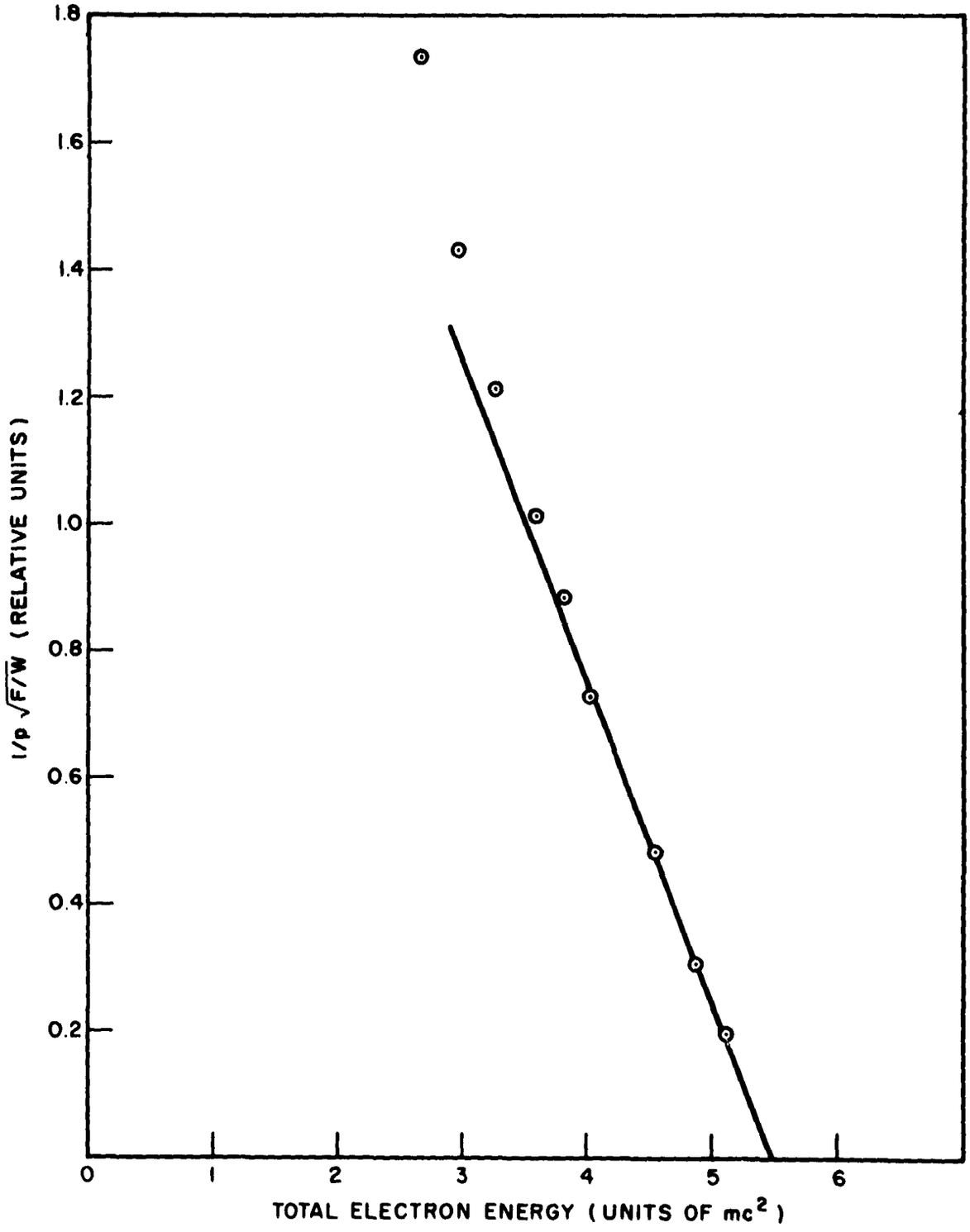

Fig. 3-13 Fermi Plot Given by Beta-Ray Spectrometer Data. Abscissa gives total energy in units of rest mass energy of the electron

The range in η was given by the determination of the body motions of the rockets in free flight. The range in ψ of $\pm 20^{\circ}$ was important because only those counting rates of the detectors which were read out in this range of ψ were used in the analysis. Counting rates which were sampled in flight while the detectors were oriented at larger angles of were not used because it was believed that large errors would have resulted from the non-planar distribution of the trapped electrons.

The geometric functions measured in the laboratory were obtained for various values of the parameters η, ψ, and E. The data below reveal, however, that the geometric functions of the long tubes were quite insensitive (less than 5%) to the orientation angle η within the range given above. This dependence was therefore neglected. Moreover, since the counting-rate samples which occurred within the ψ interval of $\pm 20^{\circ}$ were averaged over a number of spin cycles of the rocket, the geometric functions used to unfold the data were also averaged over this interval of ψ in a manner discussed below. The end result, therefore, was a geometric function for each detector which was dependent on the electron energy alone.

The counting rates of the small detectors were analyzed in a somewhat different manner, as discussed below. But that method also required an average of the geometric functions over the interval $-20^{\circ} \leq \psi \leq 20^{\circ}$.

The calibration data are given below, with the results for the long detectors preceding those for the small detectors. Within each of these groups of detectors, the detectors are considered in the order of their increasing threshold energies.

3.3.1 CALIBRATION OF CHANNELS 1 AND 5

The detectors in Channels 1 and 5 were identical in construction. Each consisted of an Anton 106C geiger tube (30 mg/cm^2 - steel wall thickness) with a brass collimator forming six rectangular windows along the length of the tube (see diagram in Figure 1-1).

First the orientation angle η of the detector in Channel 1 was set equal to 90° (longitudinal axis of detector in radiation plane), and calibration runs were made at a number of values of beam energy for each of the

following settings of ψ : -25.2°, -19.8°, -12.6°, -3.6°, +3.6°, +10.8° and +19.8°. Using Equation (3-1) the geometric functions were computed from the data obtained at each orientation of the detector, and the functions were plotted against electron energy. A graph of the results for the position $\eta = 90°$, $\psi = 3.6°$ is shown in Figure 3-14. The error bars drawn at the data points are standard deviations due to counting statistics. Error bars are not shown at the lower energy points where the errors are smaller than the circles depicting the data. The threshold energy of this detector is seen to lie at about 200 kev.

To obtain an average of these geometric functions over the angle ψ, the functions were read off the curves drawn through the data as shown in Figure 3-14 at various values of electron energy and plotted against the angle ψ. A graph of the resulting curves, for a few of the energy parameters used, is shown in Figure 3-15. The geometruc function for each of the energy parameters used, was then averaged over the interval $-20° \leq \psi \leq 20°$ by means of a planimeter. The geometric function given by this averaging process is shown in Figure 3-16.

The result of a calibration run taken at $\eta = 72°$, $\psi = 0$ is shown in Figure 3-17. Within the statistics of the measurements, the geometric function given in this figure is indistinguishable from that given by extrapolating the measurements taken at $\eta = 90°$, $\psi = -3.6°$ (see Figure 3-14) to the peak response at $\psi = 0$ (see Figure 3-15).

Two additional calibration runs were taken, one at $\eta = 72°$, $\psi = 0$ and the other at $\eta = 72°$, $\psi = 19.8°$. During these runs, three of the six collimator windows of the detector (see Figure 1-1) were covered with 1/8" of copper, as was done on some of the flights. The covered windows were the windows at the extreme end of the detector (end towards nose of rocket) and the other two were the adjacent windows at the opposite end of the detector. The ratio of the geometruc functions of the plugged and unplugged detectors measured at the same orientation to the beam ($\eta = 72°$, $\psi = 0$), was found to be 0.652. Moreover, this value agreed with the ratio of the geometric function of the plugged detectors at $\eta = 72°$, $\psi = 19.8°$ to that of the unplugged detector at $\eta = 90°$, $\psi = 19.8°$, yielding further evidence of the insensitivity of the geometric functions to relatively small departures of η from 90°.

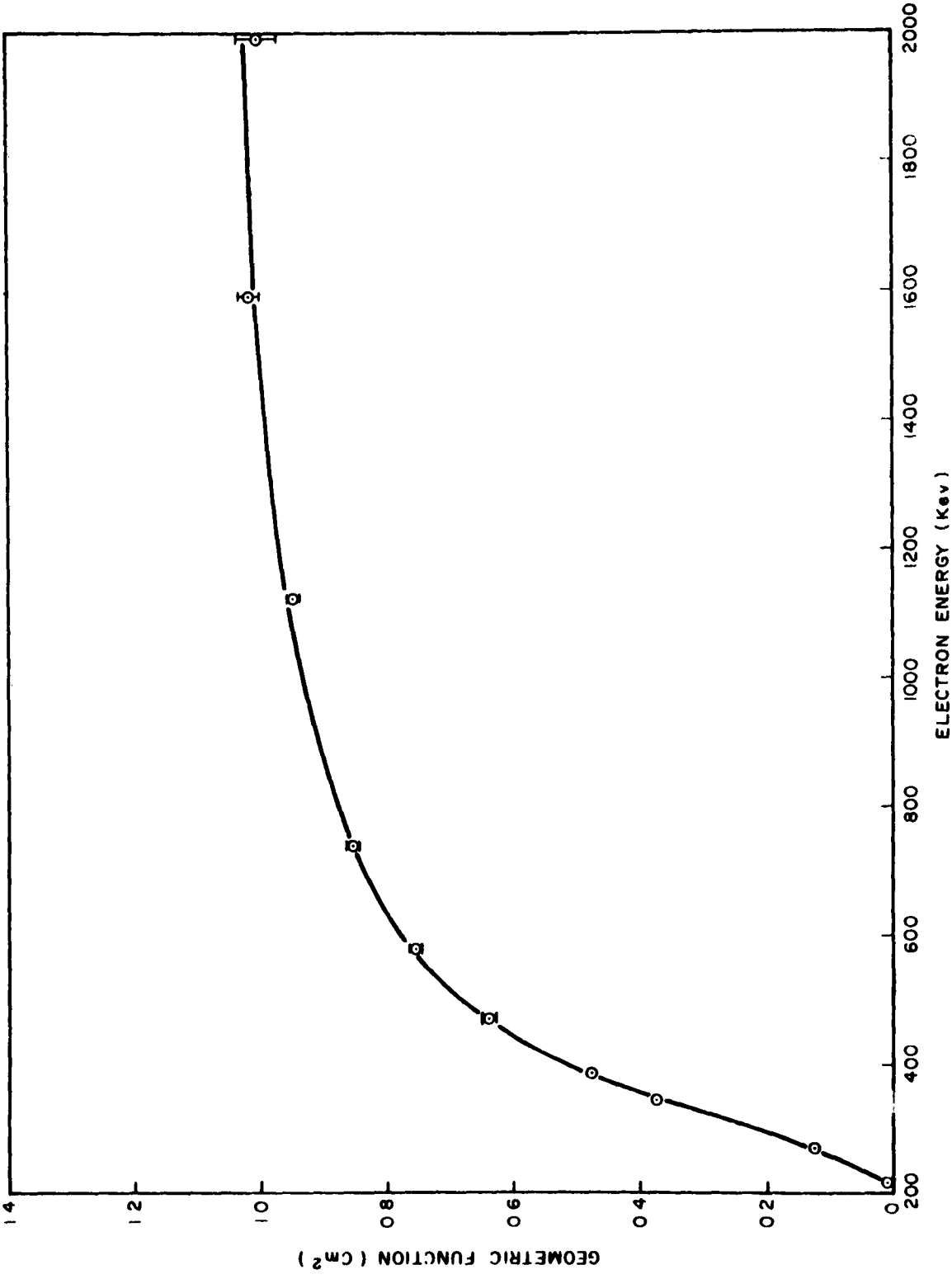

Fig. 3-14 Geometric Function of Detector in Channel 1 for Orientation Angles of $\eta = 90°$ and $\psi = -3.6°$

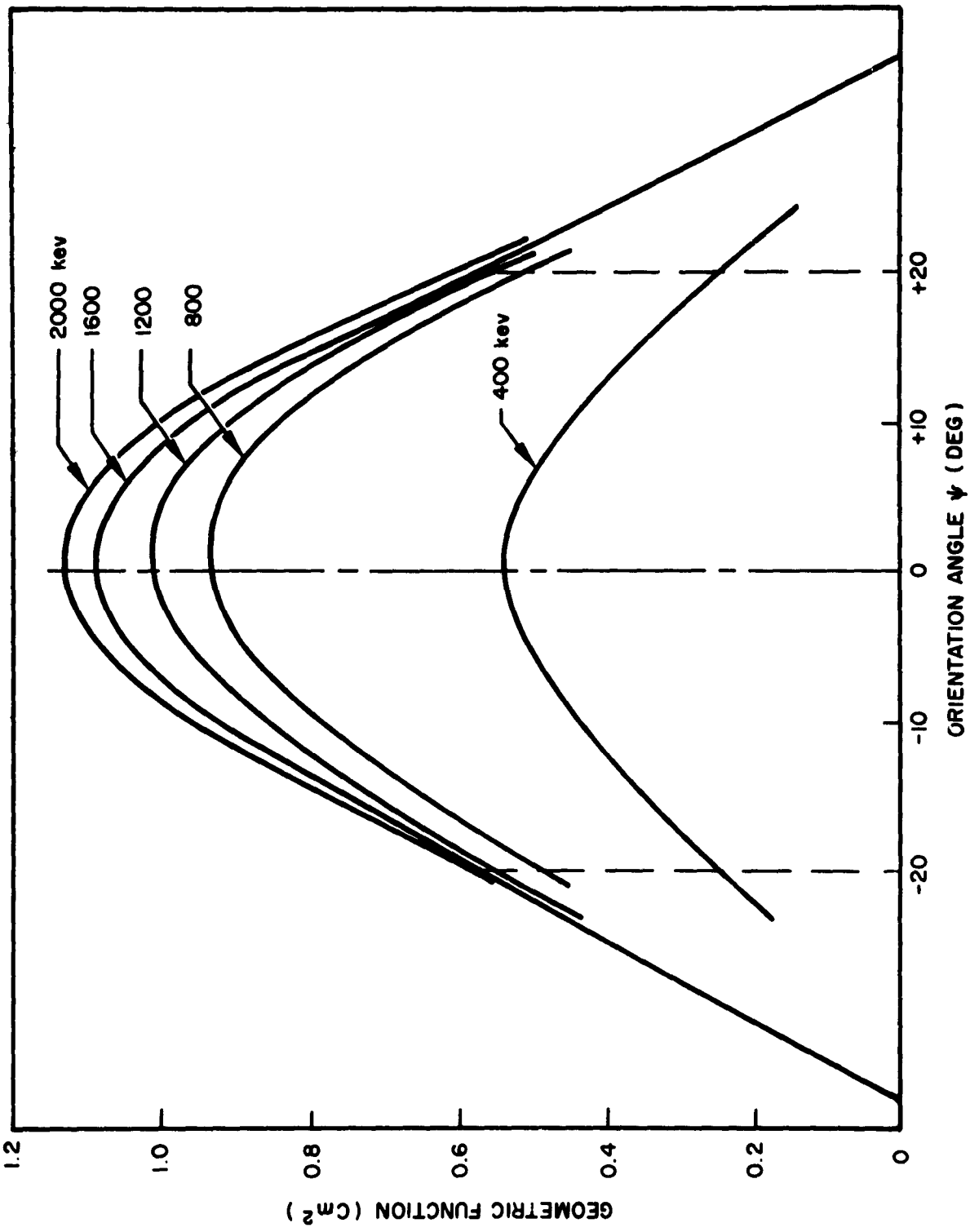

Fig. 3-15 Geometric Functions of Detector in Channel 1 Versus Orientation Angle ψ for Energies of 400, 800, 1200, 1600, and 2000 kev

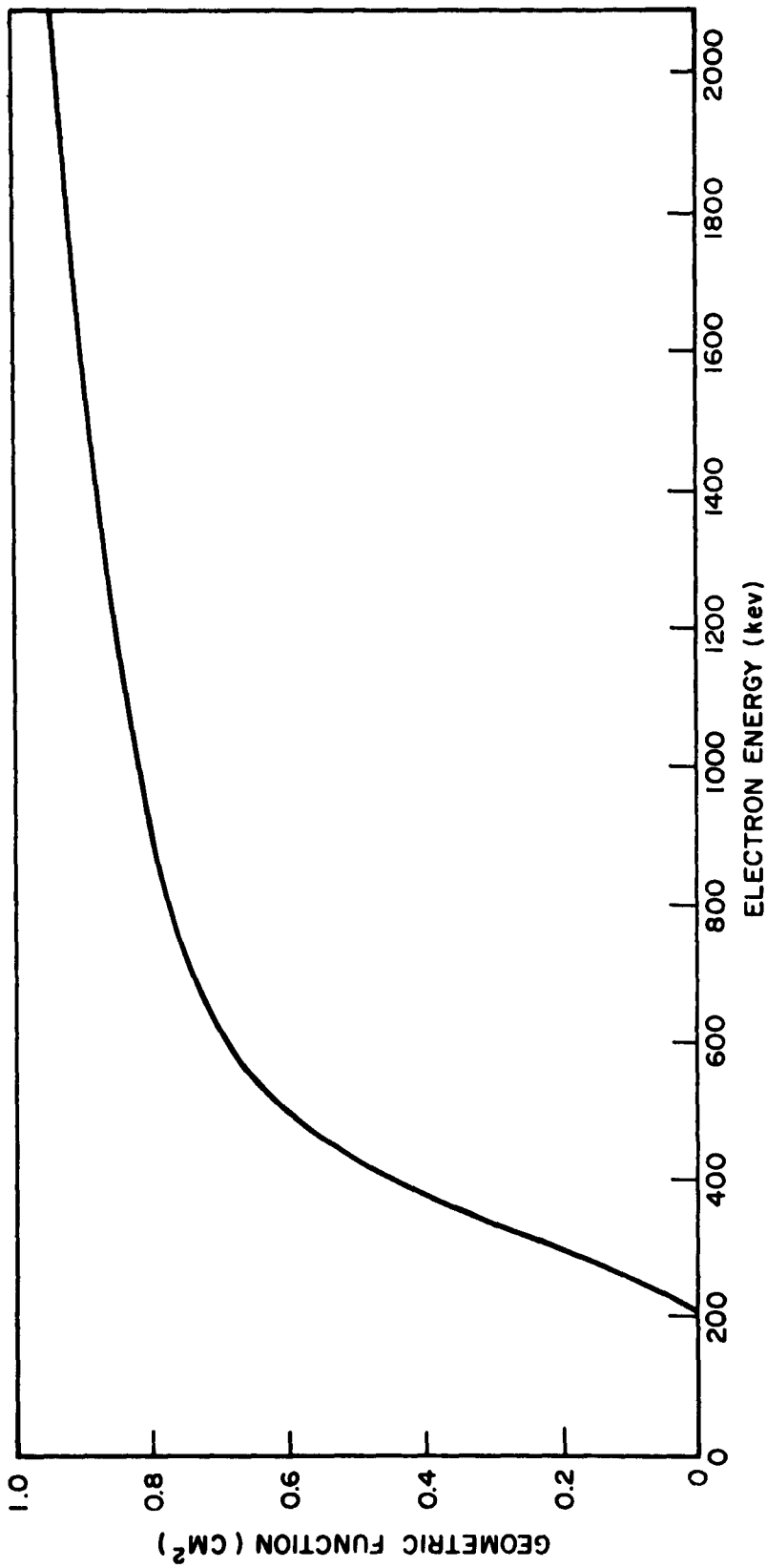

Fig. 3-16 Final Geometric Function of Detector in Channel 1

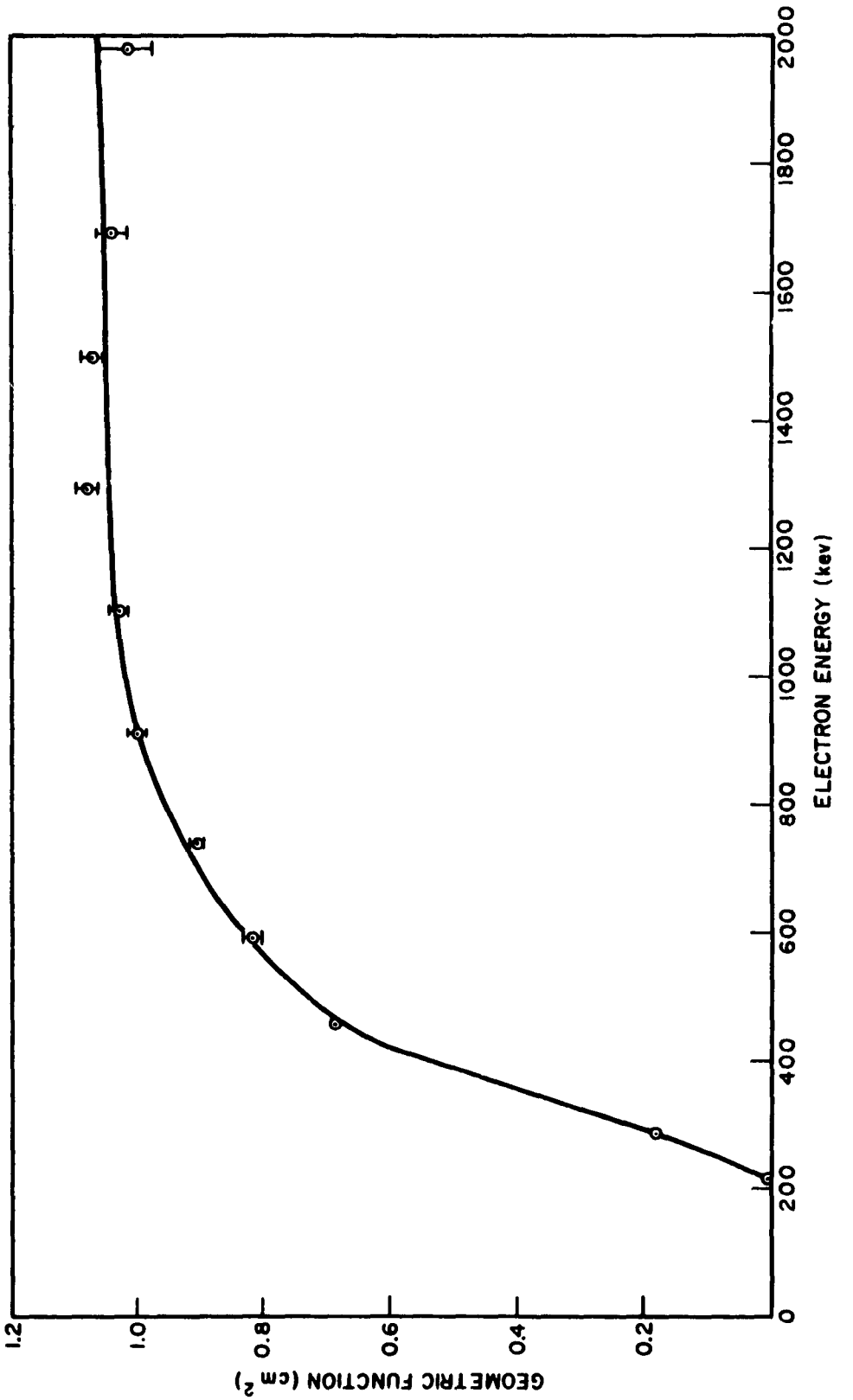
ELECTRON ENERGY (kev)
0
200
400
600
800
1000
1200
1400
1600
1800
2000
GEOMETRIC FUNCTION (cm²)
1.2
1.0
0.8
0.6
0.4
0.2

Table 1 in the Appendix lists the energy-dependent geometric function of the plugged detector in Channel 1. It is the geometric function shown in Figure 3-16 multiplied by 0.652.

3.3.2 CALIBRATION OF CHANNEL 7

The detector in Channel 7 also consisted of an Anton 106C geiger tube, but this tube was not deliberately collimated. It was shielded with a cylindrical sheath of aluminum about 150 mg/cm^2 thick.

Visual observations revealed that, throughout the orientation range $-69^\circ \leq \eta \leq 111^\circ$, $-20 \leq \psi \leq 20^\circ$ and beyond, the aperture of the detector in a planar flux was unchanged. Measurements of the counting rate of the tube at various electron energies revealed that this was indeed the case. For $\eta = 90^\circ$ these counting rates were found to be constant over a total range of ψ of about 60°. Hence, an averaging of the geometric function of this detector over ψ was not necessary.

The energy-dependent geometric function of this detector is shown in Figure 3-18a. The threshold energy is about 470 kev. Since these data indicate that the response of the tube is still rising appreciably at the highest electron beam energy used, the cylindrical shield was removed to measure the geometric function of the "bare" tube. This bare tube value was considered to be a reasonable value which the shielded detector would approach at higher energies. Hence, the curve drawn to the data was extrapolated to the "bare" tube value as shown in Figure 3-18b. This geometric factor is also listed against energy in Table A-1.

3.3.3 CALIBRATION OF CHANNEL 3

The detector in Channel 3 again was an Anton 106C geiger tube, not deliberately collimated, but encased within a cylindrical shield of aluminum, 400 mg/cm^2 in thickness.

Again, visual as well as experimental observations revealed that the geometric function of this detector should be constant in a planar flux over the range of orientation of the detectors given above. The experimental

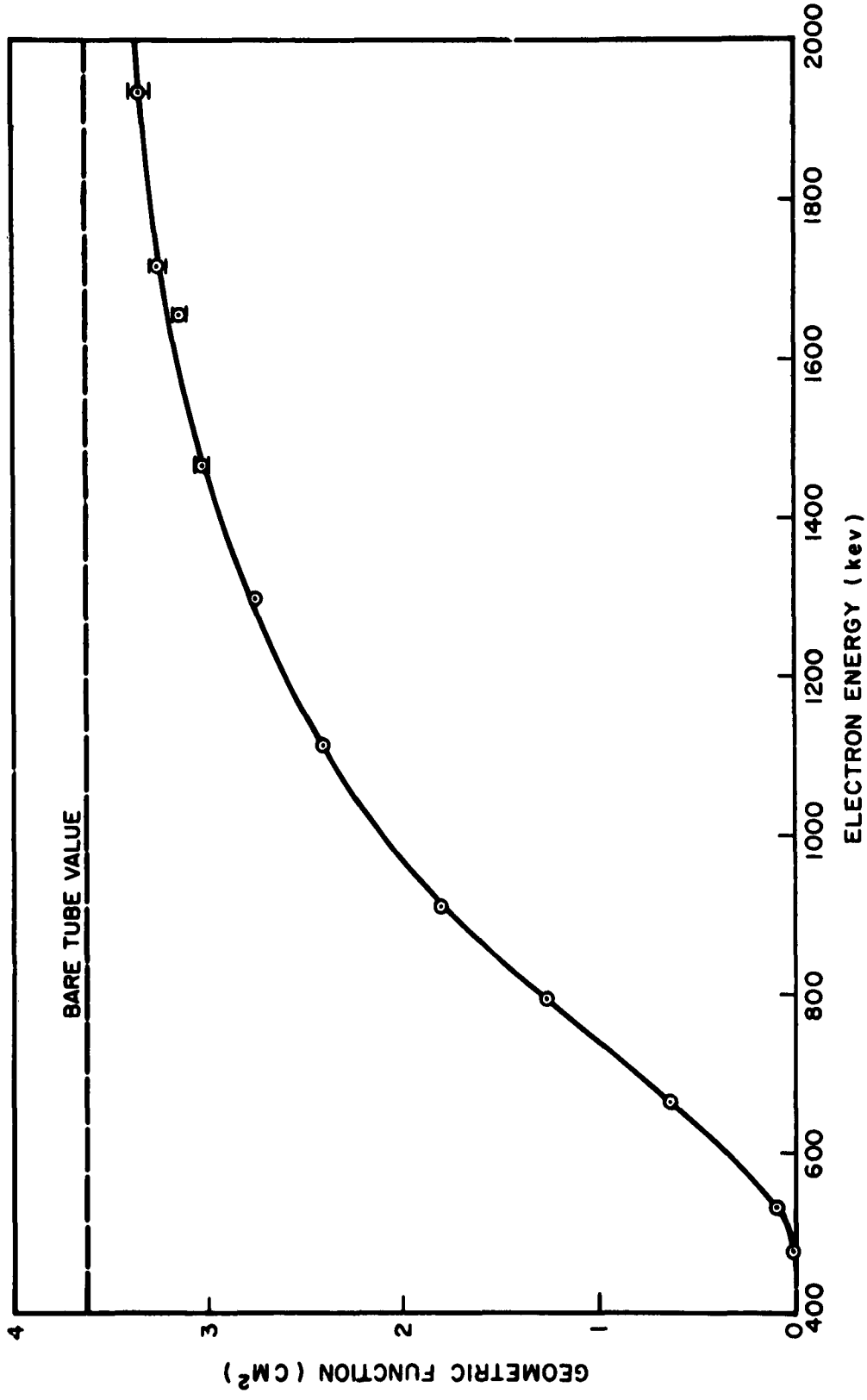

Fig. 3-18a Geometric Function of Detector in Channel 7 for Orientation Angles of $\eta = 90°$ and $-25° \leq \psi \leq 25°$

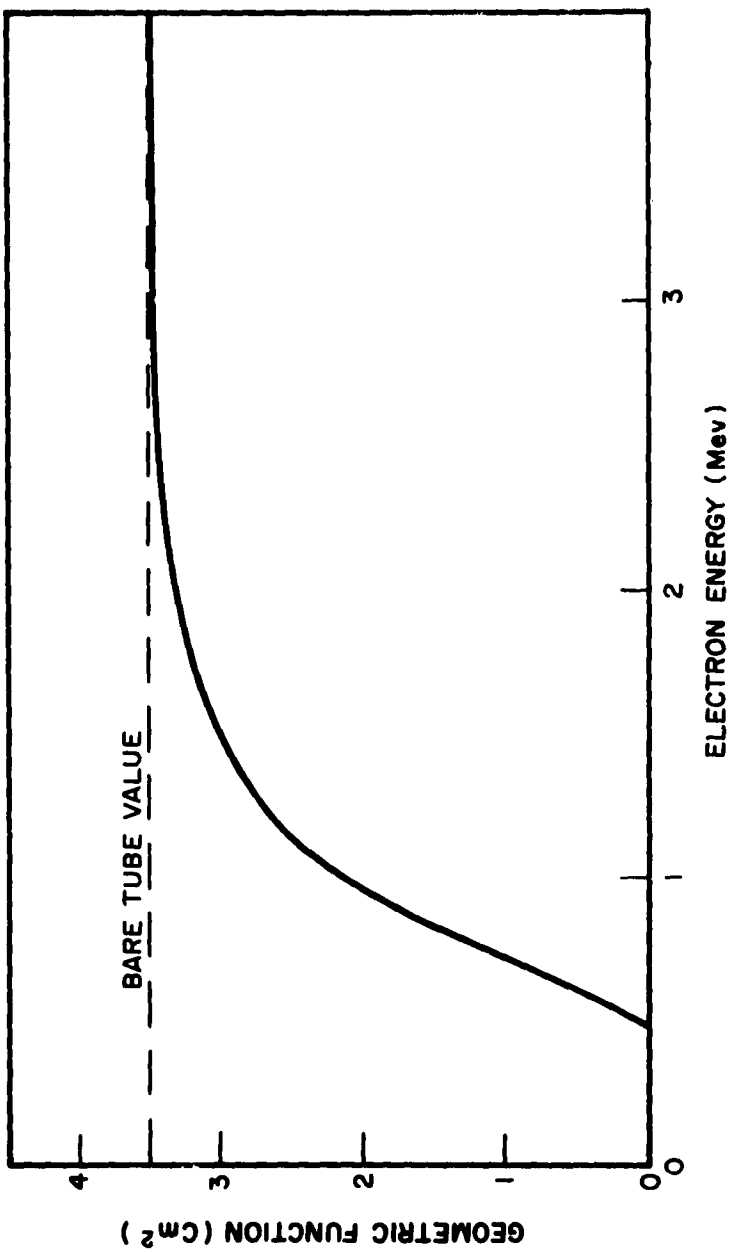

Fig. 3-18b Geometric Function of Detector in Channel 7 With Extrapolation to Bare Tube Value

results obtained at two different values of η but with ψ anywhere in the interval $-25^{\circ} \leq \psi \leq 25^{\circ}$ are shown in Figure 3-19. The results indicated by the circles were obtained at $\eta = 90^{\circ}$, and the crossed lines show the results of the measurements at $\eta = 72^{\circ}$. The threshold energy of this detector is at 940 kev.

Unfortunately, the limited beam energy of the spectrometer highly restricts the full calibration of this detector. It was necessary to extrapolate the geometric function of this detector to that of the "bare" tube value. Since the extrapolation was extreme, a study was undertaken to seek a physical basis for the extrapolation.

The following empirical method was devised for this purpose. (It was also used to compute the geometric function of the detector in Channel 6.) The measured values of the geometric functions of the detectors in Channels 7 and 3 were divided by the "bare" tube value to obtain the effective transmission function of each detector. These transmission curves were found to be systematically lower than the transmission functions for normal-incidence electrons on plane absorbers of corresponding materials and thicknesses. (The normal-incidence transmission data of Marshall and Ward[3] and Hereford and Swann[4] were used in this analysis.) The diminution of the tube transmission from the normal transmission values at each electron energy was caused by the particular distribution of the incidence angles of the electrons on the tube resulting from the irradiation of the cylindrical detector by a planar flux. Hence, the ratio of the tube transmission to the normal transmission plotted against energy should give a curve which reflects the combined effects of the shape of the detector and the angular distribution of the flux. If this is true, then detectors with different shield thicknesses but of the same shape and exposed to the same flux should yield identical ratios of tube transmission to normal-incidence transmission as functions of electron range in units of absorber thickness. Figure 3-20 shows that the agreement of these ratios obtained from the calibration data of the detectors in Channels 7 and 3 is fairly good. The solid curve drawn through the data

---

3. Marshall and Ward; Canadian Journal of Research; A 15, 30 (1937)
4. Hereford and Swann; Phys. Rev. 73, 727 (1950)

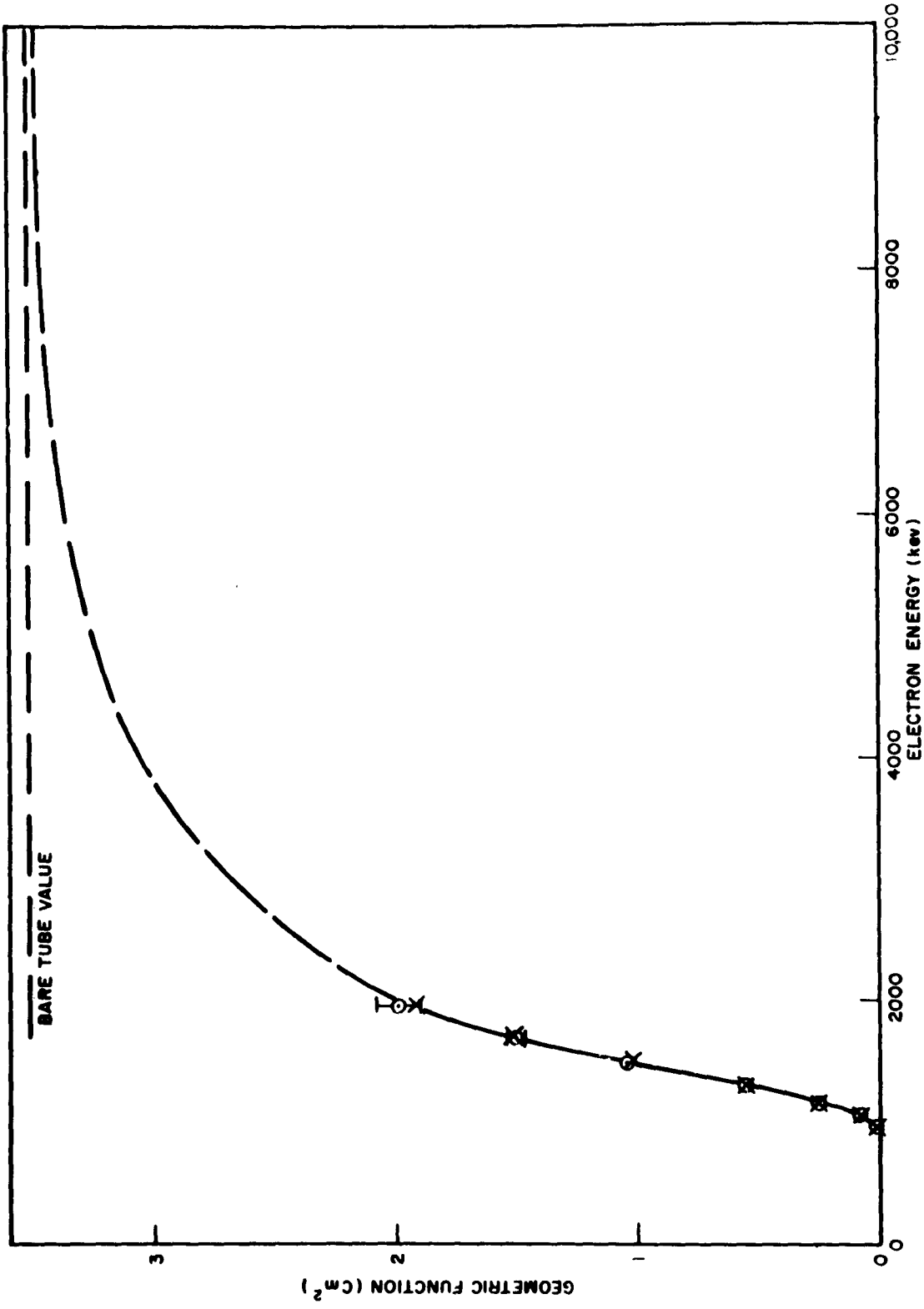

Fig. 3-19 Geometric Function of Detector in Channel 3 for Orientation Angles of $\eta = 90°$ and $-25° \leq \psi \leq 25°$

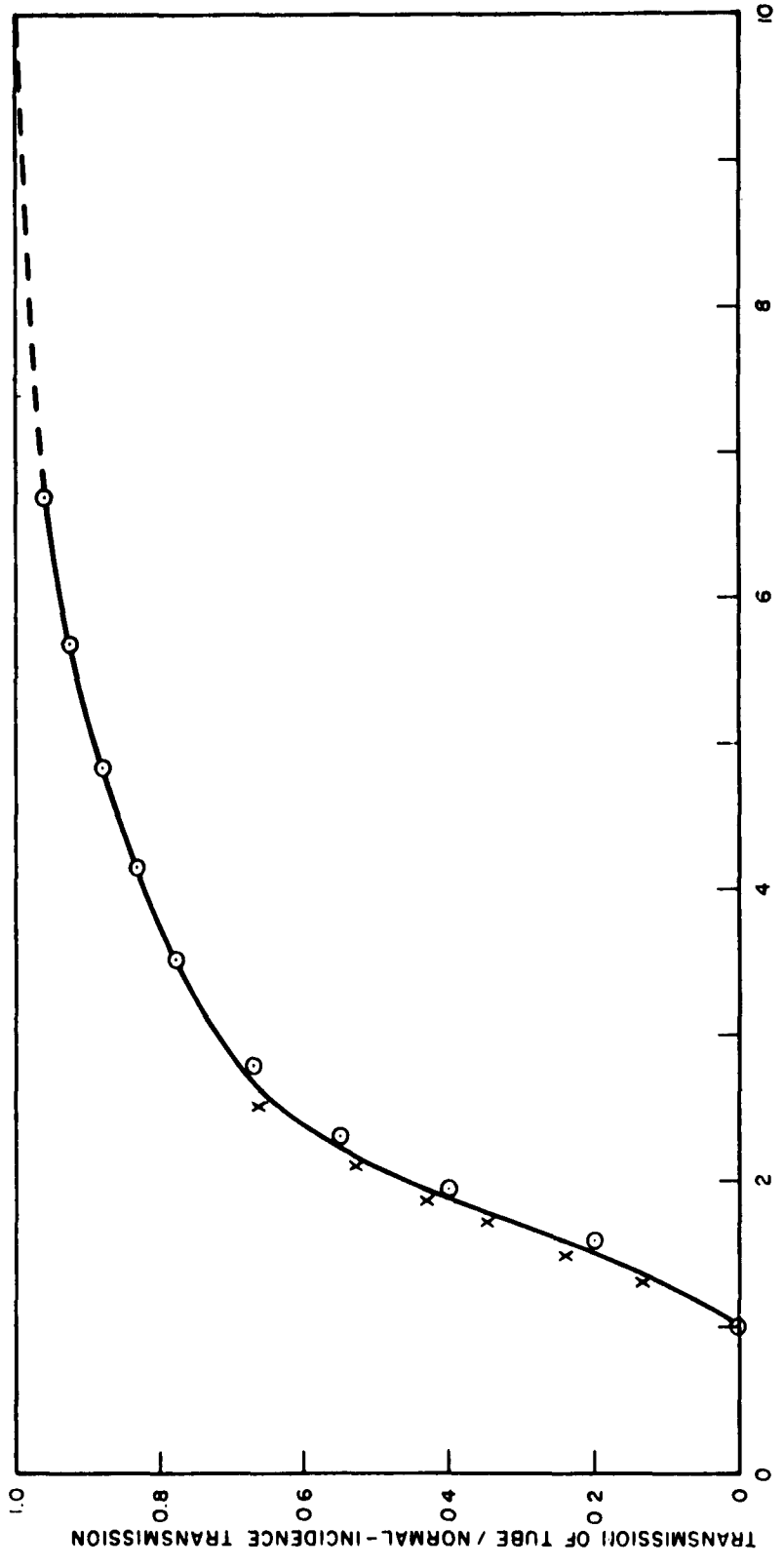

Fig. 3-20 Graph Giving Ratio of Tube Transmission to Normal-Incidence Transmission Versus Range of Electrons of Energy E in Aluminum in Units of the Detector Shield Thickness. The circled points were computed from the calibration data of the detector in channel 7. The points marked X were computed from the channel 3 data

given by both counters was therefore used to extrapolate the geometric function of the detector in Channel 3 to higher electron energies.

The final energy-dependent geometric function of this detector is given in Table A-1.

3.3.4 CALIBRATION OF CHANNEL 6

The detector in Channel 6 also consisted of a shielded Anton 106C geiger tube with no deliberate collimation. This counter was shielded with a cylindrical absorber of brass 2000 mg/cm^2 thick.

In this case the threshold energy of the detector (4.3 Mev) precluded an experimental evaluation of any portion of the geometric function of the detector with the beta-ray spectrometer. Hence, the geometric function was computed by means of the empirical method described above. For this purpose the curve of Figure 3-20 was slightly modified by plotting the transmission ratios against electron range in copper in units of the copper-range of electrons at the threshold energies of the detectors in Channels 7 and 3. This curve, together with the Hereford and Swann normal-incidence transmission data for the absorber (copper) thickness used in Channel 5, were used to compute the transmission function of that detector. The geometric function was then obtained by multiplying this transmission function by the "bare" tube value of the detector in Channel 7.

The resulting geometric function is shown in Figure 3-21 and listed in Table A-1.

3.3.5 CALIBRATION OF CHANNEL 2

The detector in Channel 2 consisted of an end-window Anton 222R geiger tube, with a flat aluminum absorber, about 28 mg/cm^2 thick, placed over the window of the detector, the detector was collimated by means of a circular hole, about 0.10 cm^2 in area, drilled through a brass "plug" at an angle of 30° with respect to the axis of the geiger tube (see Figure 1-1).

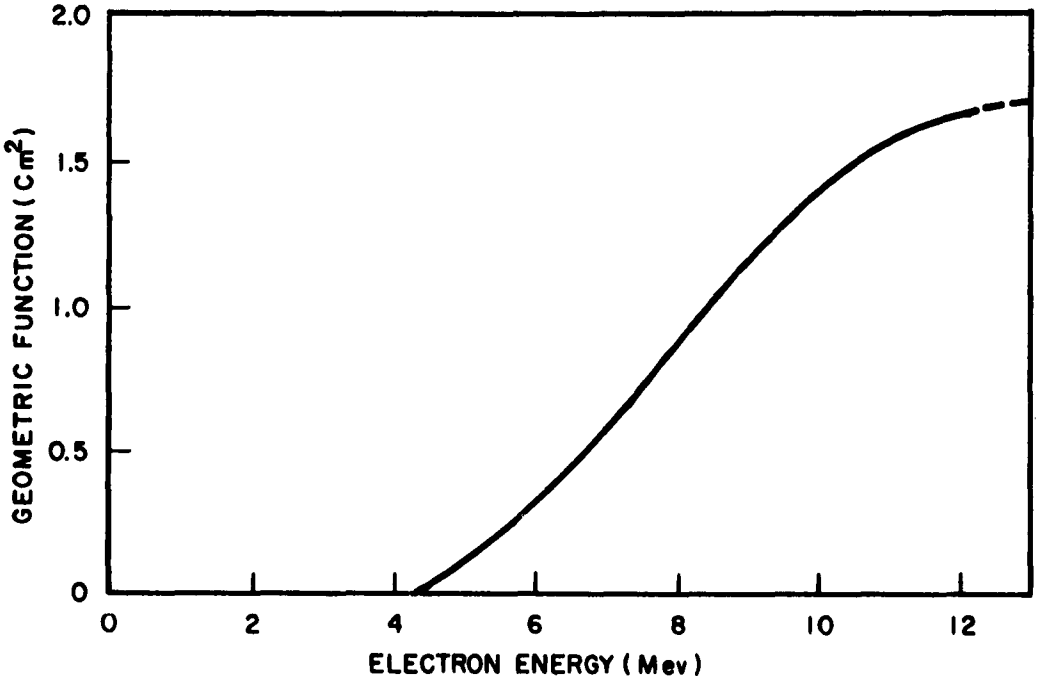

Fig. 3-21 Geometric Function of Detector in Channel 6

Since the collimator aperture was circular, the geometric function of this detector was dependent only on the angular displacement of the collimator axis from the radiation plane. The data from this detector were analyzed by using the counting-rate samples taken when this angular displacement was less than $\pm 10^{\circ}$ as discussed in Section 4. This 10° displacement of the axis corresponds closely to $\psi = \pm 20^{\circ}$ for $\eta = \pi/2$. Hence, the geometric function used for the analysis of the data was that measured for $\eta = \pi/2$ and averaged over $-20^{\circ} \leq \psi \leq 20^{\circ}$. During portions of the precession cycle of a rocket where $\eta \neq 90^{\circ}$, this method of averaging the geometric function does not give the correct average of the function over the displacement angle; however, the maximum deviation due to this cause is 6%, small in comparison with the uncertainty in the collimation of the tube discussed below.

The detector was calibrated by setting $\eta = 90^{\circ}$ (longitudinal axis of geiger tube in radiation plane) and rotating the detector in the beam with the entrance aperture of the collimator centered at the central irradiation point. At each beam energy, a calibration run consisted of about 100 rotations of the turntable. The orientation angle ψ was adjusted by rotating the detector about an axis which was in the radiation plane and which went through the central irradiation point. Calibration runs were taken for ψ angles of -51.0°, -36.5°, -22.6°, -10.4°, 0.0°, 8.8°, 18.2°, 32.6°, 47.4°, and 61.8°. Equation 3-5 was used to compute the geometric functions. The measurements of the geometric functions at $\eta = 90^{\circ}$, $\psi = 18.2^{\circ}$ is shown in Figure 3-22. The threshold energy is seen to fall at 145 kev.

The statistical accuracy of the data, as shown in Figure 3-22, was considerably poorer than that of the long-detectors. Therefore, instead of averaging the geometric functions over the angle ψ as was done for Channel 1, namely, by plotting the functions against ψ using energy as a parameter, all of the data points were used by plotting the integral over energy of the geometric functions against ψ. A graph of the integrated geometric functions versus ψ is shown in Figure 3-23. The average value of this response function over the interval; $-20^{\circ} \leq \psi \leq 20^{\circ}$ divided by the response at the peak is 0.932. Hence, by multiplying the geometric functions obtained

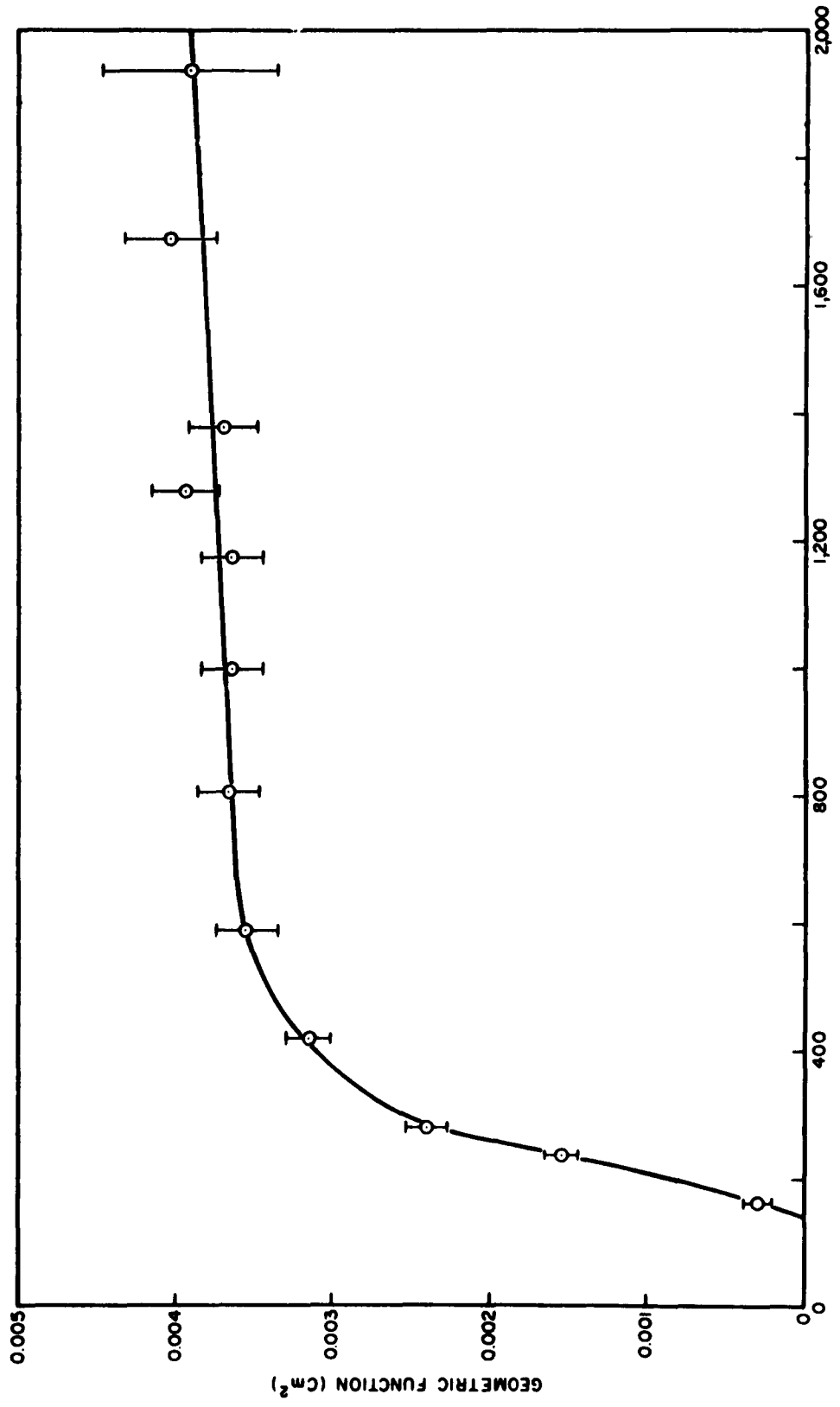

Fig. 3-22 Geometric Function of Detector in Channel 2 for Orientation Angles of η = 90° and ψ = 18.2°

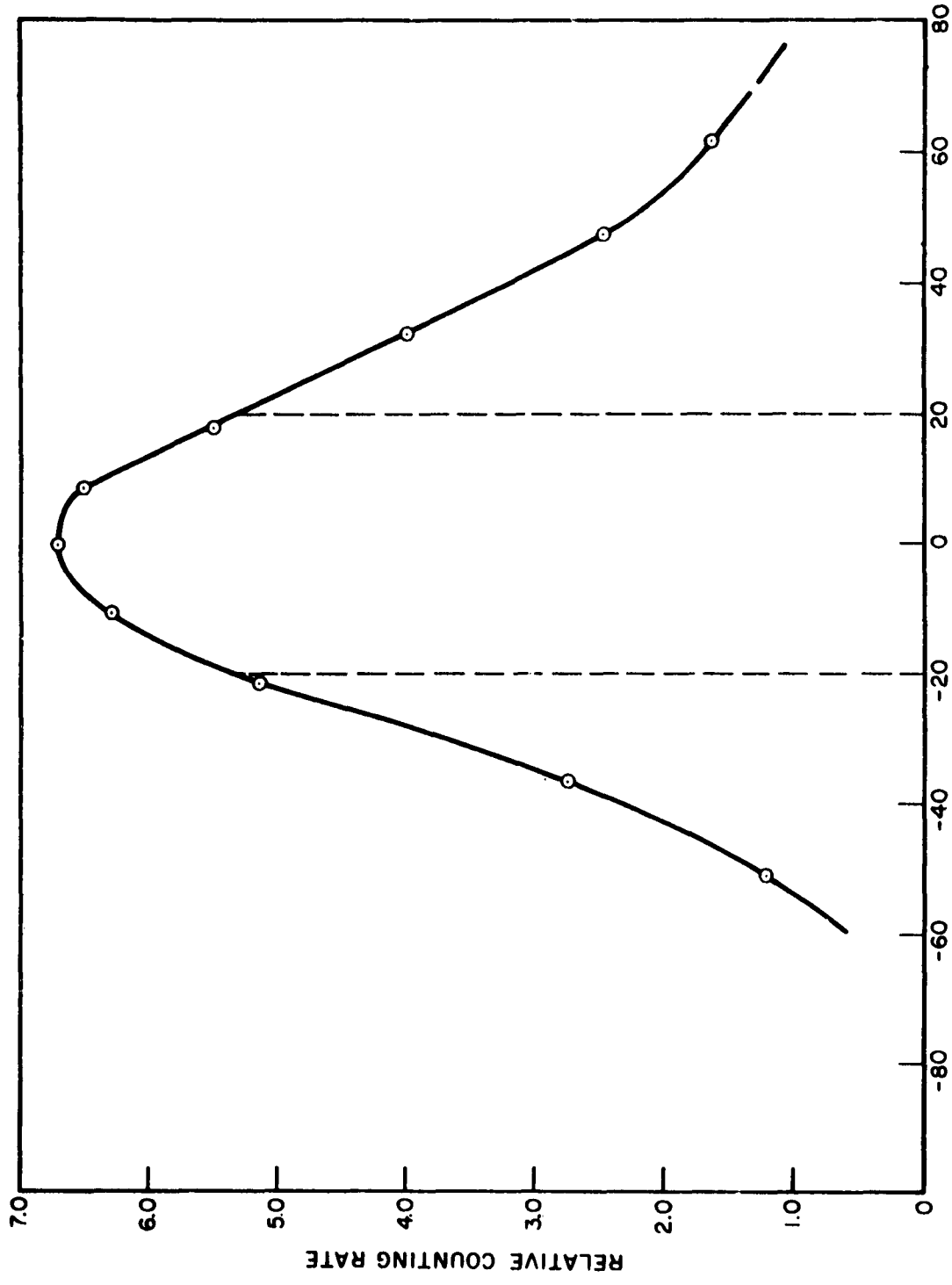

Fig. 3-23 Response of Detector in Channel 2 Versus the Orientation Angle ψ

at $\eta = 90^\circ$, $\psi = 0^\circ$ by this ratio, the final averaged geometric function for the detector was obtained. This is shown in Figure 3-24 and listed in Table A-1.

Unfortunately, the circular aperture of this detector, as well as those of the detectors in Channels 8 and 4, was partially obstructed by a titanium shield which was placed over the geiger tube package. The magnitude of the obstruction depended on the orientation of the counter in the package. Accurate information on the positional setting of counter is not available. An uncertainty in the geometric function of this tube of 15% has been estimated on the basis of the probable variation of the position of the counter.

3.3.6 CALIBRATION OF CHANNELS 8 AND 4

The detectors in Channels 8 and 4 were identical in construction to that in Channel 2, but the absorbers placed in front of the Anton 222R windows differed. The detector in Channel 8 had an aluminum absorber 150 mg/cm^2 thick, and the detector in Channel 4 had a brass absorber, 400 mg/cm^2 in thickness.

Since the geometry of each of these detectors was the same as that of the detector in Channel 2, only the transmission factors of these detectors were expected to vary. Hence, the transmission functions alone were measured for these detectors.

The transmission function of each detector was measured by aligning the collimator in the beam at the central irradiation point and dividing the resulting counting rate of the detector, above cosmic ray background by the product of the beam intensity and the area of the aperture. Figure 3-25 shows the results obtained for the detector in Channel 8. These data agree quite well with the Marshall and Ward measurements (transmission of electrons at normal incidence through 150 mg/cm^2 of aluminum), which are also given in the figure. The threshold energy is 400 kev. The transmission measurements with the 400 mg/cm^2 brass absorber together with the transmission curve given by the Marshall and Ward data for normal-incidence electrons through 400 mg/cm^2 of aluminum are shown in Figure 3-26. These data agree as well as can be

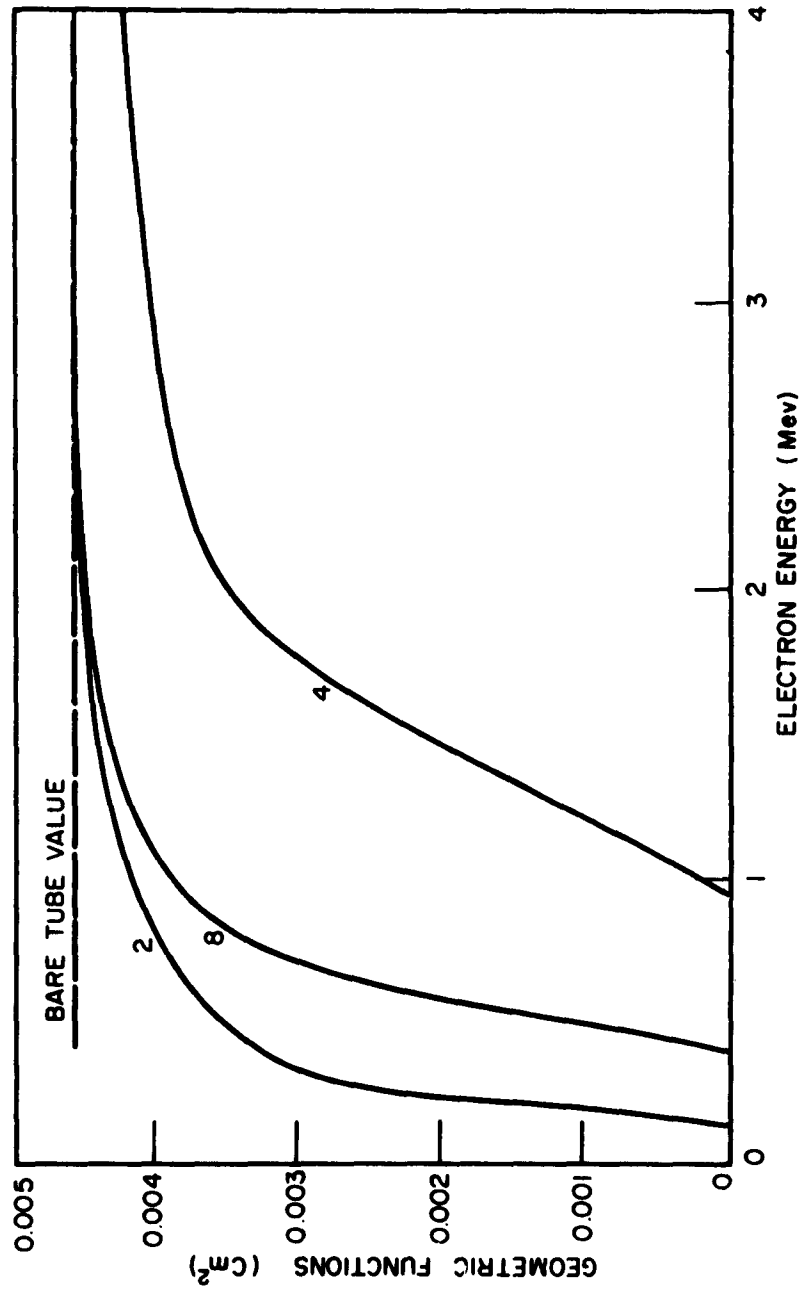

Fig. 3-24 Final Geometric Functions of Detectors in Channels 2, 4, and 8

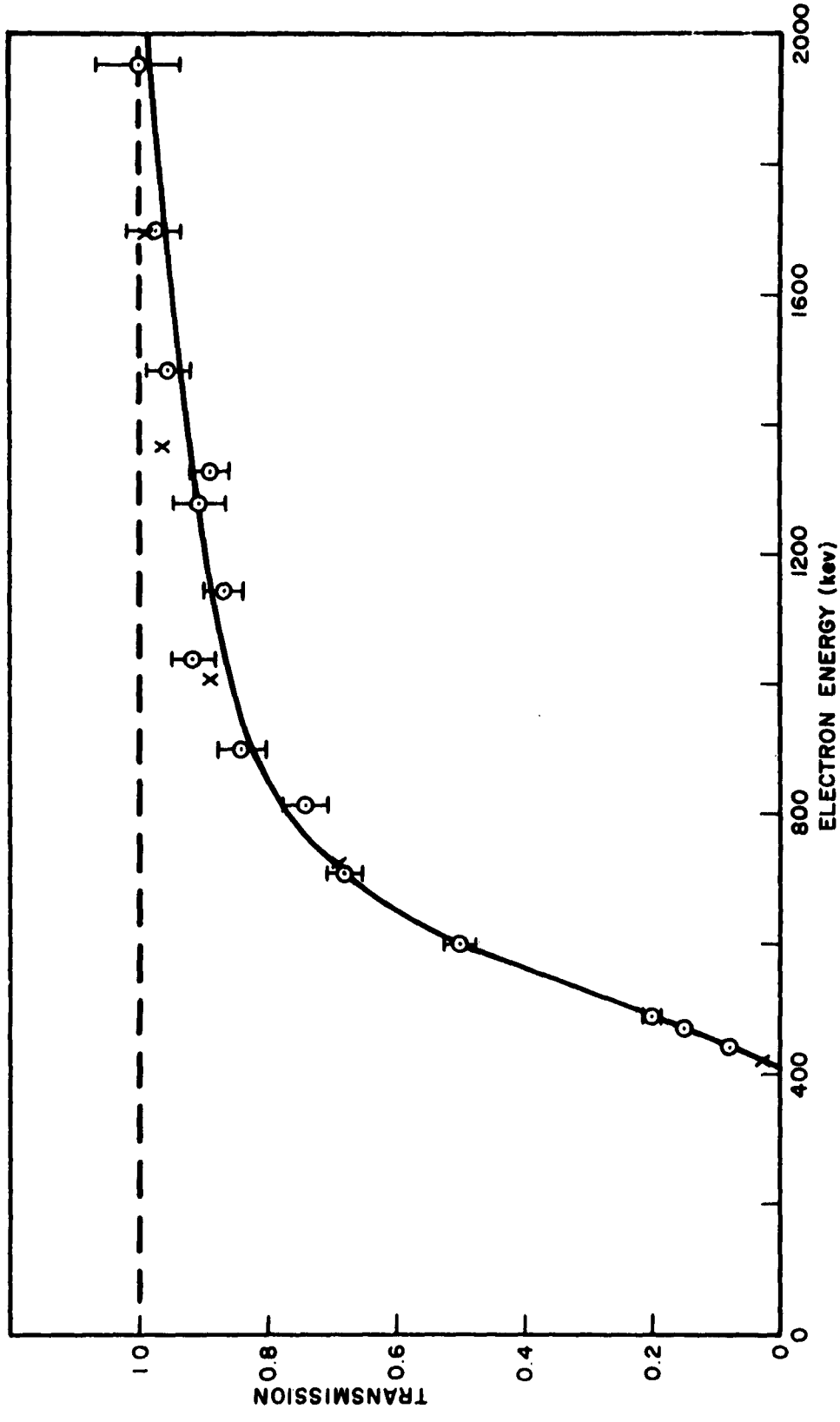

Fig. 3-25 Transmission of Detector in Channel 8

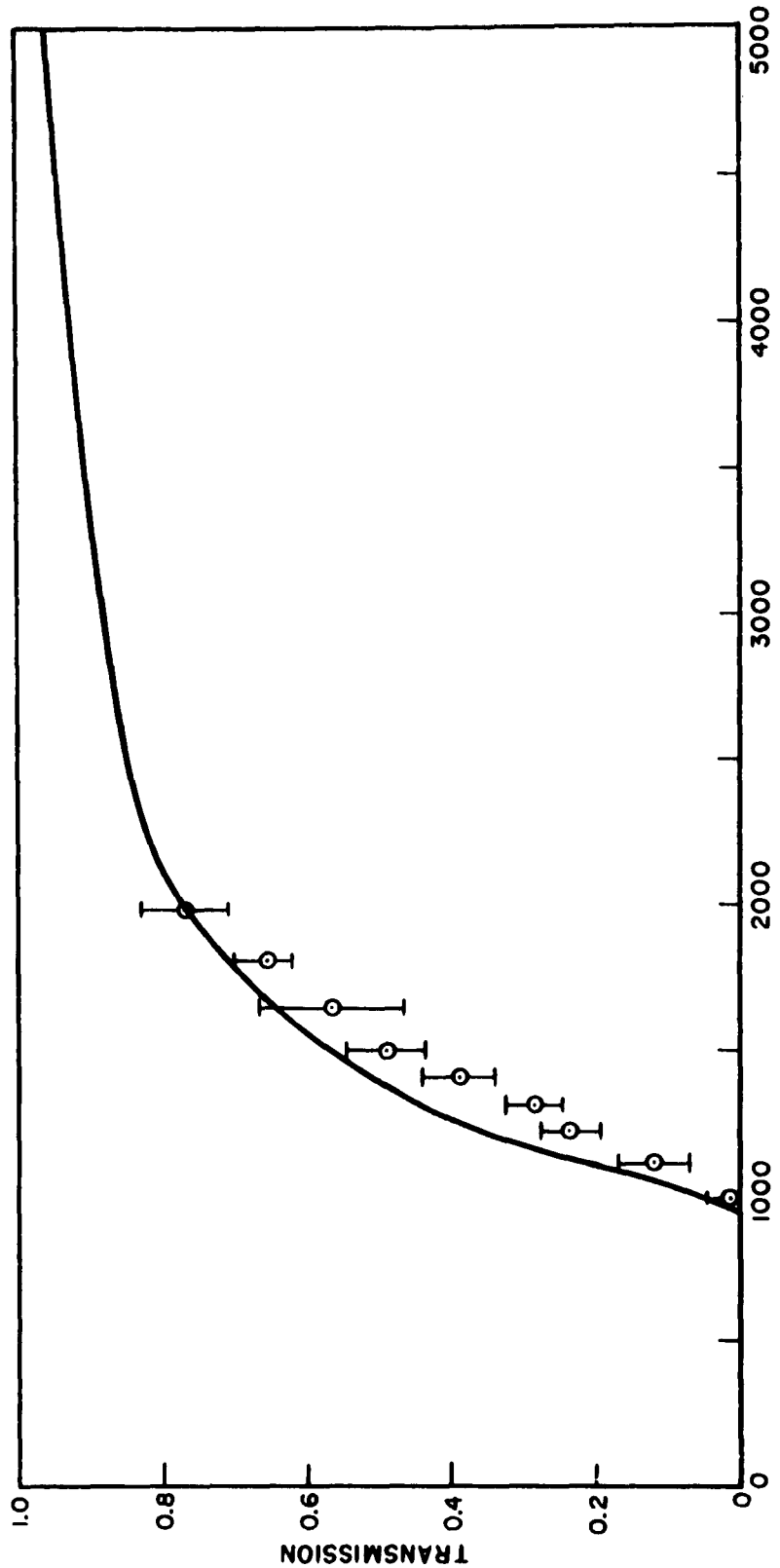

Fig. 3-26 Transmission of Detector in Channel 4

expected in view of the different absorber materials used. Since a relatively short extrapolation of the data to higher energies was required, the Marshall and Ward curve was used to compute the geometric functions for energies greater than 2.0 Mev. The threshold energy of this detector is 1.00 Mev.

The "averaged" geometric functions of these detectors were obtained by multiplying the transmission functions of the detectors by the maximum value of the geometric function of the detector in Channel 2 given in Figure 3-24. The results are depicted in Figure 3-24 and listed in Table A-1.

3.3.7 COMPARISON OF CALIBRATION RESULTS WITH INITIAL ANALYSIS OF DETECTORS

In order to compare the experimental values of the geometric functions of the detectors with those which were computed (SWC 50-TS-112) for the preliminary investigation of the data, the geometric functions were represented as a product of the transmission function of the tube and the geometric tube factor. The function was obtained experimentally at each energy E by dividing the counting rate of the detector by the value of the planar flux of electrons of that energy. Hence, the geometric factor of the counter was taken to be the geometric function for $E >> E_t$, where E_t represents the threshold energy of the counter. The transmission function of the tube was then obtained by dividing the geometric function by the geometric factor. The following comparison was observed between the experimental values for $\eta = 90^\circ$, $\psi = 0^\circ$ and the values computed for "Orientation B" given in SWC 50-TS-112.

Channels 1 and 5: The measured geometric factor was about 30% smaller than the computed value. The slope of the transmission function was less than the SWC-report value by nearly a factor of two. (The $2 g/cm^2$ copper plugs in windows 1, 5 and 6 diminished the geometric factor by a factor of 0.652 instead of 0.5).

Channels 3 and 7: The geometric factors were smaller than those given in the SWC report by 18%. The transmission functions were in fairly good agreement.

Channels, 2, 4 and 8: The measured geometric factors were found to be smaller than those given in the SWC report by about 40%. The transmission functions agreed fairly well.

Channel 6: The empirical method which was used to determine the calibrations of Channel 6, described in Section 3.3.4, is considered to be fairly good because of the agreement obtained by testing the method with the results of Channel 3. This method yielded a response function for Channel 6 which is much lower than the function given in the SWC report at energies near the threshold value, being smaller by a factor of ten at 5 Mev and by a factor of two at 10 Mev.

Moreover, the initial analysis indicated a factor of three discrepancy between the flux given by the geometric factors of the long counters and that given by the short detectors. This discrepancy does not occur when the measured geometric functions are used.

4. ANALYSIS OF RESULTS

4.1 PRESENTATION OF "RAW" DATA

The "raw" data here refer to the counting rates of the detectors as a function of time. The computer read-out records listed, for each sample of the output of a detector, the time of the sample, the corrected counting rate, and the orientation angles η and ψ . Of these counting rates, only those which were sampled when ψ occurred in the interval $-20^\circ \leq \psi \leq 20^\circ$ for the long detectors were used; and, for the short detectors only the counting rates which were sampled when the collimator axes were within $\pm 10^\circ$ of the radiation plane were used in the analysis. Data which were obtained at larger displacements were discarded because the geometric factors of the detectors began to change rapidly with angle, and large errors probably would have ensued due to the non-planar nature of the actual flux.

Before experimental information on the calibration of the detectors was obtained, it was hoped that the energy dependence of the geometric functions of the long detectors would vary with η and ψ so that a more detailed spectrum could have been obtained. However, essentially no change in the shape of the geometric functions was observed in the angular ranges $69^\circ \leq \eta \leq 111^\circ$ and $|\psi| \leq 20^\circ$ as pointed out in Section 3. This η - orientation angle for the long detectors was therefore ignored.

The samples of the counting rates which occurred within the angular intervals discussed above were then averaged over time durations for which continuous data of counts per pedestal were available (5 to 12 seconds). The process was straightforward for the long detectors: the counting rates which were read-out during $|\psi| \leq 20^\circ$ were merely added and divided by the total number of samples. However, for the short detectors, it was necessary to vary the ψ -angle interval over which the counting rates were accumulated in a manner which was dependent on η . This was accomplished by plotting two curves of η versus ψ which established the limits of these angles for a collimator displacement from the radiation plane within $\pm 10^\circ$. The displacement, δ , of the collimator from the plane is given by the equation,

$$\sin \delta = \cos 60^\circ \sin \eta \left[\sin (\psi - \nu) - 60^\circ \operatorname{ctn} \eta \right] . \quad (4\text{-}1)$$

The counting rates of the detectors, averaged as discussed above, for the five rockets which passed through the electron shell are listed in Tables 2 through 6 of the appendix. The tables are numbered in the order of the launch times of the rockets. The time interval between the launch times and the burst time for each of the rockets is given below:

Rocket Flight	Time of Launch after Burst
	Hr:Min
2019	0:28
2021	1:58
2024	4:01
2027	18:42
2042	88:43

After averaging some of the counting rates given in the tables over larger time intervals where necessary to improve the statistical accuracy, the resulting counting rates were plotted as a function of the flight time of the rockets. These data are shown in Figures 4-1 through 4-5, again in the order of the launch times of the rockets.

The errors given both in the tables and in the figures are standard deviations based only on the total number of counts used in the averaging process. At high counting rates the major errors are due to uncertainties in the determination of the counts per pedestal and the uncertainty of the "dead time" correction. Systematic errors as high as 50% or more may have been incurred at counting rates above about 10^4/sec. The probable errors P_{R_T} of the corrected counting rates R_T due to these causes is,

$$P_{R_T} = \sqrt{P_N^2 + R_o^2 P_\tau^2}\; R_T/(1 + R_o \tau),$$

where R_o = observed counting rate, $15.75\ N/T_c$. N is the number of counts sampled during the time $T_c/15.75$. T_c is the period of the commutator.

P_N = probable fractional error of N due to reading of oscillograms.

P_τ = probable error of dead time τ .

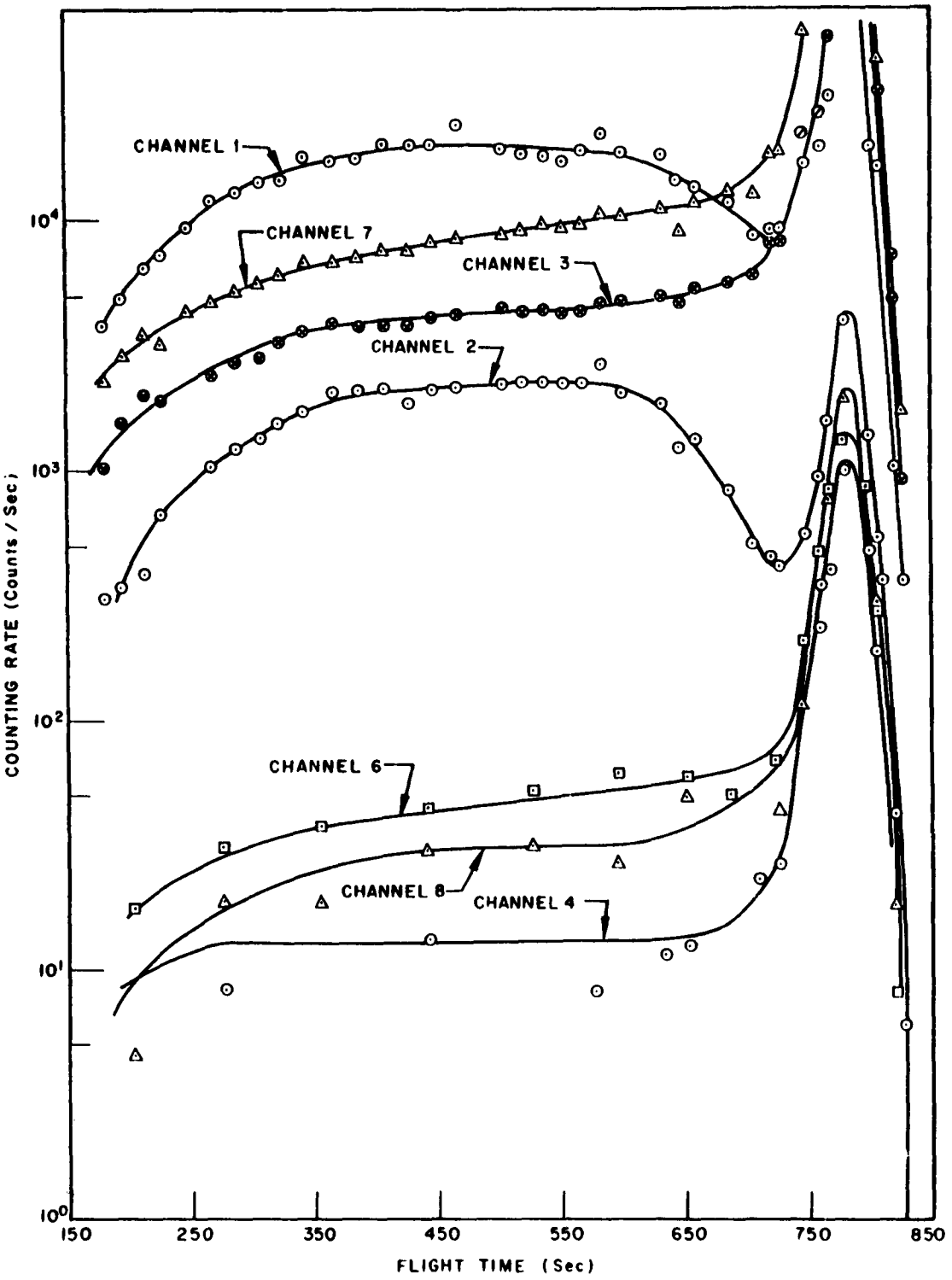

Fig. 4-1 Counting Rates of Detectors on Flight 2019 as Function of Flight Time

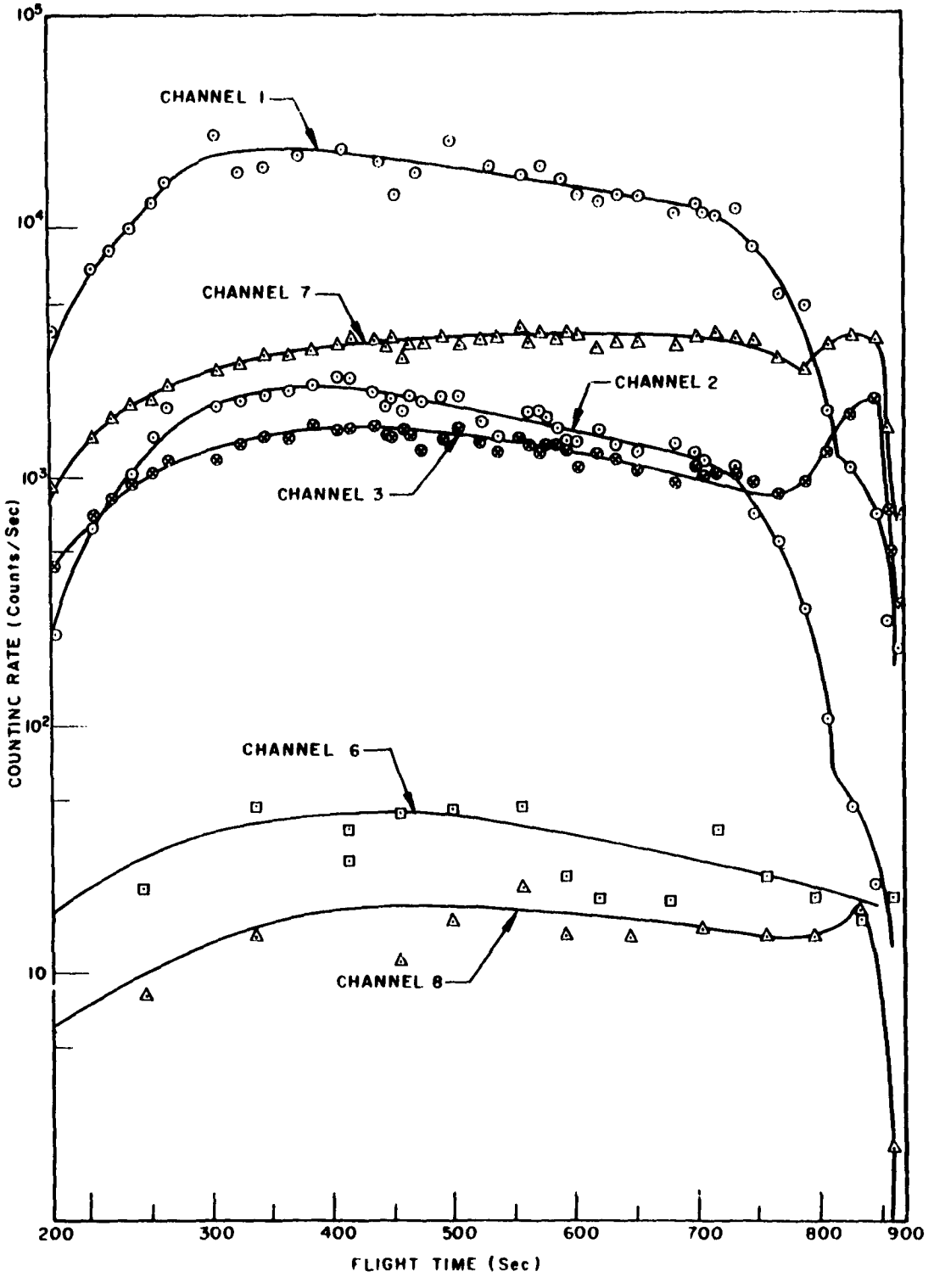

Fig. 4-2 Counting Rates of Detectors on Flight 2021 as Function of Flight Time

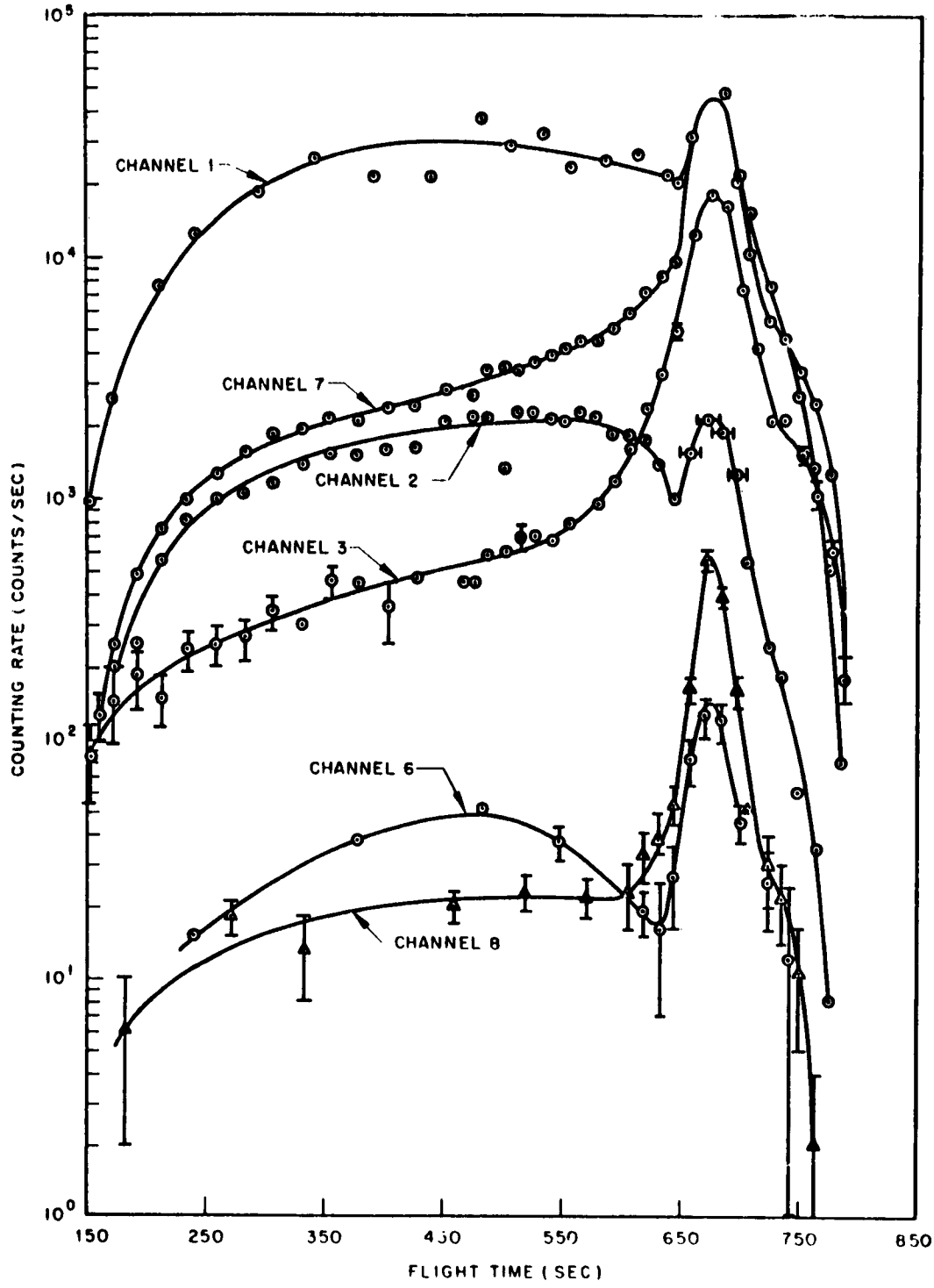

Fig. 4-3 Counting Rates of Detectors on Flight 2024 as Function of Flight Time

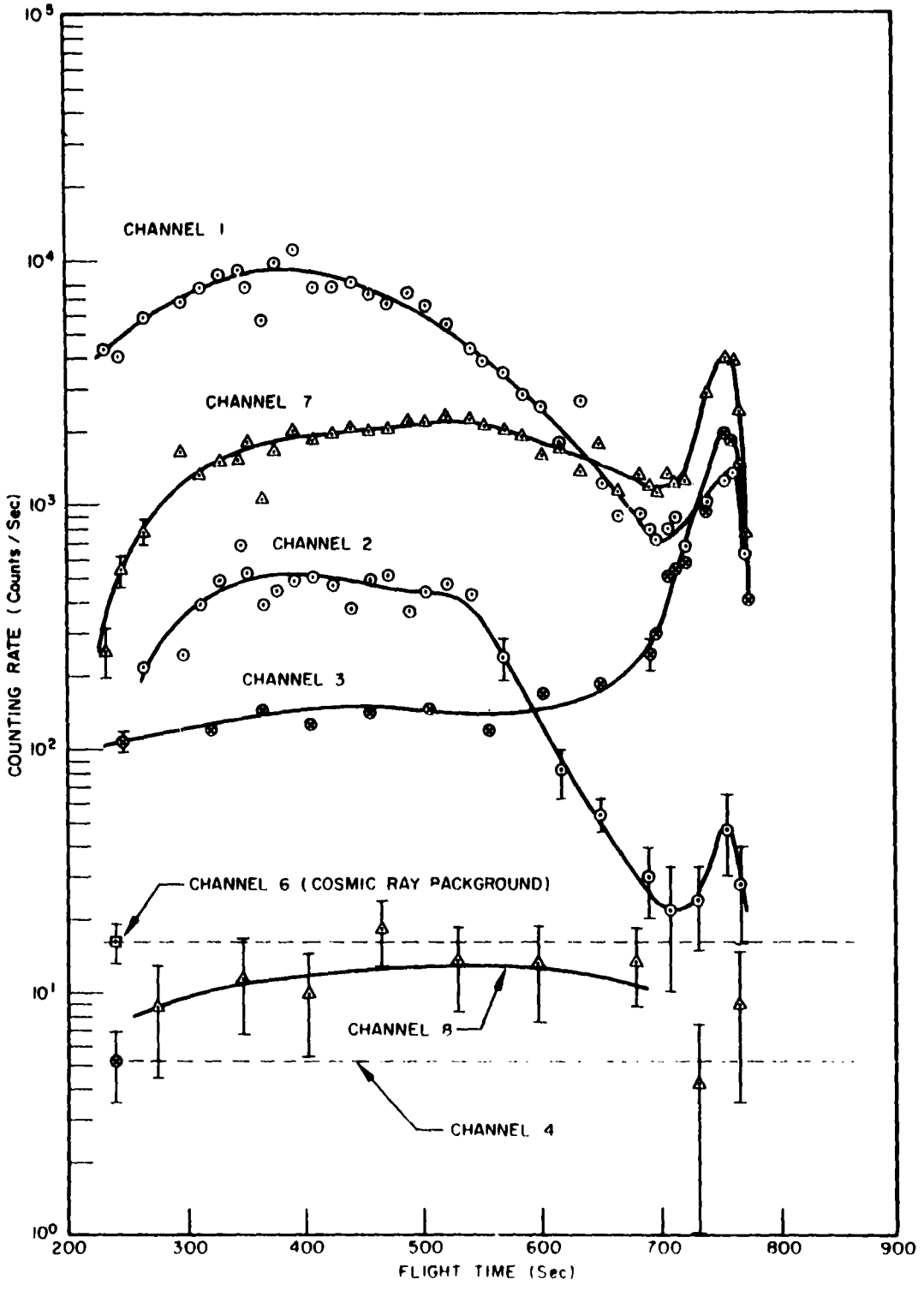

Fig. 4-4 Counting Rates of Detectors on Flight 2027 as Function of Flight Time

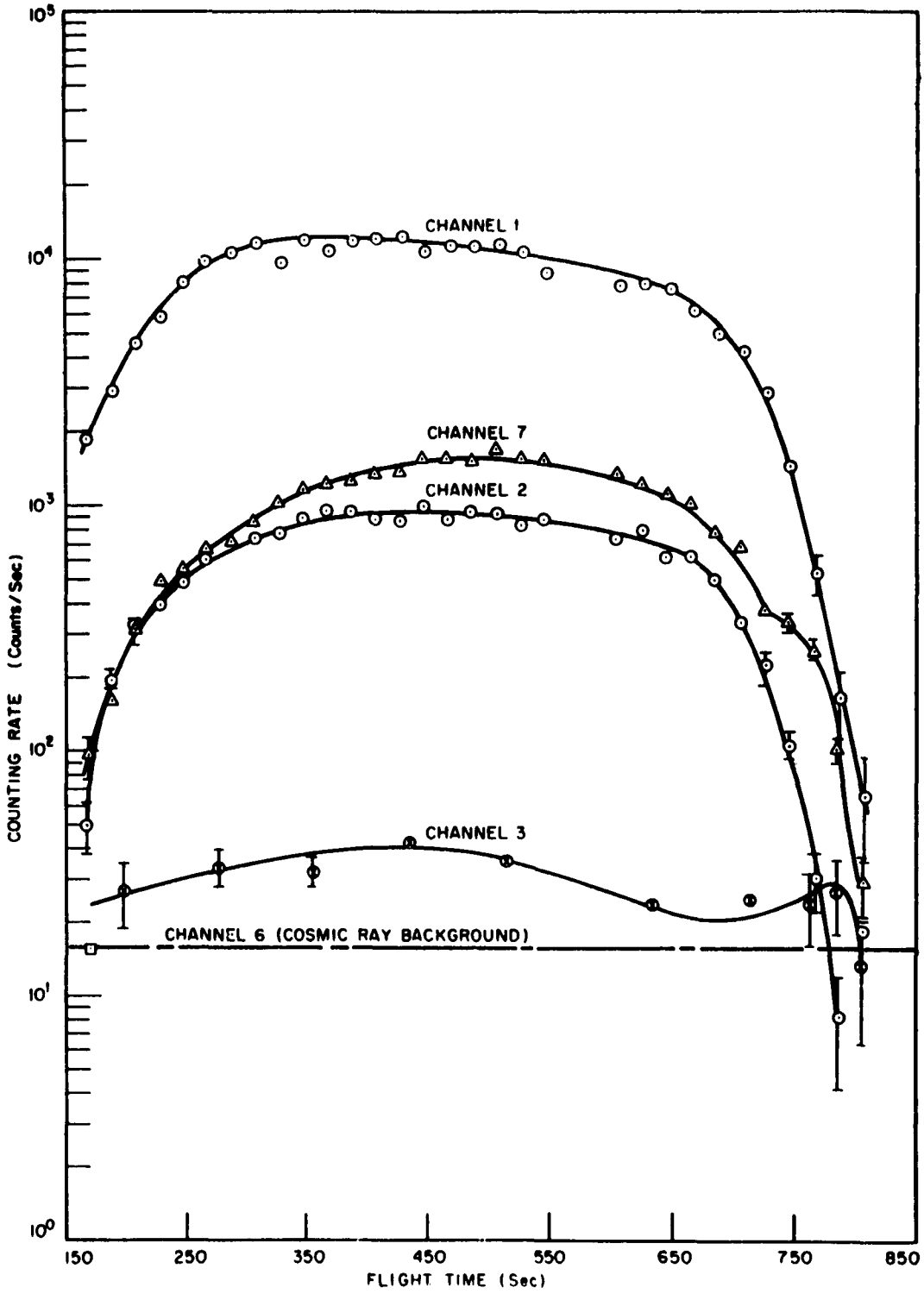

Fig. 4-5 Counting Rates of Detectors on Flight 2042 as Function of Flight Time

These errors are listed in Table 4-1. P_γ was taken to be 10 microseconds.

Table 4-1

Probable Errors Due to Data Readout and Uncertainty of Dead Time Correction

N (Counts)	P_N	R_T (Counts/sec)	PR_T (Counts/sec)
10	0	960	10
20	0	2060	42
30	0	3330	230
40	.025	4810	400
50	.050	6570	640
60	.075	8680	1580
70	.100	11,300	2380
80	.125	14,500	4850
90	.150	18,700	7350
95	.162	21,300	9180
100	.175	24,300	14,400
105	.187	27,900	18,200
110	.200	32,200	23,400
115	.225	37,500	30,600
117	.250	40,000	34,400

These counting rates can be correlated with the position of the rockets in space as well as with the locations of the rockets with respect to geomagnetic lines of force with the information given in Tables 7 through 11 of the appendix and in the Figures 4-6, 4-7, and 4-8. These tables list, against the "flight time" of a rocket, the geographical coordinates of the rocket; the magnetic field intensity, B; the logarithm of the integral invariant, I; the altitude of the rocket transformed along constant local B and I values to

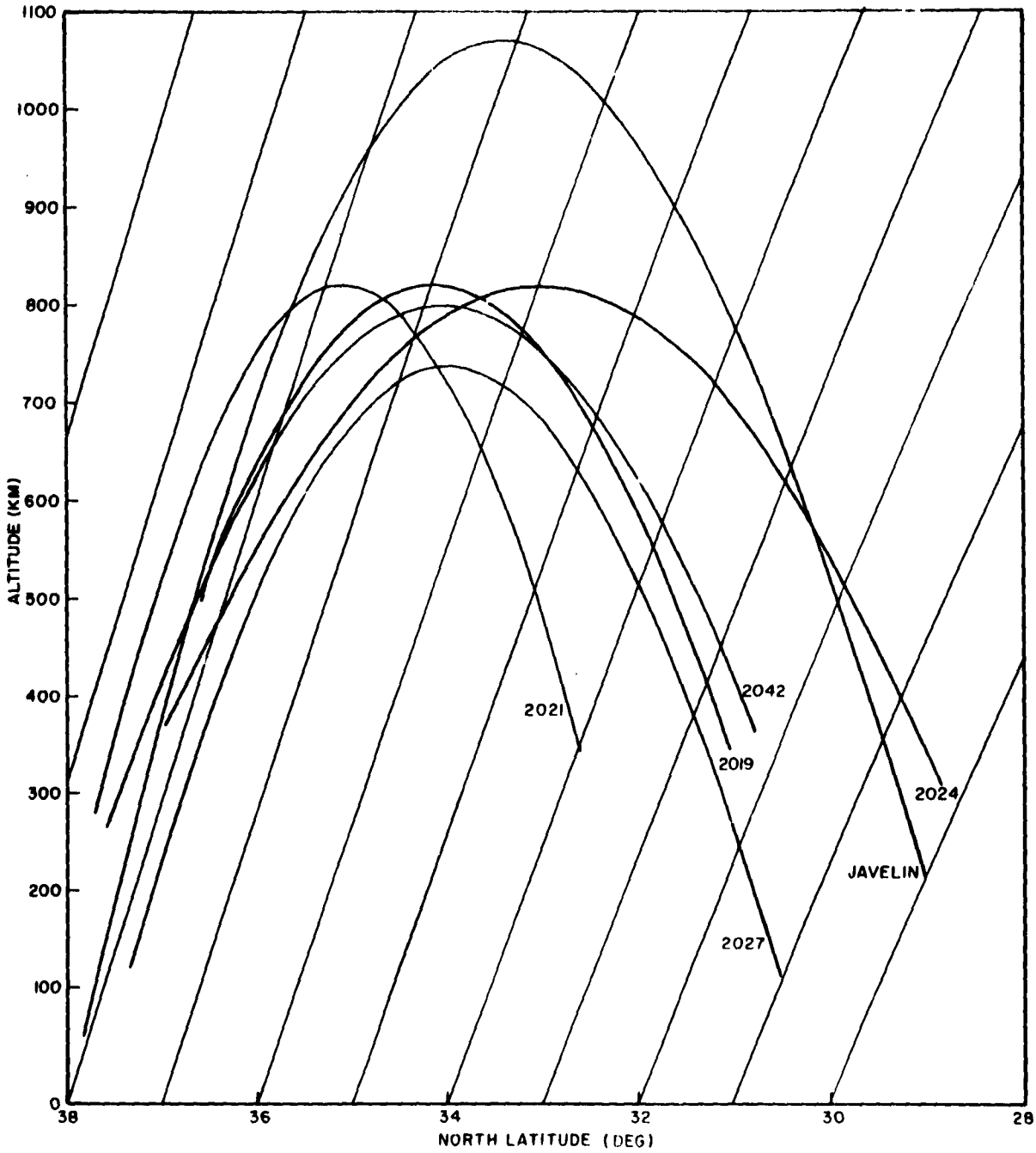

Fig. 4-6 Trajectories of Javelin I and Jason Rockets Projected in Meridian Plane at 75° West Longitude. The projection of the trajectories to this plane was done by following the altitude variations of local, but constant, B (geomagnetic field intensity) and I (integral invariant) values with longitude. Magnetic lines of force which intersect the surface of the earth at every degree of latitude are also shown. The electron shell was centered on the magnetic line of force which intersected the earth's surface at a latitude of about 33.6°.

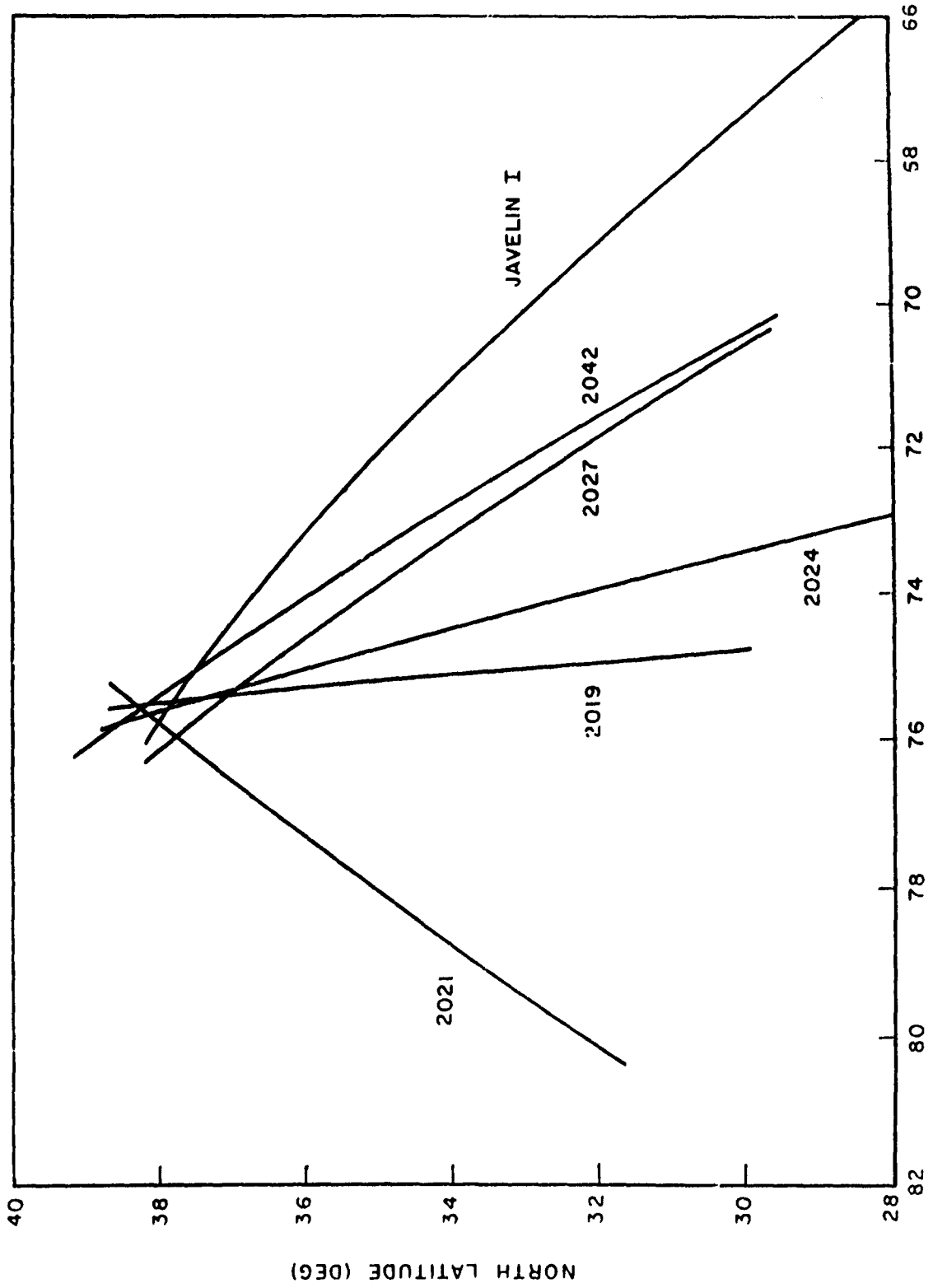

Fig. 4-7 Projection of Trajectories of Javelin I and Jason Rockets on Surface of Earth. Intersection on earth's surface of radial line from center of earth to position of rocket in flight

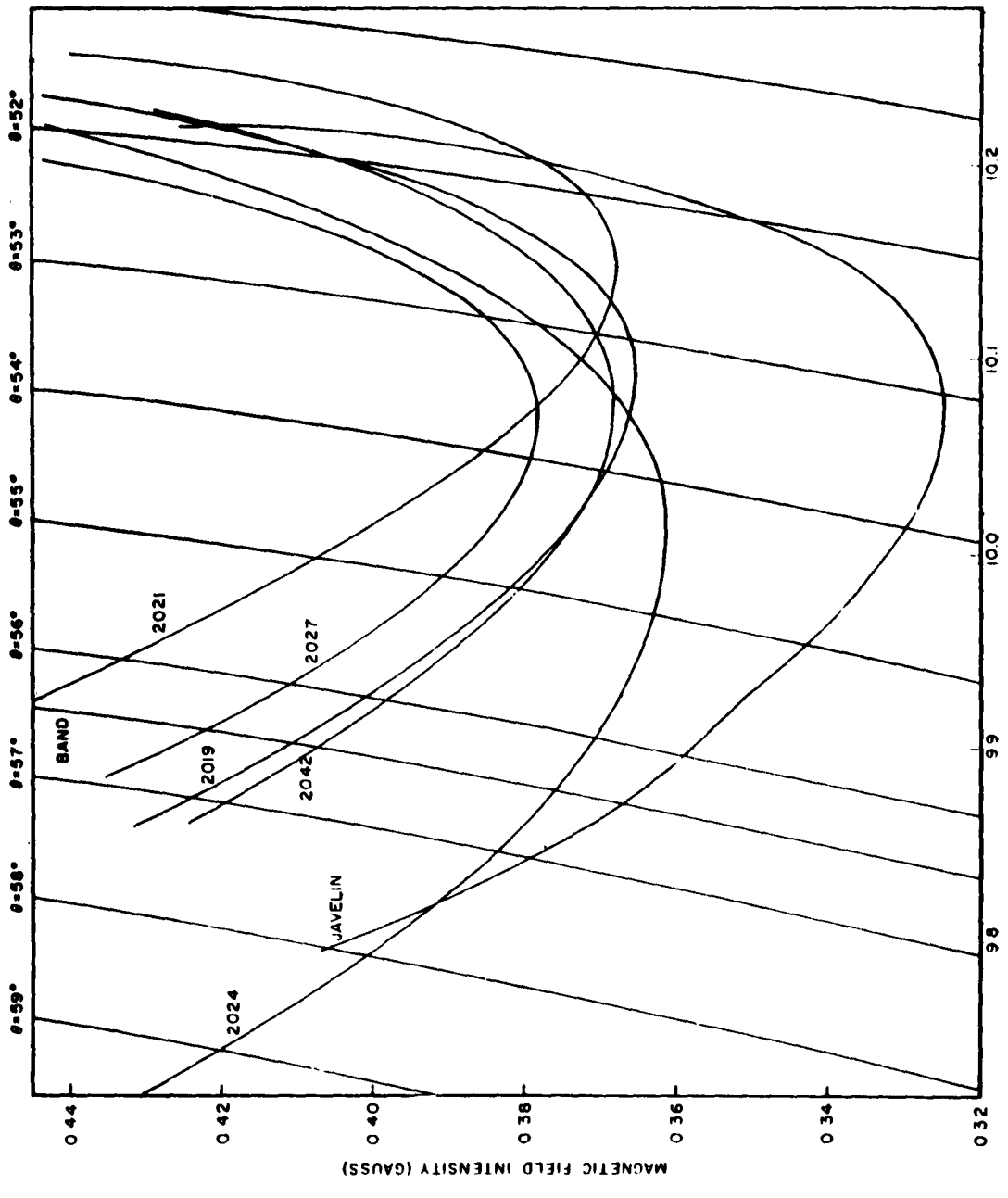

Fig. 4-8 Trajectories of Javelin I and Jason Rockets on B-Log I Plot. Magnetic lines of force which intersect the earth's surface at every degree of colatitude are also shown. The electron shell is centered on the line drawn at 56.4° (33.6° north latitude)

the geographic meridian at 75° West longitude,* H'; and the conjugate mirror-point altitude (southern hemisphere) of electrons which mirror at the location of the rocket. (The last column will be referred to in a later discussion.)

The counting rates of the detectors, when compared in this manner, show that the peak counting rates on flights 2019, 2021, 2024, and 2027 occurred when the trajectories of the rockets reached a shell containing the magnetic line of force which intersects the earth's surface at the point 33.6° North latitude, 75° West longitude. The pronounced rise to the peak generally began when the rockets reached the shell containing the magnetic line of force which falls at the surface of the earth at about 34.5° North latitude along the same meridian. High counting rates also occurred at greater distances to the North of the electron shell (the wings). The counting rates of all of these detectors on different flights but at comparable spatial locations decrease with time.

---

* The B and I values used for the analysis described in this report were obtained from the following reference: Tables of Adiabatic Invariants for Geomagnetic Field 1955.0, AFSWC-TN-60-8, Kirtland Air Force Base, New Mexico, 1960.

4.2 BACKGROUND RADIATION

4.2.1 NATURAL RADIATION

A large effort was directed towards the evaluation of the background due to the natural trapped electrons for each of the flights. The result of this effort was less than satisfactory. The problem was greatly complicated because the rockets traversed spatial regions where the natural radiation is known to be highly irregular. In general, the variation of this radiation is such that it decreases with increasing longitude, it increases rapidly with increasing altitude along magnetic lines of force, and it increases even more rapidly across magnetic lines of force towards higher latitudes.

The Javelin I rocket data (see footnote 2 on page 1), which yielded the spectrum and intensity, as well as pitch angle distributions, of the trapped electrons in spatial regions similar to those covered by the Jason rockets, verified the complexity of the background problem. This rocket was launched from Wallops Island, Virginia, on July 7, 1959, about 10 months after the Argus tests. Its trajectory is shown in Figures 4-6, 4-7, and 4-8, together with those of the Jason rockets. By multiplying the spectral intensity of the flux obtained with the Javelin rocket by the geometric functions of the Jason detectors and integrating over energy (see Equation (1-1), the counting rates of the Jason detectors along the Javelin trajectory were inferred. For the purposes of this discussion, the Jason detectors for which the counting rates were computed in this manner will be referred to as though the detectors were actually on the Javelin rocket.

A comparison of the counting rates of the detectors on the Jason rockets with those on the Javelin revealed that in the wings, a high fraction of the counting rates of the detectors in Channels 1 and 2, and a lower fraction in Channels 7 and 8 were due to the natural radiation. In fact, a plot of the counting rates of the detectors in Channel 1 for the five Jason flights and the Javelin flight as a function of altitude revealed that the counting rates of all of the detectors agreed to within 10% along the ascent trajectories to an altitude of 600 km. This good agreement with the Javelin data was probably accidental since the absolute measurement of the flux is not expected to be better than about $\pm$ 20%. At higher altitudes, a separation of

the counting rates was observed, with the counting rate of the detector on the Javelin rocket exceeding the rates of the detectors in the Jason rockets because of the continuation of the Javelin rocket up the magnetic line of force.

Efforts to determine the background of the Jason Channel 1 detector were not entirely successful. Estimates of the background were made by drawing iso-count lines connecting positions on the ascent and descent paths of the Javelin rocket, where the counting rates for Channel 1 were identical, and assigning these rates to the corresponding Jason detectors at the spatial locations where these lines intersect at the Jason rocket trajectories. Such interpolations were attempted using the graph of altitude versus latitude given in Figure 4-6, and the graph of the trajectories on the B, log I plot of Figure 4-8. The resulting background counting rates of the detectors, when plotted against the flight time of the rockets, gave curves which disagreed somewhat with the shapes of the total counting rates of the Channel 1 detectors. Moreover, over some regions of the curves for flights 2027 and 2042, the background counting rates exceeded the total counting rates of the detectors.

It was clear that a more precise computation of the variation of the natural radiation was required. Various empirical approaches were attempted, based on the variations of the mirror-point altitudes in the southern hemisphere of the electrons detected by the rockets. A comparison of the altitude of the rocket and the value listed as H_s in Tables A-7 through A-12 shows that the mirror-points altitudes of the electrons in the southern hemisphere were much lower than those at the rocket, and this lowering effect was enhanced as the rockets moved eastward. The results gave background curves which again appeared to be qualitatively correct, but they, too, exceeded the total counting rates in some areas.

It was finally decided that the detectors in Channels 1, 5 and 2 could not be used to investigate the artificially injected electrons in the regions of the wing where the natural radiation was intense.

Moreover, the accuracies of the results from the detectors in Channels 7 and 8 were seriously impaired. The background counting rates of the Channel 7 detectors computed from the Javelin data were about a factor of two lower than the total counting rates of these detectors in the wings on flights 2027 and 2042. The total Channel 7 counting rates probably included contributions due to bremsstrahlung from the natural radiation as discussed below.

Hence, the background corrections in the wings for the Channel 7 detectors were made by assuming that the counting rate of the Channel 7 detector on flight 2042 had reached the background level and that this natural background level was the same for all of the flights. The rocket trajectories on a B-log I plot (Figure 4-8) were used to determine these backgrounds: At each point of a trajectory, the background was obtained by means of a log I-weighted average, at constant B, of the Channel 7 counting rates measured on the ascent and descent trajectories of the 2042 rocket. This evaluation is expected to be poor for the portions of the rocket trajectories which depart appreciably from the path of flight 2042. Hence, the Channel 7 backgrounds for flight 2021, which has a westward velocity component (see Figure 4-7), and for flight 2024 beyond apogee (see Figure 4-8) are considered to be poorly known. The counting rates of the Channel 7 detectors on flights 2019, 2021, 2024 and 2027, together with the background curves given by this method, are shown in Figures 4-9 through 4-12, respectively, and they are listed in Table 4-2. The probable errors of the background counting rates for flights 2019, 2027, and a portion of 2024 were taken to be 20%, the extent of the agreement with the Javlin I data along the ascent trajectories. The errors were arbitrarily taken to be $\pm$50% for flight 2021 and for the portion of flight 2024 beyond apogee. Table 4-2 also lists the net counting rates of the Channel 7 detectors. Total probable errors are included.

4.2.2 BACKGROUND DUE TO PREVIOUSLY DETONATED DEVICES

Comparison of the counting rates of the Channel 1 detectors on Patrick launched flights 1822, 1909, 2020, and 2043 at similar positions of the

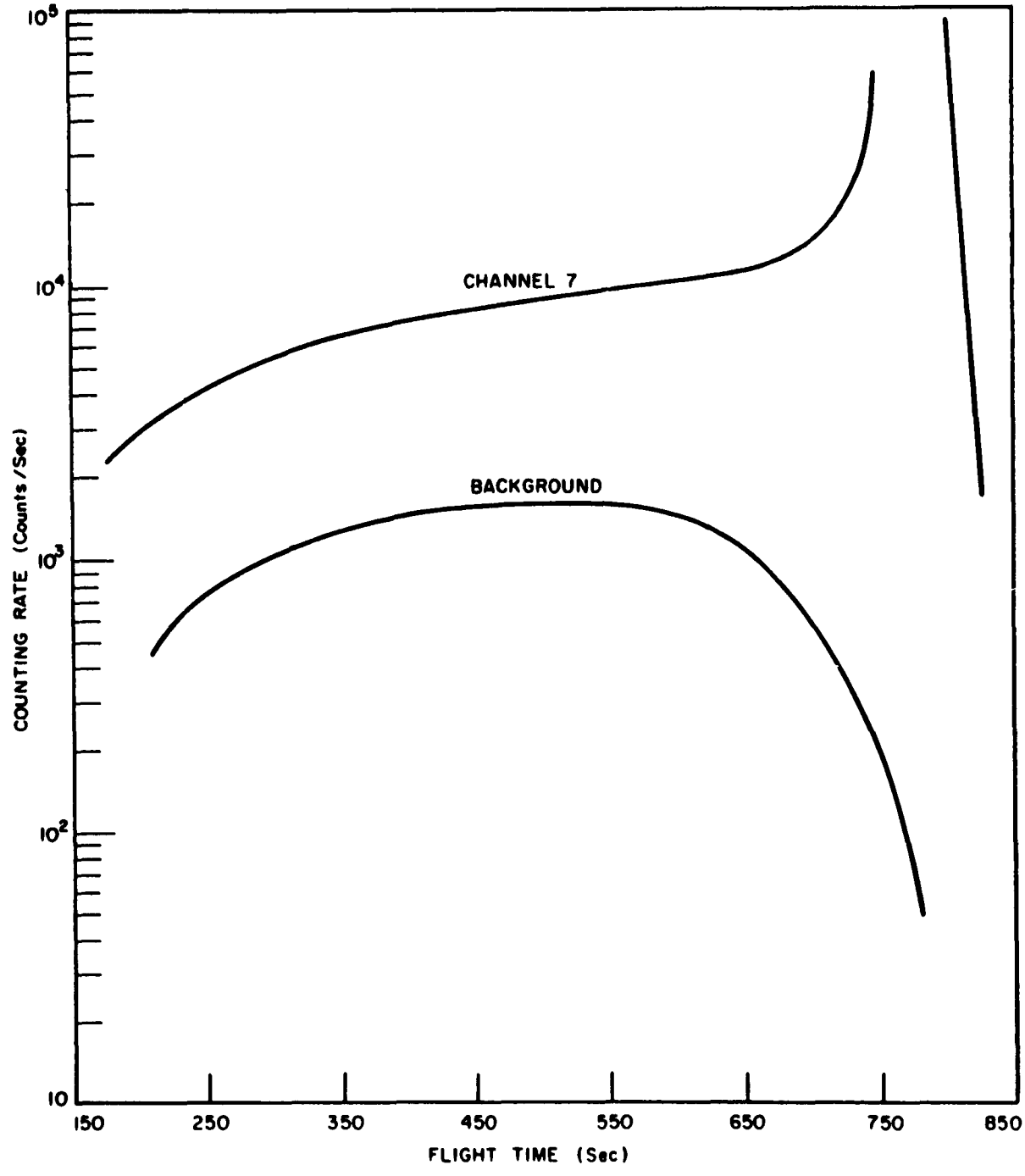

Fig. 4-9 Counting Rate of Detector in Channel 7 on Flight 2019 and Background Correction for This Detector

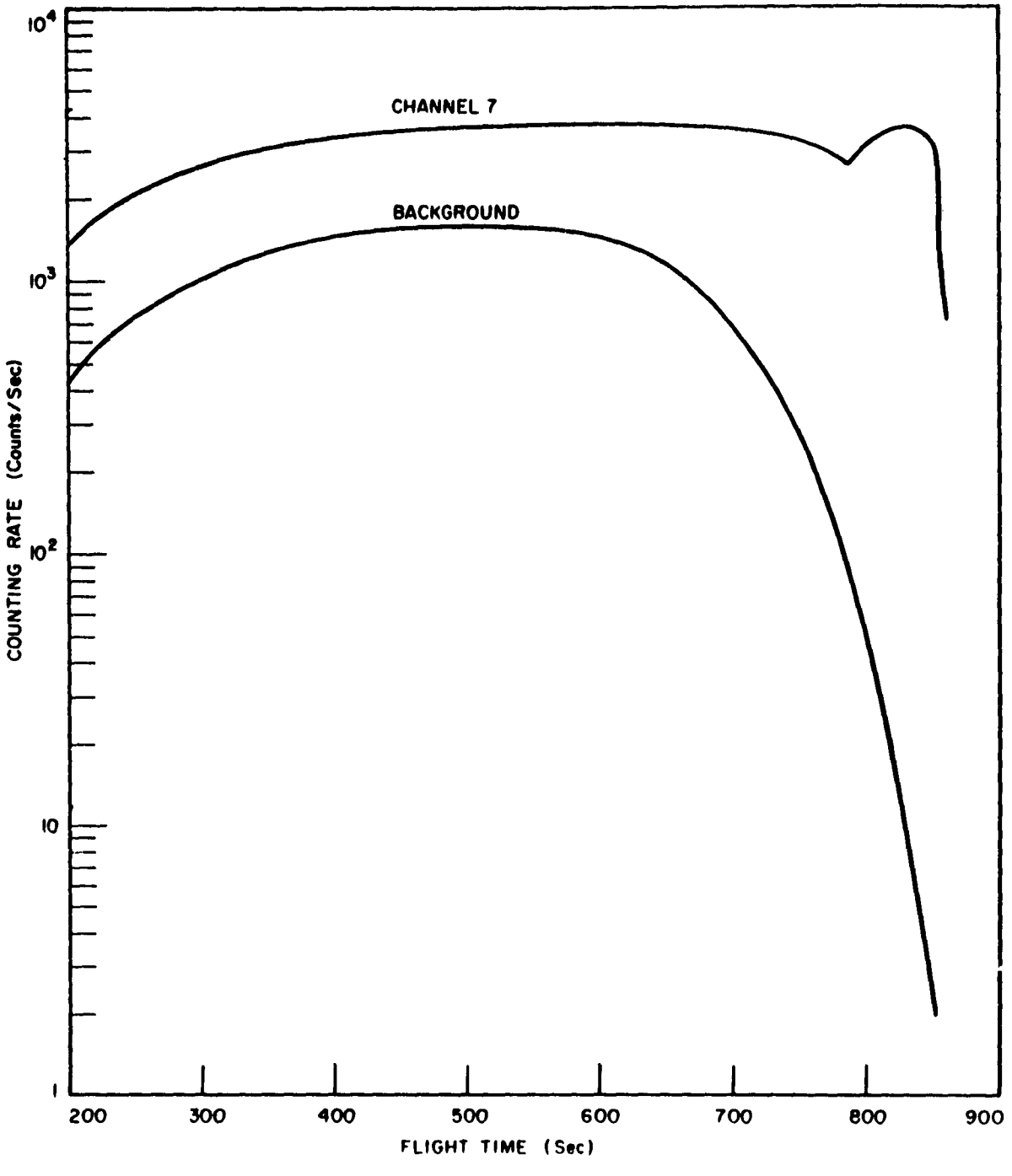

Fig. 4-10 Counting Rate of Detector in Channel 7 on Flight 2021 and Background Correction for This Detector

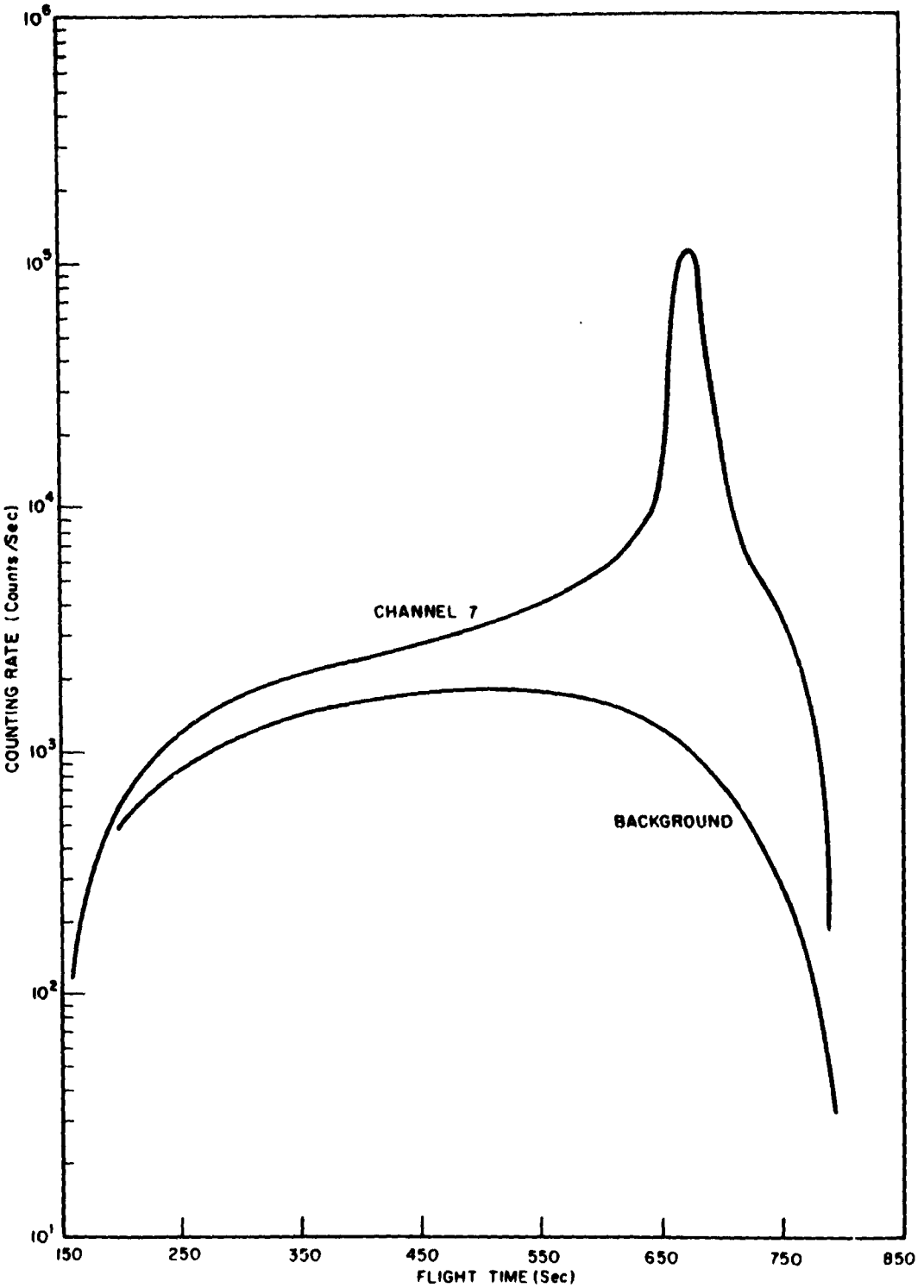

Fig. 4-11 Counting Rate of Detector in Channel 7 on Flight 2024 and Background Correction for This Detector

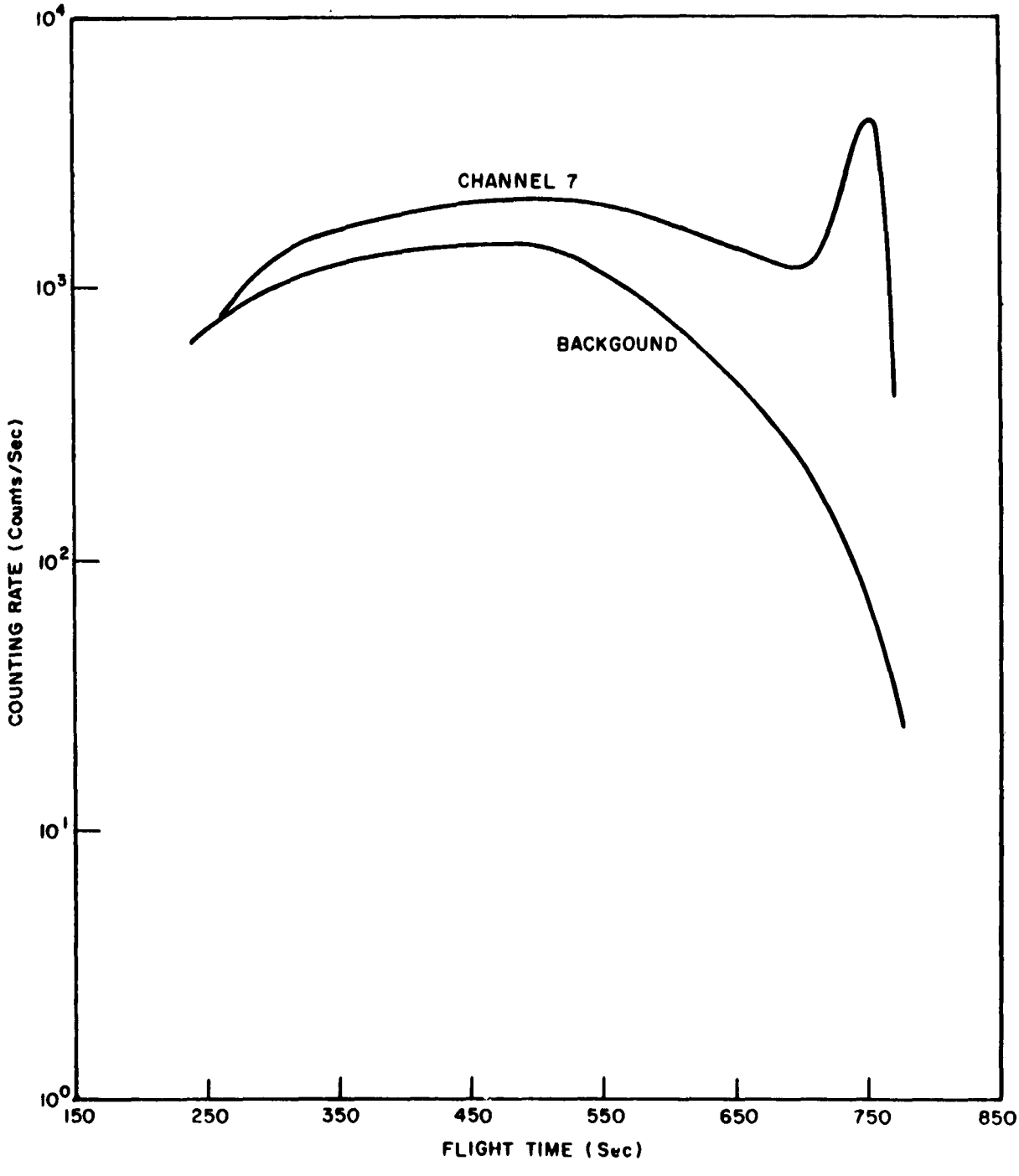

Fig. 4-12 Counting Rate of Detector in Channel 7 on Flight 2027 and Background Correction for This Detector

trajectories of these rockets on a B, log I plot, revealed an abnormally high counting rate for the earliest flight 1822. This high counting rate may have been caused by the presence of electrons injected into the geomagnetic field by the detonation of nuclear devices at high altitudes in the Pacific, as was pointed out in the initial analysis of these data. The decay rate of these electrons was so great, however, that the background due to this cause was considered to be negligible for the later flights now under discussion. (For the few rockets launched from Patrick and Ramey for which the body motions of the rockets were estimated, the counting rates of the small detectors were incorrectly analyzed in the preliminary report because the collimator axes of these detectors never entered the central plane of the radiation.)

4.2.3 COSMIC RAY BACKGROUND

The counting rates produced in the detectors by cosmic rays were evaluated from the counting rates of the tubes which had high threshold energies and in regions of the flights where the bomb and natural radiations were low. Hence, the background counting rate of the long tubes was taken to be the mean counting rate of the Channel 6 detector observed on flight 1822, which was launched prior to a detonation of an Argus device and into the slot between the natural radiation zones. This counting rate was found to be 16 ± 2 counts/sec. It also agreed with the mean counting rate obtained for the Channel 6 counting rate on flight 2027 and with the rate computed by using the omnidirectional geometric function of the detector and a cosmic ray flux of 1.5 cm^2 sec.

The counting rate of the small detectors due to cosmic rays, determined by the method indicated above, also agreed with the background counting rates determined for the same geiger tube types (Anton 222R) used on the Javelin 1 rocket. This counting rate was found to be 2.1 ± 0.25/sec.

4.2.4 BREMSSTRAHLUNG

There was early evidence that the Channel 6 detector was responding to bremsstrahlung in the wing. The counting rate of this detector, above the cosmic ray background, yielded curves when plotted against flight time which

were quite different in shape from those given by the other detectors on the same flight. The Channel 6 curves were more peaked in the wing where the natural radiation was more intense. Moreover, the decay rate of the outputs of the Channel 6 detectors in the wing, obtained by plotting the counting rates of these detectors above cosmic ray background as a function of the launchtime of the rockets after the burst, was found to be much smaller than that given by the detectors in Channels 3 and 7.

A rough calculation was performed to evaluate the response of this Channel 6 detector to the bremsstrahlung of the natural radiation. The detector response was computed for the electron spectrum given by the Javelin I measurements, and the natural radiation level at the position of a particular Jason rocket was estimated by integrating over energy the product of the Javelin I spectrum and the geometric function of the Channel 1 detector. It was found that the ratio of the counting rate of the Channel 6 detector due to this bremsstrahlung to the counting rate of the Channel 1 detector was about 0.001 ± 0.0005. The maximum correction amounted to twice cosmic ray background.

Section 4.3 NET COUNTING RATES OF CHANNEL 7, 3, and 6 DETECTORS

The background correction for Channel 7, obtained as described in Section 4.2.1, and the net counting rates of the detectors in Channels 7, 3, and 6 for flights 2019, 2021, 2024, and 2027 are listed in Table 4-2. For flight 2042, the true counting rate of the Channel 7 detector, which was used to compute background corrections for the other flights, and the net counting rate of the Channel 3 detector are listed in this table.

Only the cosmic ray background counting rate was deduced from the true counting rates of the Channel 3 detectors. The bremsstrahlung correction described in Section 4.2.4, as well as the cosmic ray background correction, were applied to the Channel 6 readings.

TABLE 4-2

Channel 7 Background Corrections and Net Counting Rates for Channels 7, 3, and 6

(R represents counting rate in counts/sec. Subscript, superscript T, and superscript B designate channel number, true counting rate, and background counting rate, respectively.)

Flight 2019

Flight Time (sec)	R_7^T	R_7^B	$R_7^T - R_7^B$	C_3^T	$C_3^T - C_3^B$	C_6^T	$C_6^T - C_6^B$
250	4300 ± 340	740 ± 150	3560 ± 370	2280	± 100	9	± 3
300	5500 ± 550	1020 ± 200	4480 ± 585	3080	± 150	3	± 9
350	6600 ± 300	1260 ± 250	5340 ± 340	3580	± 230	5	± 11
400	7400 ± 1000	1420 ± 280	5980 ± 1040	3980	± 290	6	± 13
450	3200 ± 1300	1540 ± 300	6660 ± 1340	4130	± 320	3	± 14
500	9000 ± 1600	1570 ± 310	7430 ± 1600	4380	± 330	11	± 14
550	9700 ± 1800	1550 ± 310	8150 ± 1800	4380	± 330	14	± 14
600	10200 ± 2100	1420 ± 280	8780 ± 2100	4580	± 350	16	± 16
650	11200 ± 2600	1040 ± 210	10200 ± 2600	4980	± 420	20	± 16
700	14000 ± 4200	580 ± 120	13400 ± 4200	5980	± 600	25	± 16
Band						1230	± 230

TABLE 4-2 (Cont'd)

Flight 2021

Flight Time (sec)	R_7^T	R_7^B	$R_7^T - R_7^B$	$R_3^T - R_3^B$	$R_6^T - R_6^B$
200	1400 ± 140	430 ± 220	970 ± 260	610 ± 60	Statistically Indistinguishable from zero
250	2100 ± 200	730 ± 360	1370 ± 410	980 ± 100	
300	2700 ± 260	1000 ± 500	1700 ± 560	1280 ± 130	
350	3100 ± 300	1260 ± 630	1840 ± 700	1460 ± 150	
400	3300 ± 310	1460 ± 730	1840 ± 790	1570 ± 160	
450	3500 ± 340	1560 ± 780	1940 ± 840	1570 ± 160	
500	3700 ± 360	1600 ± 800	2100 ± 880	1480 ± 150	
550	3700 ± 360	1580 ± 790	2120 ± 880	1380 ± 140	
600	3700 ± 360	1460 ± 730	2240 ± 840	1210 ± 120	
650	3700 ± 360	1170 ± 590	2530 ± 700	1080 ± 110	
700	3600 ± 360	680 ± 340	2920 ± 490	1000 ± 100	
750	3200 ± 310	290 ± 240	2910 ± 430	900 ± 90	
Band	3500 ± 350	Negl.	3500 ± 350	1980 ± 200	

Flight 2024

250	1180 ± 118	830 ± 170	350 ± 210	220 ± 30	Statistically Indistinguishable from zero
300	1680 ± 168	1120 ± 220	560 ± 280	290 ± 30	
350	2050 ± 205	1400 ± 280	750 ± 350	350 ± 30	
400	2350 ± 230	1600 ± 320	750 ± 390	430 ± 30	
450	2750 ± 270	1700 ± 340	1050 ± 440	490 ± 35	
500	3300 ± 330	1750 ± 350	1550 ± 480	560 ± 45	
550	4000 ± 400	1750 ± 880	2250 ± 970	640 ± 64	
600	5000 ± 550	1600 ± 800	3900 ± 970	1300 ± 130	
650	16000 ± 5600	1220 ± 244	14800 ± 5600	8000 ± 1200	
Band				17500 ± 6800	73 ± 29

TABLE 4-2 (Cont'd)

Flight 2027

Flight Time (sec)	R_7^T	R_7^B	$R_7^T - R_7^B$	$R_3^T - R_3^B$	$C_6^T - C_6^B$
300	1200 ± 120	1000 ± 200	200 ± 230	105 ± 15	Statistically Indistinguishable from zero
350	1620 ± 160	1200 ± 240	420 ± 290	116 ± 17	
400	1780 ± 180	1360 ± 270	420 ± 320	125 ± 20	
450	2000 ± 200	1420 ± 280	580 ± 370	127 ± 20	
500	2150 ± 220	1420 ± 280	680 ± 370	145 ± 20	
550	2100 ± 210	1130 ± 230	970 ± 310	165 ± 20	
600	1750 ± 180	750 ± 150	1000 ± 230	185 ± 20	
650	1420 ± 140	450 ± 90	970 ± 170	230 ± 25	
700	1200 ± 120	230 ± 50	970 ± 150	400 ± 40	
Band	4100 ± 410	70 ± 14	4030 ± 420	1880 ± 200	

Flight 2042

Flight Time (sec)	R_7^T	$R_3^T - R_3^B$
250	520 ± 50	15 ± 6
300	830 ± 80	20 ± 6
350	1100 ± 110	23 ± 6
400	1300 ± 130	25 ± 6
450	1500 ± 150	25 ± 6
500	1500 ± 150	22 ± 6
550	1450 ± 140	17 ± 6
600	1300 ± 130	11 ± 6
650	1050 ± 100	7 ± 6
700	730 ± 70	7 ± 7
750	300 ± 30	7 ± 7
Band	100 ± 15	12 ± 8

5. RESULTS AND DISCUSSION

Many limitations of the Jason experiment, some of which were discussed in Sections 4.1 and 4.2, make it difficult to draw definitive conclusions concerning the electron injection and trapping phenomena which occurred following the Argus II detonation. However, the more extensive analysis done in the course of the present contract does allow critical examination of many aspects of the problem. Wherever possible, definite conclusions have been drawn and are presented in this section. However, in many cases the data are insufficient to establish the existence of expected effects. In particular, some of the conclusions reached after the preliminary analysis are not borne out by the present work, after due allowance has been made for experimental uncertainties.

The major difficulty in obtaining a complete picture of the electron trapping phenomena from the Jason flights results directly from the scarcity and sporatic nature of experimental data. The five flights which have been examined in detail passed through the band at different times, at different altitudes, and at different longitudes. Since the electron fluxes are functions of position and time after the burst and since the geomagnetic field is not regular in this region, it is not clear how the data from different flights can best be compared to obtain precise information. A second deficiency of the data results from the restricted dynamic range of the detectors, so that only a few of the counters gave information at the same time. In most cases where the small counters had sufficient counting rates for statistical accuracy, the large counters were counting so rapidly that the telemetering tracings could not be read or the uncertainties in the dead time corrections were excessive. This difficulty severely limits a comparison of the energy spectrum obtained during various flights, and lowers the precision with which changes in the spectrum can be detected. A final serious deficiency was in the background counting rate information. This point has been discussed in Section 4.2. However, it should be noted here that during most of the time when the rockets were not in the intense portion of the radiation band, background uncertainties constituted the largest source of error.

5.1 GENERAL RESULTS

The results of the analysis are summarized in Figures 4-1 through 4-5, which give the counting rates as a function of time after launch of flights 2019, 2021, 2024, 2027 and 2042. In addition to the localized region of high intensity radiation which appears at the far right-hand side of the figures, there is a broad region at higher latitudes where the radiation is significantly above the background levels. This feature is most pronounced for Channels 3 and 6, but is also apparent for Channel 7. Because of the large background of low energy Van Allen electrons, the enhanced radiation in this wing is not as apparent for the low energy channels. The difference in the magnitude of the flux in the intense band for the various flights is due primarily to the decay with time of the shell of trapped electrons, although this effect is modified considerably by the differences in the altitudes at which the various vehicles passed through the band. For example, flight 2024 which passed through the band at an altitude of 400 km showed a more pronounced peak in counting rate than did flight 2021, which actually took place earlier, but crossed the band at an altitude of only about 100 km. These altitudes refer to the heights of the conjugate points of the rocket positions.

5.2 VARIATION OF ELECTRON ENERGY SPECTRUM WITH POSITION

The ratios of the counting rates of the detectors were examined at various times during each flight to see if the spectrum of the injected electrons was different at different points of the trajectory. In particular, it was of interest to see if the spectrum in the wing differed from that of the intense band, since this would shed light on whether the wing electrons were injected directly into their orbits or whether they diffused across field lines. From the discussion of the background problem in Section 4.2, it is apparent that only the counting-rate ratios R_7/R_3 and R_3/R_6 can be considered reliable for this purpose. These ratios for flights 2019 and 2024 are listed in Table 5-1. In the center of the band, both detectors in Channels 7 and 3 on flight 2019 were saturated. The value listed in parenthesis for this flight in the R_7/R_3 column is the R_3/R_4 ratio which was measured in the center of the band. The

listing in parenthesis in the R_3/R_6 column was obtained by integrating the product of the geometric function of the Channel 3 detector and the best fit spectrum over energy and dividing the result by the measured rate R_6. The ratios in the table appear to be changing systematically with time, with the R_7/R_3 indicating a softening of the spectrum and the R_3/R_6 ratio indicating a hardening of the spectrum. It is not believed that these ratios demonstrate a spectrum change. It is more likely that the trend reflects a systematic error in the evaluation of the background.

TABLE 5-1

Comparison of Counting-Rate Ratios

Flight Time (sec)	$(R_7^T - R_7^B)/(R_3^T - R_3^B)$ Flight 2019	$(R_7^T - R_7^B)/(R_3^T - R_3^B)$ Flight 2024	$(R_3^T - R_3^B)/(R_6^T - R_6^B)$ Flight 2019	$(R_3^T - R_3^B)/(R_6^T - R_6^B)$ Flight 2024
250	1.56 ± .26	1.60 ± .80		
300	1.46 ± .28	1.81 ± .74		
350	1.50 ± .33	1.86 ± .86	720 ± 1600	
400	1.50 ± .35	1.75 ± .82	660 ± 1430	
450	1.60 ± .40	2.14 ± .82	520 ± 900	
500	1.70 ± .45	2.77 ± .86	390 ± 500	
550	1.86 ± .49	3.50 ± 1.50	310 ± 310	
600	1.92 ± .53	3.00 ± .80	290 ± 290	
650	2.04 ± .57	1.85 ± .71	250 ± 200	
700	2.25 ± .72		240 ± 150	
Band	(1.90 ± .47)*		(416 ± 136)*	245 ± 132

*Refer to text for comments on this ratio.

5.3 VARIATION OF ELECTRON ENERGY SPECTRUM WITH TIME

The reduced data were also examined carefully to see if there was an indication of a change in the electron energy distribution during the 88-hour period covered by the Jason experiment. Since no definitie variation of spectrum with position had been detected, it was felt possible to compare data taken on different flights without regard to the position of the vehicle during the time the comparison was made. In this way sections of various flights could be compared in which the counting rates were similar and dead-time corrections would be comparable. This investigation failed to show any definite time variation in the spectral distribution, in agreement with the preliminary analysis presented two years ago. Unfortunately, the low energy channels where the spectrum change is expected to be most pronounced were not very useful in this regard because of the high and uncertain background produced by the Van Allen electrons. The fact that the spectrum obtained during flight 2019 which took place about half an hour after the explosion was not significantly different from the later flights is perhaps an indication of the poor sensitivity of the spectrum test.

5.4 DECAY OF ELECTRON FLUX

A quantitative measurement of the decay of geomagnetically trapped electrons was one of the most important objectives of the Argus experiment. The observed decay time of several days is considerably less than the decay time of many years which has been calculated for particles distributed in the Van Allen electron belt. The relative short time of decay has been attributed to the low injection altitude and to the low altitude at which the measurements were made. It has been argued that what is observed is the decay of a higher order normal mode in the spatial distribution of electrons in the trapping volume; hence the lifetime is correspondingly reduced. Theoretical calculations have suggested that the intensity of this distribution may decrease as the inverse first power of the time after detonation, a time variation which is in fair agreement with observation. However, it has also been observed that the beta decay of gross fission fragments behaves as $t^{-1.2}$. Since the

interpretation which would be placed on the Argus experiment is vastly different depending on which time behavior is obtained, a considerable effort was made to resolve this question from the results of the Jason rockets.

Because of the different trajectories followed by the various flights and because no method of unquestioned validity was found to extrapolate the measurement from one position to another, it was not possible to compare intensities found at different times near the center of the band. However, in the broad region of radiation north of the band, it is possible to make a much more accurate estimate of the decay rate. From the curves of Figure 4-8 which give a plot of the vehicle trajectories on B, Log I coordinates, it can be seen that there are seven points where two of the trajectories intersect. At these points the rockets of the two flights pass through equivalent points on the magnetic shell and a comparison of the counting rates of the two flights will then give an estimate of the flux decay during the time interval between the two flights. A small correction was made for the difference in the longitudes of the two vehicles at the time of the intersection. This correction is, in essence, the variation of flux along a line of constant B and Log I. It was obtained from flight 2025 launched from Cape Canaveral. This flight was directed towards the east, and the ascending and descending portions of the trajectory passed through equivalent magnetic locations, which were displaced in longitude and also in altitude. Hence, this flight gives the rate at which the flux varies during the eastward drift. Corrections for this effect are fairly small, ranging from 0 to 7 percent because of the high altitude at which most of the intersections occurred.

Since each intersection gives a value of the decay during a particular time interval, the seven intersections give seven points on a time decay curve. These points, obtained for the Channel 3 detector are shown in Figure 5-1. Here, the ratio of the counting rates observed by the two rockets at each intersection point is plotted against the ratio of the times at which the rockets reached the point of intersection after the time of burst. The error bars indicate the total probable error which results from counting statistics,

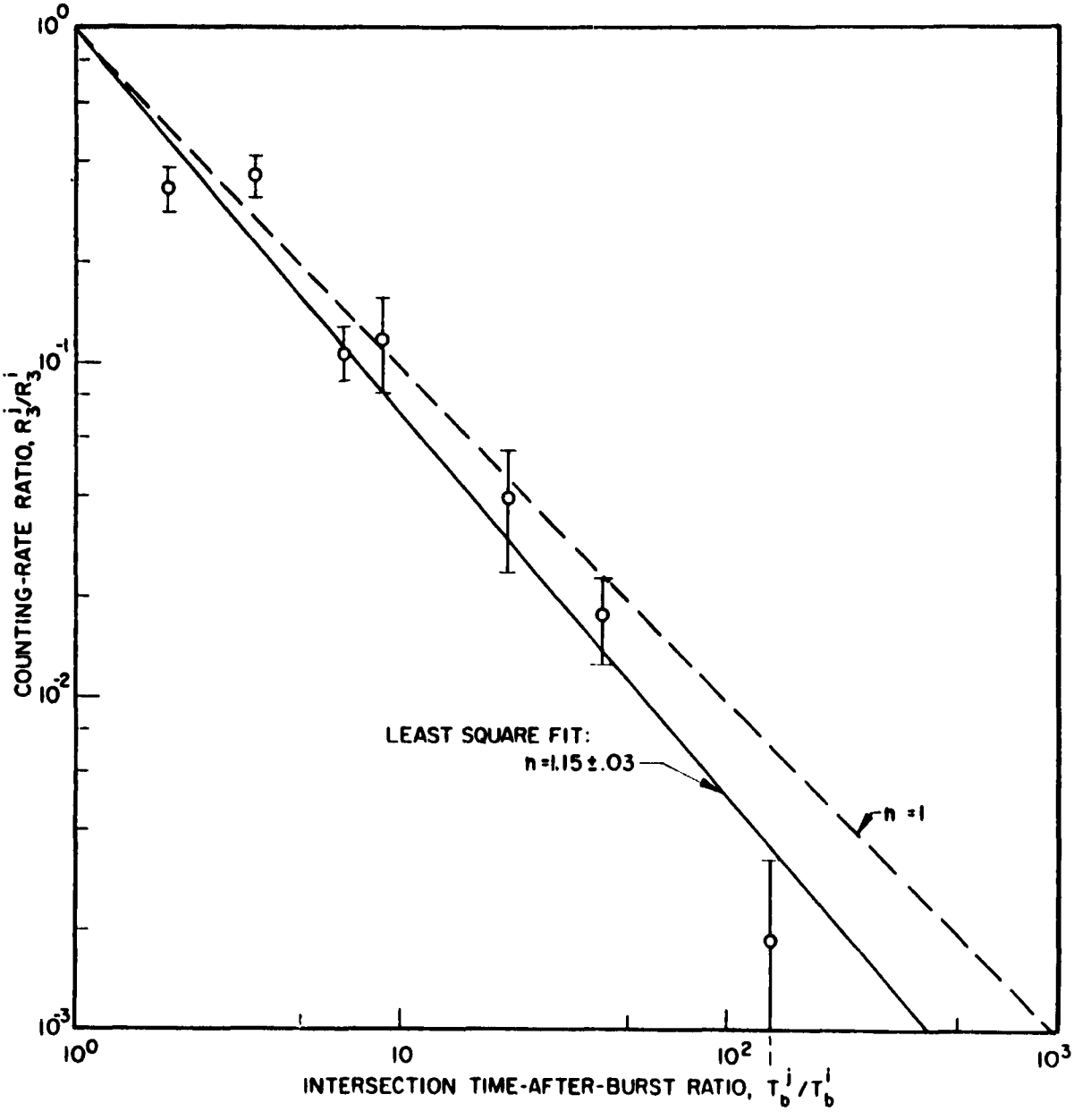

Fig. 5-1 Time Rate of Decay of Electron Flux. For a Decay Rate of the Form t^{-n}, n Has the Value 1.15 ± 0.03

dead-time uncertainties, background uncertainties, and trajectory uncertainties. Assuming that the decay has a function form of t^{-n}, a least square fit to the data gives a value of n of 1.15 $\pm$ .03. Since the ratio of the counting rates must be equal to 1 when the time ratio equals 1, only a one parameter fit (the slope of the line) was required. The same calculation for channel 7 gives similar results but with considerably greater probable errors.

On the basis of this analysis, it appears more likely that the time dependence follows that of gross fission product decay, rather than the predicted t^{-1}. The line of slope n = 1 is drawn in Figure 4-13 for comparison.

5.5 ENERGY SPECTRUM OF ELECTRONS

Since no variation in time or space was noted in the energy distribution of the electrons in the band, the determination of the electron spectrum was made at positions where the experimental data were most reliable. The best information for this purpose was obtained in flight 2019 during its passage through the band, at which time reliable data were obtained simultaneously with detectors 2, 4, 6 and 8. The spectrum was represented by the expression

$$f(E) = AE^{D} \exp(-BE)$$

where E is the electron energy in Mev and A, B, and D are parameters. Since A merely normalizes the flux, the shape parameters D and B are of greatest concern.

To deduce the electron spectrum, a set of values of B and D were selected and the counting rates calculated from the equation,

$$R_i = \int G_i(E)\, f\,(E)\; dE$$

where $G_i(E)$ is the geometric factor of the "i"th detector as obtained by the calibration measurements described in Section 3. The calculated counting rates were then compared to the experimental values by forming the sum of the squares

of the deviations

$$M(B,D) = \sum_i W_i (R_i - R_i^{ex})^2$$

where W_i is a weighting function equal to the reciprocal of the square of the probable error in the counting rates, and R_i^{ex} is the experimental counting rate of the "i"th detector. The values of M form a matrix in B, D space and the minimum value of M as a function of B and D indicates the values of B and D which best represent the experimental result. This computing process was carried out using a digital computer. The resulting spectrum was modified by interation to improve the agreement with the counting rates. The best fit spectrum is depicted by the solid line in Figure 5-2. An indication of the accuracy of the spectrum is given by the rectangles shown in the figure. These rectangles are the "raw-data" defined as follows: the vertical lines of the rectangles are drawn at the energy values which are at the half-height points of the product of the best fit spectrum and the geometric functions of the detectors. The vertical positions of the centers of the rectangles are located at the geometric-function weighted averages of the flux in these energy intervals; and the heights of the rectangles correspond to twice the probable errors of the net counting rates of the detectors.

Two other spectra are shown in Figure 5-2 for comparison: An unmodified fission spectrum and a fission spectrum divided by the product $\omega_d T_b$, the azimuthal drift velocity times the bounce period between mirror points. The disagreement of the best fit spectrum with the fission spectrum is not severe; it is now much more in agreement with the data than was indicated by the initial analysis of the data. However, the better agreement of the data with the fission spectrum divided by $\omega_d T_b$ might be evidence of a fission spectrum source, a lifetime of less than a drift period for the electrons which reach the region of the Jason rockets, and no evidence of energy degradation by scattering.

This statement can be verified as follows: the omnidirectional flux given by the Jason rockets is equal to the number density of the electrons times

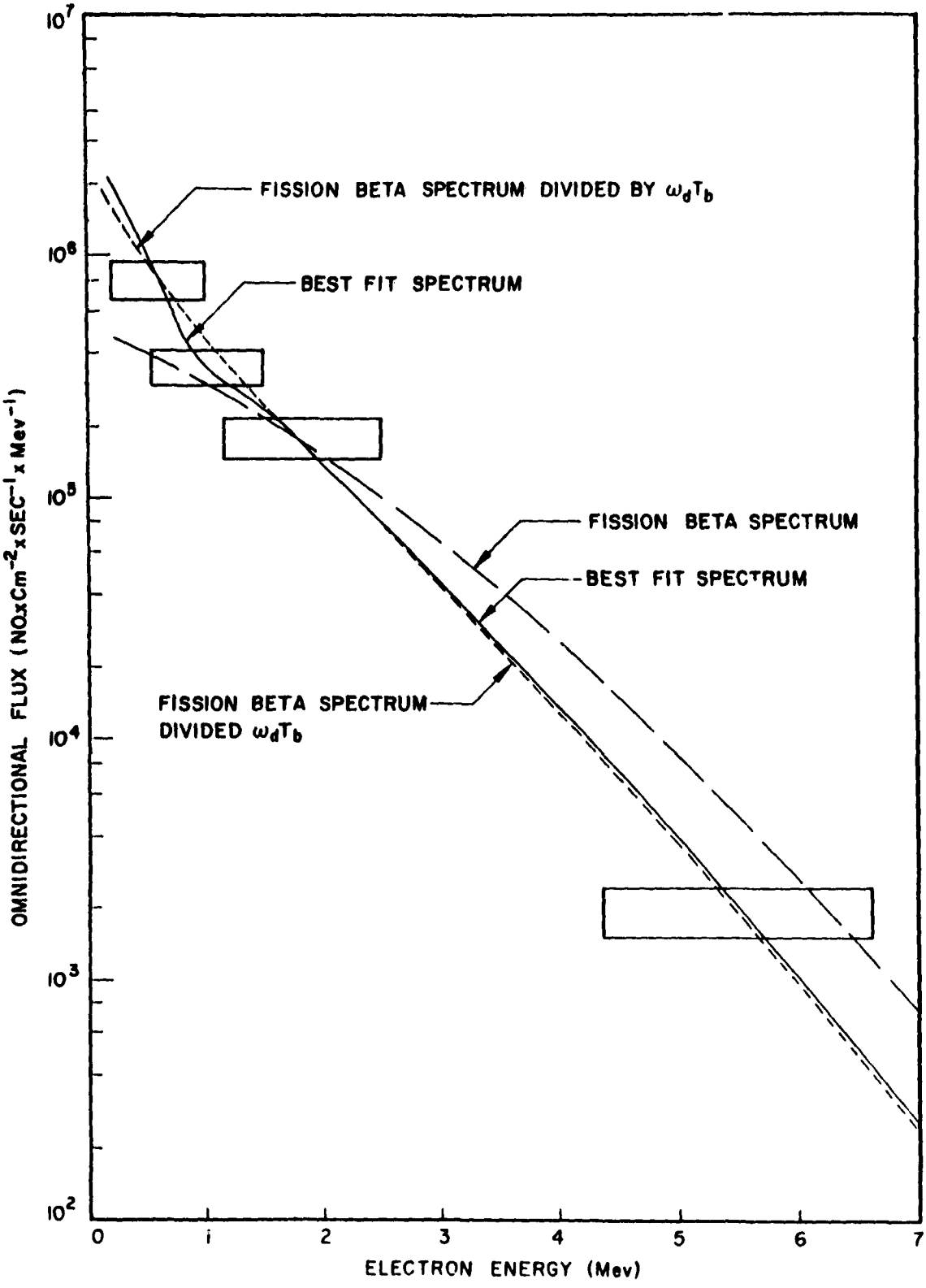

Fig. 5-2 Omnidirectional Flux at Center of Electron Shell

their velocity. Or,

$$f(E)dE = n(E)dE \cdot v, \qquad (5\text{-}1)$$

where n(E) is the number density of electrons of energy E per unit energy interval. If N(E) designates the number of electrons emitted by the fission spectrum per unit time and unit energy interval and dV is the incremental volume the electrons fill during the incremental emission time dt, then

$$f(E)dE = \frac{N(E)\, dE\, dt}{dV} \cdot v \qquad (5\text{-}2)$$

This equation shows that a fission spectrum multiplied by electron velocity will be measured if there is no electron loss and if the electrons are injected into a magnetic shell of fixed volume for a period of time which is long in comparison to drift periods. However, if the electrons which were reflected in the region of the Jason rockets become lost beyond the longitude of the measurements, then for these electrons dV/dt is proportional to ω_d, and v is inversely proportional to T_b. Hence, with no loss of energy by scattering, the measurements should yield a fission spectrum divided by $\omega_d T_b$.

The observed counting rates R_i of the detectors in the center of the band on flight 2042 and the rates R_i^F given by the product of the modified-fission beta spectrum $(N(E)/\omega_d T_b)$ and the geometric functions of the detectors integrated over energy are listed below for comparison.

Channel Number	2	8	4	6
R_i	4030 ± 760	2000 ± 360	1050 ± 190	1280 ± 230
R_i^F	4030	2730	1000	1250

For flight 2019, which was launched about 23 minutes after the burst, the good agreement of the measurements with this spectrum, is exceedingly difficult to understand. The mechanism proposed earlier involved the passage of fission

fragments from the detonation point to the conjugate region via the magnetic field lines, and electrons which were emitted during the time the fission fragments were in transit would be trapped. If this process did occur, the injection would take place only during the fragment passage and the spectrum observed during flight 2019 would consist of a line spectrum containing contributions of particles whose energies were appropriate for drift around the world one or more times during the interval between the detonation time and the measurement. Comparison of the counting rates (R_i^L) expected with this spectrum with the observed rates R_i, as shown in Table 5-2, reveals that the agreement is poor.

An alternate hypothesis for injection would be to assume that the fragments become distributed in such a manner that injection can take place for a much longer period of time. If this were the case, the spectrum observed in flight 2019 would be continuous, containing components for very high energies but being cut-off at energies below about 0.8 Mev, since electrons below this energy cannot drift the required distance in the available time. The observed counting rates (R_i) and the rates (R_i^C) calculated with these assumptions are also listed for comparison in Table 5-2. In this case, the high threshold energy detector in Channel 6 reads quite low because of the $t^{-1.2}$ decay of the source (these high-energy electrons were emitted at a later time than the low-energy electrons to have arrived at the rocket position at the same time).

It should be noted that the above calculations assume that no energy is lost by the electrons during their drift about the earth. It is unlikely that the electrons do not loose energy since a considerable amount of scattering must occur if the electrons are to be found in orbits which are accessible to the Jason rockets. Due to the anamolies in the geomagnetic field, electrons whose mirroring points are above the earth's surface on the magnetic line passing through the detonation point will, after drifting to the latitude of the Jason flights, mirror at altitudes far above apogee of the vehicles. Therefore, in order to be detected these electrons must have been scattered into lower altitude orbits, and their energy must be correspondingly modified. The amount of energy loss expected cannot be calculated under the present state of the trapping theory and the uncertainty introduced by the possibility of energy

loss makes the conclusions derived from spectrum information extremely tentative.

TABLE 5-2

Comparison of Counting-Rate Ratios Based on the Various Injection Mechanisms for Flight 2019

CHANNEL NUMBER(i)	2	8	4	6
Observed Ratios (R_1/R_2)	1.00 $\pm$ .27	0.50 $\pm$ .13	0.26 $\pm$ .07	0.32 $\pm$ .09
Modified Fission Beta Spectrum (R_1^F/R_2^F)	1.00	0.68	0.25	0.31
Line Spectrum (R_1^L/R_2^L) (instantaneous injection)	1.00	0.88	0.18	0.19
Continuous Emission (R_1^C/R_2^C) (Cut-off below .8 MeV because of drift line requirements)	1.00	0.90	0.22	0.042

5.6 INJECTION EFFICIENCY

A lower limit of the trapping efficiency can be determined by considering the Jason data to be a measure of the rate at which electrons are lost. This is plausible because of the special region in which the data were taken with respect to the total configuration of the geomagnetic field. As discussed earlier, electrons which reached the region of the Jason flights were very likely absorbed by the atmosphere as they proceeded to drift eastwards. Hence, an integration of the flux measurements over time gives a lower limit of the total loss of trapped electrons, from which a lower limit of the trapping efficiency can be estimated.

The incremental loss rate of electrons, observed by the Jason rockets, can be obtained by finding the number of electrons in an incremental magnetic shell which cross a certain area at the equator per unit time and which have pitch angles at the equator such that the electrons reach the altitudes of the Jason rockets. By Liouville's theorem, we know that the electron flux at the equator, directed at the angle α_o with respect to the geomagnetic line of force, is equal to the flux at the Jason-rocket altitudes which is directed essentially at 90° to the magnetic field line. The angle α_o can be obtained from the adiabatic invariance of the magnetic moment of the electrons ($\sin^2 \alpha_o$ equals ratio of magnetic field intensity at equator to magnetic field intensity at Jason altitude along the same magnetic line of force). Thus, the number of electrons of energy E in the range ΔE which cross a unit cross sectional area of the incremental magnetic shell at the equator at the time t is $f(E,t)\,\Delta E/\cos\alpha_o$, where $f(E,t)$ is the measured flux.

To get the number of electrons which are lost per second from the shell, the flux $f(E,t)\,\Delta E/\cos\alpha_o$ must be multiplied by the cross sectional area $r_o\ \Delta r_o\ \Delta\phi(E)$ of the magnetic shell. Here r_o is the geocentric distance to the line of force at the magnetic equator, Δr_o is the thickness of the shell, and $\Delta\phi(E) = \omega_d\, T_b/2$. Note that if the azimuthal extent $\Delta\phi$ of this "loss area" were taken to be larger than $\omega_d\, T_b/2$, then electrons would be "counted" more than once; if $\Delta\phi$ were taken to be smaller than $\omega_d\, T_b/2$, then some of these electrons could avoid striking the "loss area" if their

phases were appropriate. Hence, the loss of electrons of energy E in the range ΔE, contained in the shell at r_o of thickness Δr_o per second is

$$L(E, r_o, t)\ \Delta E\ \Delta r_o = \frac{f(E,t)\ \Delta E}{\cos \alpha_o} \cdot r_o\ \Delta r_o\ \Delta \phi(E) \qquad (5\text{-}3)$$

In the previous section it was shown that the measured spectrum agreed exceedingly well with a fission spectrum divided by $\omega_d T_b$. Consequently, since the measured spectrum in Equation (5-3) is multiplied by $\Delta \phi(E) = \omega_d T_b/2$, the loss spectrum L(E) is just the fission spectrum.

An evaluation of L(E) in the center of the band at t = 41 minutes (2019 data) and a subsequent integration over energy yields the following loss rate of electrons from the band:

$$\dot{N}_B(41 \text{ min.}) = \int_{.5 \text{ Mev}}^{10 \text{ Mev}} L(E),\ 2r_e,\ 41)\ (.047\ r_e)\ dE$$

$$= 9.44 \times 10^{18} \text{ electrons/sec.}$$

A similar evaluation and integration of Equation (5-3) over the "north wing" of the trapping region yields,

$$\dot{N}_{NW}\ (32 \leq t \leq 40.7 \text{ min}) = 4.23 \times 10^{18} \text{ electrons/sec.}$$

Now, by assuming that the loss rate from the low latitude wing is equal to that from the high latitude wing and extrapolating the time decay of the flux ($t^{-1.15}$) which was observed in the range 32 min $\leq$ t $\leq$ 5333 min, to, say, t = 1 min, the total loss of electrons after t = 1 min, becomes,

$$N_o \approx \int_1^{\infty} \left[\dot{N}_B(41) + 2\dot{N}_{NW}(41)\right]\left(\frac{t}{41}\right)^{-1.15} dt, \text{ or}$$

$$N_o \approx 6.2 \times 10^{21} \text{ electrons.}$$

Finally by taking the total number of fission betas emitted one minute or later after the detonation to be

$$N_T = (1.7\ \text{KT})\ (1.3 \times 10^{23}\ \frac{\text{fission frag.}}{\text{KT}})\ (2.1\ \text{electrons/fission emitted after one minute})$$

$$= 4.65 \times 10^{23}\ \text{electrons},$$

the lower limit of the trapping efficiency is,

$$(\text{Trap. Eff.})_{\text{lower limit}} = 6.2 \times 10^{21}/4.65 \times 10^{23} = 1.3 \times 10^{-2}\ .$$

This value is believed to be a lower limit because it is quite likely that more electrons were lost than those detected by the Jason rockets. Also, this trapping efficiency is on the low side because no account was taken of electrons which might have been trapped for very long periods of time, that is, of electrons with mirror points so high as to remain trapped during the course of this experiment.

5.7 COMMENTS ON RESULTS

The observed decay rate of the electron flux, the constancy of electron spectrum with time and space, and the broad wing of electron flux extending hundreds of milometers north of the intense central band, suggest that the phenomena leading to electron injection and decay may be vastly different from the high altitude injection by trapped fission fragments proposed earlier. The broad wing to the north of the band is possibly produced by the decay of fission fragments which were either initially uionized or which became uncharged by charge exchange collisions with the atmospheric atoms. The uncharged fragments could move freely across magnetic field lines. The existence of this wing only 41 minutes after the detonation and the constancy of spectrum as a function of latitude suggest that electrons could not have diffused to this region by scattering with the atmosphere. An alternate explanation might be that the wing electrons were injected by debris carried aloft in the rising fireball. However, in order to place electrons in the observed positions, the debris would have to rise vertically almost 1000 km. Since debris rise could produce a wing only on the high latitude side of the central band, the occurrence of a similar wing on the low latitude side would indicate that debris rise was not the cause of the wing. The data obtained with the satellite Explorer IV should be examined closely for evidence of such low-latitude wing.

The time variation of the electron flux is not understood, and the theory of electrons trapped in the geomagnetic field is not adequate at present to give quantitative values of the flux variation with time. Early attempts to estimate time decay rates led, with certain extreme approximations, to a time dependence given by 1/t. Another approach leads to the conclusion that the decay time is not a simple function of time but depends upon both the initial energy distribution and pitch angle distribution of the electrons. In essence, the distribution function of the electrons can be decomposed into a series of spatial eigenfunctions, each of which decay in a prescribed manner. Only in the simple case when a single eigenfunction is present will the decay rate be the same at all altitudes. However, when the initial transients have died out and the flux does decay with the time constant appropriate to the longest lived or dominant eigenfunction, the decay time expected is on the order of tens of years, far longer than the experimental results indicate.

However, the interpretation of the Jason experiment in terms of this theory is difficult due primarily to the departure of the geomagnetic field from that of a centered dipole. As mentioned previously, the trajectories of the Jason rockets lie in the "magnetic shadow" of the earth. In effect, this means either that the fission fragments emitting the electrons must have migrated thousands of miles in longitude or that the electrons seen by the Jason vehicles must have been scattered sufficiently to lower their mirror points hundreds of kilometers during a single drift period about the earth. No quantitative calculations of the time required for mirror point diffusion are available to check this latter possibility, although qualitative arguments indicate that it is possible providing the initial injection altitude is low enough.

The observed decay rate in the wings is sufficiently close to the time variation of the gross beta activity of fission fragments that one is tempted to explain the observed decay by assuming that the flux is in some form of equilibrium with the source and that the observed time dependence results from the decaying activity of the fission debris rather than from the lifetime of individual electrons. This situation would occur if the fragments remained

in a position where they could inject electrons and the electron mirror points were sufficiently low that most of the electrons are lost after one drift period about the earth.

In addition to explaining the time dependence of the electron flux, such an injection phenomenon would also account for the constant spectrum over the time period of the observation. However, the spectrum observed on flight 2019 shortly after the detonation is still difficult to explain on this basis.

This continuous injection hypothesis has two fundamental difficulties. The first difficulty is the low injection efficiency which would probably occur if the electrons were emitted at low altitudes. The altitude of the bomb detonation makes it very unlikely that any of the fission fragments can be magnetically trapped high above the atmosphere, and it is expected that they will quickly loose energy and come to thermal equilibrium with the atmosphere somewhere between 100 km and perhaps 500 km depending on initial pitch angles. Since the initial mirroring point of an electron cannot be higher than the injection point, many of these electrons will not live long enough to drift once around the earth. Some of the electrons will have their mirror points raised by scattering, but until quantitative calculations are available, it is difficult to estimate how effective this scattering might be.

The other major difficulty is the requirement that the fission debris be stationary, at least in latitude, for a duration of several days. Although data are meager, wind velocities above one hundred kilometers are expected to be several hundred kilometers per hour, a velocity which would quickly disperse the radioactive fragments if they were neutral and behaved as the neutral constituents of the ionosphere. If the fragments are charged, they might be held in place by the magnetic field, at least at altitudes above the exosphere where collisions with the neutral particles are infrequent. Actually, a continual change in the degree of ionization of the fission fragments is expected: During the slowing-down process, a tendency towards neutralization by charge exchange collisions prevails; but after thermal equilibrium with the atmospheric constituents is reached, fission fragments can be charged by ionizing collisions and by the action of the solar ultraviolet. In fact, the fractional ionization

of the fission fragments would probably be greater than that of the atmospheric gases because of the lower ionization potentials of the fragment atoms compared to the ionization potentials of oxygen and nitrogen.

At the present time, work is continuing on these two aspects of the Argus experiment: 1) the ultimate distribution of the fission fragments, and 2) the efficiency of low altitude injection as modified by atmospheric scattering. Equations describing the time behavior of the distribution function of electrons trapped in the geomagnetic field have been derived and are now being programmed for solution by a digital computer. The results of this calculation should at least give a qualitative indication whether fragments suspended at a few-hundred kilometers altitude can inject enough trapped electrons to agree with the measured fluxes. With regard to the possible suspension of fission fragments at high altitude, it is hoped that forthcoming geophysical data may shed some light on this question. Preliminary reports have indicated that a high concentration of ionized atoms of meteoretic material have been detected at high altitude, suggesting that heavy ions may remain charged and suspended for long periods of time. Further evidence may be obtained from studies of sodium ions detected in studies of the night airglow. It is hoped that as a result of this further work it will be possible to conclude whether the short-time injection mechanism or the continuous injection hypothesis best describes the trapping phenomena observed in the Argus experiment.

TABLE A-1

GEOMETRIC FUNCTIONS of DETECTOR CHANNELS
(Subscript Refers to Channel No.)

Electron Energy (MEV)	G_1	G_7	G_3	G_6	G_2	G_8	G_4
.150	0	0	0	0	0	0	0
.200	0				.00100		
.250	.0652				.00232		
.300	.151				.00280		
.350	.212				.00308		
.400	.275				.00326		
.450	.330				.00341	.00045	
.500	.374	.05			.00354	.00104	
.550	.405	.17			.00366	.00174	
.600	.434	.35			.00375	.00226	
.650	.455	.57			.00384	.00264	
.700	.474	.82			.00391	.00298	
.750	.489	1.07			.00397	.00324	
.800	.501	1.31			.00403	.00344	
.850	.513	1.55			.00408	.00361	
.900	.523	1.76			.00412	.00374	
.950	.531	1.94	.01		.00416	.00383	.00006
1.000	.536	2.10	.05		.00420	.00391	.00022
1.050	.543	2.24	.09		.00423	.00398	.00038
1.100	.547	2.36	.16		.00426	.00404	.00055
1.150	.554	2.47	.25		.00429	.00409	.00074
1.200	.559	2.58	.34		.00432	.00413	.00092
1.250	.562	2.68	.45		.00434	.00418	.00113
1.300	.566	2.76	.57		.00437	.00421	.00133
1.350	.571	2.84	.70		.00439	.00424	.00154
1.400	.575	2.92	.82		.00441	.00428	.00174
1.450	.578	2.98	.94		.00443	.00430	.00195
1.500	.581	3.04	1.05		.00444	.00433	.00213
1.550	.585	3.08	1.17		.00446	.00436	.00234
1.600	.587	3.13	1.29		.00447	.00438	.00252
1.650	.590	3.17	1.40		.00448	.00440	.00269
1.700	.593	3.21	1.51		.00449	.00442	.00284
1.750	.595	3.24	1.60		.00450	.00444	.00298
1.800	.598	3.27	1.69		.00451	.00446	.00312
1.850	.600	3.30	1.77		.00452	.00447	.00325
1.900	.601	3.32	1.85		.00452	.00448	.00336
1.950	.603	3.34	1.92		.00453	.00449	.00345
2.000	.605	3.36	1.98		.00453	.00450	.00353

TABLE A-1 (cont'd)

GEOMETRIC FUNCTIONS of DETECTOR CHANNELS
(Subscript Refers to Channel No.)

Electron Energy (MEV)	G_1	G_7	G_3	G_6	G_2	G_8	G_4
2.250	.612	3.42	2.21	0	.00455	.00453	.00377
2.500	.619	3.45	2.39		.00457	.00456	.00389
2.750	.624	3.47	2.54		.00458	.00457	.00396
3.000	.626	3.48	2.67		.00458	.00458	.00403
3.250	.629	3.49	2.79				.00410
3.500	.631	3.49	2.89				.00415
3.750	.634	3.50	2.98				.00420
4.000	.634	3.50	3.06				.00425
4.250	.635	3.50	3.12				.00429
4.500		3.51	3.17	.020			.00433
4.750		3.51	3.21	.068			.00437
5.000		3.51	3.25	.110			.00440
5.250		3.51	3.28	.150			.00443
5.500		3.51	3.31	.198			.00445
5.750		3.52	3.34	.250			.00447
6.000			3.36	.310			.00449
6.250			3.38	.370			.00451
6.500			3.40	.440			.00452
6.750			3.42	.510			.00453
7.000			3.43	.580			.00454
7.250			3.44	.650			.00455
7.500			3.45	.720			.00456
7.750			3.46	.793			.00457
8.000			3.47	.862			.00457
8.250			3.48	.933			.00458
8.500			3.48	1.008			.00458
8.750			3.48	1.078			.00458
9.000			3.49	1.149			.00458

TABLE A-2

COUNTING RATES OF DETECTORS ON FLIGHT 2019

Flight Time Interval (sec) From	To	Average of Channels 1 & 5	Channel 7	Channel 3	Channel 6	Channel 2	Channel 8	Channel 4
177	184	3850 ± 147	2300 ± 160	1010 ± 100	10 ± 10	307 ± 68	0	0
192	199	4900	2960 ± 140	1570 ± 100	18 ± 10	388 ± 62	0	18 ± 13
208	216	6590	3520 ± 150	2010 ± 115	25 ± 12	383 ± 62	0	12 ± 12
221	234	7360 ± 131	3250 ± 110	1910 ± 88	17 ± 9	666 ± 70	18 ± 10	6 ± 6
241	254	9560	4350 ± 136	3440 ± 150	25 ± 9	1320 ± 122	17 ± 12	0
261	273	12,100	4750 ± 140	2420 ± 100	26 ± 10	1030 ± 76	0	17 ± 10
281	294	13,100 ± 170	5200 ± 140	2750 ± 103	44 ± 12	1220 ± 85	28 ± 12	0
300	313	14,500	5810	2900 ± 104	29 ± 11	1350 ± 82	30 ± 12	16 ± 9
321	328	14,900	6180 ± 200	3360 ± 115	66 ± 23	1540 ± 97	18 ± 10	9 ± 9
341	348	18.400	6960	3680 ± 160	18 ± 13	1710 ± 130	18 ± 13	0
362	373	17,500	6870 ± 180	3960 ± 128	44 ± 14	2080 ± 123	13 ± 9	24 ± 12
281	394	18.000 ± 210	7190 ± 163	3860 ± 125	22 ± 9	2100 ± 102	26 ± 12	16 ± 9
401	414	20,400 ± 220	7760	3890 ± 120	8 ± 5	2120 ± 116	6 ± 6	24 ± 18
421	433	20,500 ± 220	7740	3890 ± 128	36 ± 13	1830 ± 101	45 ± 16	5 ± 5
441	453	20,100 ± 210	8350 ± 180	4120 ± 126	86 ± 19	2100 ± 115	32 ± 13	6 ± 6
461	474	24,300 ± 240	8640	4260 ± 120	46 ± 13	2170 ± 110	35 ± 13	16 ± 9
501	508	19,900 ± 280	8950 ± 237	4520 ± 174	42 ± 16	2220 ± 156	52 ± 20	0
516	524	18,500 ± 284	9120	4360 ± 165	68 ± 21	2270 ± 141	29 ± 17	18 ± 13
533	540	18,100 ± 270	9810	4440 ± 182	49 ± 18	2280 ± 151	27 ± 16	0
549	556	17,400 ± 270	9500	4250 ± 169	48 ± 18	2250 ± 148	16 ± 11	18 ± 13
565	571	19,300 ± 290	9630 ± 246	4390 ± 187	64 ± 23	2240 ± 141	39 ± 22	13 ± 13
581	588	22,100 ± 290	10,900	4680 ± 180	62 ± 20	2690 ± 170	39 ± 19	11 ± 11
596	604	18,800 ± 280	10,700	4720 ± 184	58 ± 20	2060 ± 149	9 ± 9	10 ± 10
629	636	18,500 ± 260	11,100	4960 ± 182	61 ± 60	1840 ± 133	20 ± 14	
645	652	10,500 ± 200	9100 ± 250	4640 ± 170	38 ± 15	1230 ± 109	49 ± 22	10 ± 10
655	667	13,300 ± 170	11,900 ± 222	5280 ± 145	48 ± 13	1320 ± 88	61 ± 18	16 ± 9
681	694	11,800 ± 160	13,000	5710 ± 145	63 ± 14	838 ± 70	34 ± 14	0
701	714	8720 ± 140	12,900 ± 223	6100 ± 147	86 ± 17	511 ± 53	55 ± 16	23 ± 10
714	727	9380 ± 140	18,600 ± 273	8080 ± 172	52 ± 14	448 ± 51	24 ± 12	23 ± 10
721	734	9200 ± 140	18,700	8180 ± 166	85 ± 17	411 ± 51	33 ± 13	26 ± 12

TABLE A-2
(continued)

Flight Time Interval (sec) From	To	Average of Channels 1 & 5	Channel 7	Channel 3	Channel 6	Channel 2	Channel 8	Channel 4
741	754	16,300 ± 200	56,500 ± 430	22,100 ± 292	167 ± 23	543 ± 54	205 ± 30	115 ± 24
754	767	19,300 ± 220	Saturation	27,400 ± 356	469 ± 41	930 ± 69	342 ± 42	230 ± 32
761	774	31,400 ± 280	Saturation	52,300 ± 541	309 ± 55	1590 ± 88	764 ± 51	393 ± 44
774	787	Saturation	Saturation	Saturation	1280 ± 67	3960 ± 140	1940 ± 96	991 ± 70
794	807	19,300 ± 210	Saturation	Saturation	346 ± 53	1390 ± 85	730 ± 70	473 ± 45
801	814	16,100 ± 190	44,000 ± 430	32,400 ± 380	270 ± 34	535 ± 55	294 ± 32	187 ± 31
814	827	2010 ± 220	7250 ± 160	4320 ± 239	8 ± 6	42 ± 15	18 ± 10	34 ± 14
821	834	359 ± 88	1730 ± 34	919 ± 60		6 ± 6	0	

TABLE A-3

COUNTING RATES of DETECTORS on FLIGHT 2021

Flight Time Interval (sec) From	To	Average of Channels 1 & 5	Channel 7	Channel 3	Channel 6	Channel 2	Channel 8	Channel 4
137	144	667 ± 60	146 ± 31	116 ± 30	17 ± 12	34 ± 20	9	12
152	160	2750	516 ± 53	332 ± 55	28 ± 14	155 ± 34	0	5
169	176	5930 ± 172	906 ± 71	433 ± 62	7	230 ± 23	12	4
201	208	10,600 ± 282	1440 ± 109	713 ± 70	15	636 ± 69	4	0
217	224	12,500 ± 294	1720 ± 109	827	15	815 ± 64	8	8
233	240	15,400 ± 313	1990 ± 122	940 ± 80	23	1020 ± 63	10	7
249	256	19,500	2050 ± 108	1035	26	1470 ± 69	14	5
261	274	23,300	2320 ± 88	1193 ± 67	24 ± 10	1920 ± 93	23	9
301	314	36,200 ± 360	2670 ± 98	1180 ±	44 ± 13	1940 ± 96	8	2
321	334	25,600	2850 ± 100	1370 ± 73	34	2010 ± 82	9	4
341	354	26,900	3140 ± 109	1450	60 ± 15	2150 ± 96	14	14
361	374	36,900	3080 ± 113	1419	50	2250 ± 1[illegible]	27	6
381	394	23,600	3270 ± 109	1620 ± 86	64 ± 16	2360 ± 91	29 ± 15	13
401	414	28,100	3420 ± 111	1520	23	2570 ± 139	23	8
414	422	34,800	3640 ± 154	1580 ± 101	46	2500 ± 144	30	3
433	440	26,400	3520 ± 152	1600	20	2200 ± 158	12	8
443	448	29,100	3330 ± 158	1470	33	1950 ± 121	11	11
447	455	18,200	3650 ± 154	1430	39	2040 ± 152	14	7
457	464	23,100	2990 ± 138	1580	45	1830 ± 135	8	11
463	471	21,500	3420 ± 148	1460	58 ± 19	2130 ± 154	23	27
472	480	29,700	3370 ± 147	1280 ± 91	52	2000 ± 93	18	14
488	496	36,600	3650 ± 136	1400	39	2110 ± 127	21	17 ± 14
504	512	31,900	3380 ± 144	1590 ± 102	31 ± 14	2130 ± 156	3	14
521	527	22,200	3570 ± 159	1370 ± 98	60 ± 20	1680 ± 139	15	0
536	543	31,500	3620 ± 154	1257	62	1460 ± 130	31 ± 17	0
553	560	14,700	3990 ± 162	1450 ± 86	53	1530 ± 119	23	0
560	566	34,700	3490 ± 163	1310 ± 115	59 ± 22	1830 ± 87	17	3
568	576	36,900	3750 ± 137	1230	13	1820 ± 113	20	0
575	582	16,600	3870 ± 158	1360	23 ± 13	1770 ± 111	9	6
585	591	26,000	3540 ± 142	1340	13	1540 ± 98	16	19 ± 10

TABLE A-3
(continued)

Flight Time Interval (sec) From	To	Average of Channels 1 & 5	Channel 7	Channel 3	Channel 6	Channel 2	Channel 8	Channel 4
592	599	22,000	3600 ± 147	1280	46	1400 ± 89	11	7
601	606	20,500 ± 332	3720 ± 162	1090 ± 100	11 ± 5	1390 ± 113	8	8
617	623	19,600	3300 ± 161	1220	13 ± 5	1560 ± 128	29 ± 16	8
633	639	20,200	3460 ± 151	1180 ± 85	17 ± 6	1330 ± 110	11	0
649	656	20,100	3420 ± 144	1038	15 ± 6	1260 ± 102	8	12
681	687	17,000	3320 ± 153	934 ± 78	15 ± 6	1340 ± 110	8	0
697	703	18,500	3660 ± 155	1100	29 ± 10	1250 ± 137	7	7
705	710	17,220 ± 268	3260 ± 129	998	29 ± 10	1140 ± 98	18	7
713	719	16,900	3729 ± 158	1010	39 ± 11	1070 ± 79	28	0
729	735	18,100	3589 ± 154	1010	45 ± 12	1100 ± 113	13	13 ± 11
745	752	12,700	3490 ± 138	947	23 ± 9	704 ± 81	15	9
761	774	8230	2960 ± 105	858 ± 55	26 ± 7	544 ± 62	21	6
781	793	4860	2664 ± 97	951	15 ± 5	291 ± 42	21	6
801	813	2843 ± 91	3360 ± 114	1230 ± 65	26 ± 7	103 ± 17	7	7
821	834	1670	3570 ± 110	1760 ± 76	18 ± 6	47 ± 16	19 ± 10	0
841	853	1080	3450 ± 109	2010 ± 85	13 ± 5	23 ± 12	17	20
853	859	399 ± 43	1520 ± 100	732 ± 65	13 ± 7	16 ± 11	4	0
863	869	312 ± 40	697 ± 69	307 ± 45	27 ± 10	0	0	0

TABLE A-4

COUNTING RATES of DETECTORS on FLIGHT 2024

Flight Time Interval (sec) From	To	Average of Channels 1 & 5	Channel 7	Channel 3	Channel 6	Channel 2	Channel 8
143	154	953 ± 62	124 ± 28	77 ± 25		0	0
168	174	2560 ± 97	246	59 ± 19		200 ± 41	4 ± 4
188	194	1410 ± 140	479	168		245 ± 44	0
206	217	7550 ± 128	749 ± 45	117 ± 21		557 ± 47	19 ± 7
229	241	12,150 ± 165	996	140 ± 21		815 ± 57	11 ± 5
254	260	12,600	1250	181	41 ± 16	984 ± 60	12 ± 5
277	290	17,300 ± 200	1530 ± 67	312	14	1020 ± 65	40 ± 10
301	313	19,900	1840	261 ± 30	20	1160 ± 68	11 ± 5
325	337	19,800	1930	228	37	1380 ± 74	13 ± 5
349	361	30,800 ± 262	2190 ± 79	297	54	1500 ± 55	8 ± 4
373	386	20,400	2100	359 ± 38	48	1520 ± 79	10 ± 5
402	405	22,300 ± 400	2390 ± 146	296	8	1570 ± 129	6 ± 6
422	433	25,400 ± 240	2490 ± 82	392 ± 40	43	1630 ± 82	13 ± 5
446	457	17,300	2830	380	30	2100 ± 100	20 ± 7
470	481	37,700 ± 320	2670 ± 96	373	90 ± 24	2180 ± 108	29 ± 9
481	493	37,500	3400	487 ± 41	46	2130 ± 97	16 ± 6
495	507	30,800	3430	479	63	1310 ± 97	21 ± 6
508	520	27,000	3400 ± 110	534 ± 42	28	2270 ± 101	38 ± 10
521	532	28,500	3690	546	49	2290 ± 104	14 ± 6
536	546	35,800 ± 311	3940	537	15	2110 ± 104	19 ± 7
547	558	27,700	4200	553	22	2080 ± 90	20 ± 7
560	572	18,600 ± 205	4440	696 ± 50	62	2290 ± 91	20 ± 7
574	586	25,000 ± 260	4500 ± 150	772 ± 50	36 ± 11	2160 ± 90	25 ± 8
588	600	25,400 ± 240	5100	1020 ± 60	34 ± 12	1840 ± 84	23 ± 7
602	613	26,300	5830 ± 160	1430	9 ± 6	1800 ± 81	23 ± 7
614	626	26,700	7090 ± 160	1910 ± 89	10 ± 7	1730 ± 75	33 ± 8
628	638	22,900 ± 260	8300	2880 ± 108	16 ± 9	1380 ± 75	39 ± 10
640	651	20,200	9560 ± 186	3260 ± 104	26 ± 10	1000 ± 58	54 ± 10
653	665	27,500	31,400 ± 340	10,660 ± 187	82 ± 18	1540 ± 75	162 ± 19
666	678	Saturation	Saturation	17,700	124 ± 23	2100 ± 94	548 ± 49

TABLE A-4
(continued)

Flight Time Interval (sec) From	To	Average of Channels 1 & 5	Channel 7	Channel 3	Channel 6	Channel 2	Channel 8
679	692	43,200 ± 130	48,100 ± 400	13,740 ± 216	119 ± 22	1820 ± 82	394 ± 39
693	705	22,000	21,000 ± 302	6650 ± 148	43 ± 14	1220 ± 76	162 ± 24
707	717	15,300 ± 200	10,200 ± 224	3690	47 ± 14	538 ± 49	51 ± 13
719	730	7560 ± 130	5350 ± 153	1690 ± 72	25 ± 9	242 ± 32	30 ± 10
732	743	4960	4620	1660	9	184 ± 27	22 ± 8
745	756	2620	3350	1200	16 ± 11	60 ± 16	11 ± 6
758	769	1340 ± 56	2460 ± 94	797 ± 54		35 ± 12	2 ± 2
771	782	491	1240	483		8 ± 6	0
784	795	81 ± 13	176 ± 26	96 ± 18		0	0

TABLE A-5

COUNTING RATES of DETECTORS on FLIGHT 2027

Flight Time Interval (sec) From	To	Average of Channels 1 & 5	Channel 7	Channel 3	Channel 6	Channel 2	Channel 8	Channel 4
200	207	6670 ± 282	255 ± 59	112 ± 39	37 ± 18		2 ± 2	
213	220	6230 ± 174	546 ± 71	103 ± 31				
233	239	8960 ± 229	790 ± 85	108 ± 36		221	4 ± 3	3 ± 2
265	271	10,470 ± 226	1670 ± 94	169 ± 48	36 ± 21	246	3 ± 2	4 ± 3
281	287	11,960 ± 282	1320 ± 95	111 ± 39		397	2 ± 2	2 ± 2
297	303	13,750 ± 285	1520 ± 102	120 ± 38		493	8 ± 3	3 ± 2
313	320	14,200 ± 277	1518 ± 111	82 ± 33	41 ± 20	695	2 ± 2	2 ± 2
320	326	12,080 ± 264	1840 ± 130	137 ± 38		522	3 ± 2	3 ± 2
335	341	8830 ± 248	1070 ± 112	153 ± 46		389	2 ± 2	2 ± 2
345	351	15,200 ± 263	1700 ± 133	148 ± 39		441	2 ± 2	3 ± 2
361	367	17,100 ± 384	2090 ± 134	137 ± 41		497	2 ± 2	2 ± 2
377	383	12,100 ± 219	1840 ± 124	138 ± 38	8 ± 8	511	4 ± 3	
393	399	12,140 ± 236	1960 ± 124	98 ± 32		470	4 ± 3	2 ± 2
409	415	12,400 ± 267	2130 ± 143	109 ± 36		386	10 ± 4	
425	431	11,300 ± 273	2060 ± 131	97 ± 32	38 ± 19	497	3 ± 2	2 ± 2
441	447	10,400 ± 258	2090 ± 139	213 ± 47		520	2 ± 2	2 ± 2
457	463	11,430 ± 300	2210 ± 130	127 ± 36		362	6 ± 3	
473	478	10,170 ± 311	2220 ± 130	158 ± 47	18 ± 13	436	3 ± 3	
489	495	8360 ± 240	2350 ± 147	155 ± 46		475	4 ± 3	4 ± 3
505	517	6760 ± 257	2270 ± 137	105 ± 33		425	6 ± 3	4 ± 3
521	527	6070 ± 207	2120 ± 126	113 ± 39		341	2 ± 2	
537	543	5370 ± 185	2020 ± 145	132 ± 40	9 ± 9	148	3 ± 2	2 ± 2
553	559	4370 ± 132	1930 ± 142	197 ± 48	8 ± 8	213	5 ± 3	
569	574	3850 ± 188	1580 ± 162	169 ± 48		140	4 ± 3	
585	591	2760 ± 129	1790 ± 112	136 ± 48	17 ± 12	63		
601	607	4100 ± 116	1390 ± 102	150 ± 39		63	3 ± 2	
617	623	1380 ± 123	1790 ± 123	238 ± 50	6 ± 6	128	4 ± 3	3 ± 2
633	639	1360 ± 94	1160 ± 84	172 ± 49	31 ± 15	13 ± 13		2 ± 2
649	655	1390 ± 175	1360 ± 112	173 ± 61		38	8 ± 3	3 ± 2
656	667	1200 ± 89	1200 ± 82	245 ± 34	4 ± 4	39	2 ± 1	2 ± 1

TABLE A-5
(continued)

Flight Time Interval (sec) From	To	Average of Channels 1 & 5	Channel 7	Channel 3	Channel 6	Channel 2	Channel 8	Channel 4
665	671	1100 ± 102	1110 ± 117	298 ± 50	8 ± 8	13 ± 13	3 ± 2	
673	684	1220 ± 103	1350 ± 71	514 ± 70	19 ± 10	22		3 ± 2
681	687	1350 ± 112	1220 ± 102	540 ± 68	30 ± 15		2 ± 2	2 ± 2
689	700	1040 ± 100	1290 ± 117	573 ± 55	12 ± 7	26	2 ± 1	1 ± 1
704	717	1540 ± 97	2860 ± 113	94 ± 85	8 ± 8	21		2 ± 1
721	732	1930 ± 111	4090 ± 121	1946 ± 109	4 ± 4	47	2 ± 1	1 ± 1
739	735	2090 ± 177	3350 ± 155	1367 ± 151	12 ± 9	25	3 ± 2	
737	741	973 ± 121	2410 ± 145	1110 ± 157		31	3 ± 2	
741	748		775 ± 66	402 ± 24				

TABLE A-6

COUNTING RATES of DETECTORS on FLIGHT 2042

Flight Time Interval (sec) From	To	Channel 1	Channel 5	Channel 7	Channel 3	Channel 6	Channel 2	Channel 8	Channel 4
161	173	1500 ± 95	1870 ± 106	97 ± 18	4 ± 4	18 ± 6	50 ± 12	9 ± 4	11 ± 5
182	194	2010	2910 ± 116	160	26 ± 10		198 ± 14	2 ± 2	9 ± 4
201	213	3620	4580 ± 164	331 ± 34	35 ±	23 ± 7	332 ± 26	17 ± 6	11 ± 4
222	233	4360	5860 ± 174	490	45 ± 13	24 ± 7	399 ± 29	21 ± 6	17 ± 6
241	253	5130	8100 ± 194	548	31	15 ± 5	490 ± 32	18 ± 6	16 ± 6
261	270	5330	9760 ± 285	667	23	30 ± 9	601 ± 42	38 ± 11	18 ± 7
282	293	6510	10,400 ± 231	734	43	24 ± 7	758 ± 40	8 ± 4	11 ± 5
301	313	6580	11,680 ± 246	858 ± 57	40	16 ± 6	734 ± 40	13 ± 5	2 ± 2
321	333	6790	9670	1016	52	25 ± 7	769 ± 40	9 ± 4	12 ± 5
341	353	7060	11,900 ± 244	1190 ± 72	28		893 ± 44	17 ± 6	11 ± 5
362	374	7660	10,900	1220	31		958 ± 45	17 ± 6	21 ± 7
382	392	8060 ± 212	11,900 ± 258	1250	16 ± 7		944 ± 45	15 ± 6	26 ± 8
401	413	6930	12,000 ± 251	1330	32		879 ± 43	8 ± 4	6 ± 4
422	434	7030	12,160	1390	40		872 ± 43	15 ± 6	26 ± 7
441	453	7400	10,600	1540 ± 76	66 ± 16	18 ± 6	994 ± 47	4 ± 3	11 ± 5
461	473	6620	11,200 ± 242	1540	34	30 ± 8	879 ± 44	18 ± 6	28 ± 8
480	491	6110	11,300	1510	26	16 ± 6	922 ± 45	18 ± 6	11 ± 5
501	513	6500	11,450	1680	39 ± 12	22 ± 7	922 ± 44	25 ± 7	21 ± 7
521	533	6610	10,700	1570	31	38 ± 9	829 ± 42	31 ± 8	15 ± 6
541	552	5660 ± 192	8680	1520	48	27 ± 8	879 ± 45	11 ± 5	7 ± 4
601	612	5330	7720	1340	43	26 ± 7	722 ± 40	21 ± 9	11 ± 5
621	633	5170	7900	1200 ± 68	18 ± 8	38 ± 9	793 ± 41	15 ± 6	16 ± 6
641	653	4420 ± 146	7390 ± 207	1120	18 ± 8	12 ± 5	616 ± 36	33 ± 8	4 ± 3
661	673	4240	6070	1010	17	38 ± 9	628 ± 36	26 ± 8	8 ± 4
681	693	3340	4900	776 ± 42	40 ± 12	21 ± 6	496 ± 31	15 ± 6	11 ± 5
701	713	2620	4200	586	19	17 ± 6	332 ± 26	6 ± 4	2 ± 2
721	733	1820 ± 100	2390 ± 119	372	32	28 ± 8	222 ± 24	6 ± 4	11 ± 5
741	752	958 ± 78	1410	336 ± 27	9 ± 6	28 ± 8	106 ± 16	7 ± 4	5 ± 4
761	774	527 ± 100		260 ± 22	32 ± 8	22 ± 6	30 ± 8	2 ± 2	
781	794	162 ± 50		101 ± 14	34 ± 8	14 ± 5	8 ± 4	6 ± 4	
801	814	65 ± 30		30 ± 8	22 ± 6	16 ± 6	19 ± 6	8 ± 4	

TABLE A-7

Jason Flight 2019

Flight Time (min)	West Longitude (deg)	North Latitude (deg)	Rocket Altitude (KM)	Magnetic Intensity (Gauss)	Log I	Altitude* 75° West (KM)	Altitude** S. Hemis. (KM)
2.00	75.41	52.60	282				
2.50	75.39	52.89	367				
3.00	75.36	53.17	444				
3.50	75.33	53.45	513	0.4300	10.228	510	139
4.00	75.31	53.72	576	0.4169	10.218	573	259
4.50	75.28	53.99	631	0.4054	10.206	628	318
5.00	75.26	54.25	679	0.3954	10.195	676	366
5.50	75.24	54.51	719	0.3872	10.182	717	409
6.00	75.21	54.77	753	0.3806	10.170	751	443
6.50	75.19	55.03	780	0.3753	10.156	778	468
7.00	75.17	55.28	800	0.3710	10.142	799	486
7.50	75.15	55.53	813	0.3680	10.128	812	501
8.00	75.13	55.79	820	0.3660	10.112	819	508
8.50	75.11	56.04	819	0.3651	10.096	819	510
9.00	75.08	56.29	812	0.3654	10.080	812	503
9.50	75.06	56.54	798	0.3667	10.062	798	487
10.00	75.04	56.80	778	0.3691	10.043	777	463
10.50	75.02	57.05	750	0.3726	10.022	750	444
11.00	75.00	57.31	716	0.3772	9.999	716	412
11.50	74.98	57.57	674	0.3833	9.976	675	372
12.00	74.96	57.83	626	0.3910	9.953	626	326
12.50	74.93	58.10	570	0.4001	9.929	571	274
13.00	74.91	58.38	507	0.4108	9.903	508	228
13.50	74.89	58.65	444				
14.00	74.87	58.94	359				

NOTE: Single and double asteriks refer to last two columns of Tables 7 through 12

*Rocket altitude transformed along lines of constant B_o and I values to the meridian plane at 75° West longitude

**Altitude in southern hemisphere where magnetic field intensity (along local magnetic line of force) is same as that at the position of the rocket.

TABLE A-8

Jason Flight 2021

Flight Time (min)	West Longitude (deg)	North Latitude (deg)	Rocket Altitude (KM)	B	Log I	Altitude* 75° West (KM)	Altitude** S. Hemis. (KM)
2.00	75.99	37.66	305			300	
2.50	76.17	37.43	389			384	85
3.00	76.35	37.21	465			458	159
3.50	76.52	36.99	534	0.4281	10.254	526	234
4.00	76.69	36.77	596	0.4154	10.247	588	313
4.50	76.85	36.56	650	0.4046	10.239	642	374
5.00	77.01	36.35	697	0.3951	10.230	688	421
5.50	77.17	36.14	737	0.3875	10.220	728	459
6.00	77.32	35.94	771	0.3813	10.210	760	492
6.50	77.48	35.74	797	0.3762	10.200	782	521
7.00	77.63	35.53	816	0.3724	10.188	804	541
7.50	77.78	35.33	829	0.3698	10.175	816	550
8.00	77.92	35.13	835	0.3683	10.162	822	560
8.50	78.07	34.93	834	0.3678	10.149	820	558
9.00	78.22	34.73	826	0.3684	10.134	810	557
9.50	78.37	34.52	812	0.3701	10.118	796	542
10.00	78.51	34.32	790	0.3730	10.102	774	521
10.50	78.66	34.12	732	0.3820	10.080	744	476
11.00	78.81	33.91	727	0.3821	10.064	700	470
11.50	78.96	33.70	684	0.3886	10.043	668	430
12.00	79.11	33.49	636	0.3969	10.022	618	389
12.50	79.26	33.27	579	0.4066	9.999	564	345
13.00	79.41	33.05	516	0.4182	9.974	496	274
13.50	79.57	32.83	445			422	
14.00	79.72	32.60	366			346	

TABLE A-9

Jason Flight 2024

Flight Time (min)	West Longitude (deg)	North Latitude (deg)	Rocket Altitude (KM)	B	Log I	Altitude* 75° West (KM)	Altitude** S. Hemis. (KM)
2.50	75.23	36.81	389			386	81
3.00	75.13	36.44	463			462	158
3.50	75.02	36.08	530	0.4251	10.200	530	223
4.00	74.92	35.73	589	0.4123	10.184	588	282
4.50	74.83	35.39	641	0.4011	10.168	642	334
5.00	74.73	35.05	686	0.3912	10.151	686	377
5.50	74.64	34.71	724	0.3832	10.133	726	413
6.00	74.55	34.38	755	0.3767	10.116	740	444
6.50	74.46	34.05	780	0.3714	10.098	784	466
7.00	74.37	33.72	797	0.3673	10.079	802	483
7.50	74.28	33.39	808	0.3642	10.060	814	495
8.00	74.19	33.07	813	0.3623	10.040	820	500
8.50	74.11	32.74	810	0.3614	10.019	816	497
9.00	74.02	32.41	801	0.3616	9.997	808	486
9.50	73.93	32.08	785	0.3629	9.973	796	468
10.00	73.85	31.75	763	0.3652	9.948	774	442
10.50	73.76	31.42	733	0.3685	9.921	744	411
11.00	73.68	31.08	697	0.3728	9.892	708	374
11.50	73.59	30.74	654	0.3789	9.865	664	333
12.00	73.51	30.40	604	0.3861	9.836	612	285
12.50	73.42	30.05	547	0.3950	9.807	556	239
13.00	73.33	29.69	483	0.4056	9.778	496	167
13.50	73.24	29.33	411	0.4185	9.749	428	97
14.00	73.15	28.96	332			340	27

TABLE A-10

Jason Flight 2027

Flight Time (min)	West Longitude (deg)	North Latitude (deg)	Rocket Altitude (KM)	Magnetic Intensity (Gauss)	Log I	Altitude* 75° West (KM)	Altitude** S. Hemis. (KM)
0.00	76.25	39.17	-172				
0.50	76.01	37.86	- 57				
1.00	75.78	38.56	49			45	
1.50	75.56	37.27	147			144	
2.00	75.35	36.99	236			235	
2.50	75.14	36.72	318			317	
3.00	74.94	36.45	392			392	
3.50	74.74	36.19	458			459	
4.00	74.55	35.93	516	0.4267	10.189	519	194
4.50	74.37	35.67	568	0.4157	10.178	571	250
5.00	74.18	35.42	612	0.4061	10.167	616	295
5.50	74.01	35.17	649	0.3981	10.153	654	330
6.00	73.83	34.93	679	0.3914	10.142	684	358
6.50	73.66	34.68	701	0.3860	10.128	708	378
7.00	73.48	34.44	717	0.3823	10.115	725	392
7.50	73.31	34.19	726	0.3798	10.100	734	399
8.00	73.14	33.95	728	0.3784	10.084	737	400
8.50	72.98	33.70	723	0.3781	10.068	733	392
9.00	72.81	33.46	711	0.3790	10.050	722	378
9.50	72.64	33.21	692	0.381	10.031	704	358
10.00	72.47	32.97	666	0.3848	10.013	679	329
10.50	72.31	32.72	633	0.3896	9.993	647	293
11.00	72.14	32.46	593	0.3957	9.972	608	252

Table A-1d (continued)

11.50	71.97	32.21	546	0.4033	9.951	561	205
12.00	71.80	31.95	491			507	
12.50	71.62	31.68	429			446	
13.00	71.45	31.41	360			378	
13.50	71.27	31.13	283			301	
14.00	71.09	30.85	197			217	
14.50	70.90	30.56	104			125	
15.00	70.71	30.26	3				
15.50	70.51	29.95	-107				
16.00	70.31	29.62	-226				

TABLE A-11

Jason Flight 2042

Flight Time (min)	West Longitude (deg)	North Latitude (deg)	Rocket Altitude (KM)	B	Log I	Altitude* 75° West (KM)	Altitude** S. Hemis. (KM)
2.50	75.01	37.45	299			296	
3.00	74.80	37.14	379			380	
3.50	74.60	36.84	452			454	
4.00	74.40	36.54	517	0.4284	10.229	520	191
4.50	74.21	36.25	575	0.4159	10.217	580	258
5.00	74.02	35.97	626	0.4051	10.204	632	309
5.50	73.83	35.68	670	0.3956	10.190	676	349
6.00	73.65	35.40	707	0.3877	10.176	712	380
6.50	73.48	35.12	737	0.3816	10.161	746	407
7.00	73.30	34.85	760	0.3767	10.147	768	427
7.50	73.13	34.57	776	0.3728	10.131	784	443
8.00	72.95	34.30	785	0.3702	10.115	796	451
8.50	72.78	34.03	788	0.3686	10.098	800	452
9.00	72.61	33.75	784	0.3681	10.080	796	445
9.50	72.45	33.48	773	0.3688	10.061	786	434
10.00	72.28	33.20	755	0.3705	10.041	770	415
10.50	72.11	32.92	731	0.3732	10.019	744	390
11.00	71.94	32.64	699	0.3770	9.996	714	353
11.50	71.77	32.36	661	0.3827	9.973	676	313
12.00	71.60	32.07	616	0.3895	9.950	632	267
12.50	71.43	31.78	563	0.3978	9.926	582	214
13.00	71.26	31.48	503	0.4074	9.900	524	155
13.50	71.08	31.18	436			456	
14.00	70.90	30.87	362			382	

TABLE A-12

Javelin I

Flight Time (min)	West Longitude (deg)	North Latitude (deg)	Rocket Altitude (KM)	B	Log I	Altitude* 75° West (KM)	Altitude** S. Hemis. (KM)
1.00	75.46	37.78	76			76	
1.50	75.08	37.50	189			188	
2.00	74.71	37.22	294			294	
2.50	74.37		392				
3.00		36.68				486	
3.50	73.72	36.43	565	0.4204	10.220	570	225
4.00	73.42	36.18	641	0.4025	10.219	648	309
4.50	73.13	35.93	710	0.3886	10.211	718	379
5.00	72.85	35.69	772	0.3771	10.203	782	436
5.50	72.58	35.44	828	0.3669	10.193	840	490
6.00	72.31	35.20	877	0.3581	10.183	890	542
6.50	72.06	34.96	920	0.3503	10.173	934	581
7.00	71.81	34.73	957	0.3436	10.162	970	618
7.50	71.56	34.49	987	0.3378	10.151	1004	651
8.00	71.32	34.25	1011	0.3334	10.138	1030	675
8.50	71.09	34.05	1029	0.3301	10.128	1048	685
9.00	70.85	33.78	1041	0.3275	10.112	1062	693
9.50	70.62	33.54	1047	0.3258	10.098	1068	694
10.00	70.40	33.31	1046	0.3250	10.083	1068	690
10.50	70.17	33.07	1040	0.3249	10.068	1064	682
11.00	69.95	32.83	1027	0.3258	10.051	1052	663
11.50	69.72	32.59	1008	0.3273	10.033	1032	647
12.00	69.50	32.34					
12.50	69.27	32.10	952	0.3335	9.995	980	588

TABLE A 12 (continued)

Javelin I

Flight Time (min)	West Longitude (deg)	North Latitude (deg)	Rocket Altitude (KM)	B	Log I	Altitude* 75° West (KM)	Altitude** S. Hemis. (KM)
13.00	69.04	31.85	914	0.3379	9.974	944	545
13.50	68.82	31.59	870	0.3434	9.952	902	498
14.00	68.58	31.33	820	0.3499	9.929	852	438
14.50	68.35	31.07	763	0.3576	9.903	796	380
15.00	68.11	30.80	700	0.3662	9.874	734	317
15.50	67.87	30.52	630	0.3769	9.849	662	241
16.00	67.62	30.24	553	0.3891	9.823	590	163
16.50	67.36	29.95	468	0.4046	9.800	506	
17.00	67.10	29.65	377			416	
17.50	66.83	29.35	279			320	
18.00	66.54	29.03	173			216	
18.50	66.25	28.70	59				

DISTRIBUTION

No. Cys

HEADQUARTERS USAF

1	Hq USAF (AFCOA), Wash 25, DC
1	Hq USAF (AFDAP), Wash 25, DC
1	Hq USAF (AFORQ), Wash 25, DC
1	Hq USAF (AFRDT), Wash 25, DC
1	Hq USAF (AFRDT-NU-1), Wash 25, DC
1	Hq USAF (AFCIN), Wash 25, DC
1	Hq USAF (AFTAC), Wash 25, DC
1	USAF Dep IG for Insp (AFCDI-B-3), Norton AFB, Calif
1	USAF Dep IG for Safety (AFINS), Kirtland AFB, N Mex
1	FTD (Library), Wright-Patterson AFB, Ohio
1	AFOAR, ATTN: RRN, Major Munyon, Bldg T-D, Wash 25, DC
	AFCRL, L. G. Hanscom Fld, Bedford, Mass
1	ATTN: Tech Library
1	ATTN: CRZCT, H. P. Gauvin
1	ATTN: Dr. P. Newman
1	AFOSR, ATTN: SREC, Bldg T-D, Wash 25, DC
1	Aeronautical Research Lab, ATTN: RRLO, Mr. Cady, Wright-Patterson AFB, Ohio

MAJOR AIR COMMANDS

	AFSC, Andrews AFB, Wash 25, DC
1	ATTN: SCR
1	ATTN: SCR-2, Maj Berrier
1	AUL, Maxwell AFB, Ala
1	USAFIT (USAF Institute of Technology), Wright-Patterson AFB, Ohio

AFSC ORGANIZATIONS

1	ASD (ASAPRL, Tech Document Library), Wright-Patterson AFB, Ohio
1	DCAS, ATTN: Technical Data Center, AF Unit Post Office, Los Angeles 45, Calif
	BSD (Ballistic Systems Division), AF Unit Post Office, Los

DISTRIBUTION (con't)

No. Cys	
	Angeles 45, Calif
1	ATTN: BSR-VP-3
1	ATTN: BSR
1	SSD (Space Systems Divison), ATTN: Tech Library, AF Unit Post Office, Los Angeles 45, Calif
	ESD, Hanscom Fld, Bedford, Mass
1	ATTN: ESAT
1	ATTN: ESRH
1	ATTN: ESS
1	ATTN: ESF
1	AF Msl Dev Cen (MDGRT), Holloman AFB, N Mex
1	AFFTC (FTFT), Edwards AFB, Calif
1	AFMTC, ATTN: MU-135, Tech Library, Patrick AFB, Fla
1	AEDC (AEOI), Arnold Air Force Station, Tenn
1	APGC (PGAPI), Eglin AFB, Fla
1	RADC, Griffiss AFB, NY
	KIRTLAND AFB ORGANIZATIONS
	AFSWC, Kirtland AFB, N Mex
1	(SWNH)
48	(SWOI)
1	(SWT)
2	(SWRPT, Capt Welch)
1	(SWRPA)
1	(SWRPI, Lt Holly)
1	(SWRPS, Maj Nadler)
1	(SWRJ)
1	(SWRB, Lt Tinney)
1	(SWRP, Maj Allen)
1	US Naval Weapons Evaluation Facility (NWEF) (Code 404), Kirtland AFB, N Mex
	OTHER AIR FORCE AGENCIES
1	Director, USAF Project RAND, ATTN: RAND Library, via: Air Force Liaison Office, The RAND Corporation, 1700 Main Street, Santa Monica, Calif

DISTRIBUTION (con't)

No. Cys	
1	Avn School of Medicine, USAF Aerospace Medical Center, (ATC), Brooks AFB, Tex
	ARMY ACTIVITIES
1	Chief of Research and Development, Department of the Army, ATTN: Lt Col Conarty, Wash 25, DC
1	Commanding Officer, Diamond Ordnance Fuze Laboratories, (ORDTL 06.33), Technical Library, Wash 25, DC
1	Commanding Officer, Chemical Warfare Laboratories, (Library), Army Chemical Center, Md
1	Commander, Army Rocket and Guided Missile Agency (ARGMA), ATTN: Tech Library, Redstone Arsenal, Ala
	Director, Ballistic Research Laboratories, Aberdeen Proving Ground, Md
1	ATTN: Mr. E. O. Baicy
1	ATTN: Library
1	Director, Evans Signal Laboratory, Weapons Effects Section, Belmar, NJ
1	Commanding Officer, US Army Signal Research & Development Laboratory, ATTN: Dr. W. McAfee, Fort Monmouth, NJ
1	Commanding General, White Sands Missile Range (Technical Library), White Sands, N Mex
	NAVY ACTIVITIES
1	Chief of Naval Operations, (OP-36), Department of the Navy, Wash 25, DC
1	Commanding Officer, Naval Research Laboratory, ATTN: Tech Library, Wash 25, DC
1	Commanding Officer, Naval Radiological Defense Laboratory (Technical Info Div), San Francisco 24, Calif
1	Office of Naval Research, ATTN: Dr. W. J. Thaler, Wash 25, DC
	OTHER DOD ACTIVITIES
	Chief, Defense Atomic Support Agency, Wash 25, DC
1	ATTN: Document Library
1	ATTN: Major MacCormac
1	ATTN: Cmdr Ennis
1	Commander, Field Command, Defense Atomic Support Agency (FCAG3, Special Weapons Publication Distribution), Sandia Base, N Mex

DISTRIBUTION (con't)

No. Cys	
1	Director, Weapon Systems Evaluation Group, Room 2E1006, The Pentagon, Wash 25, DC
1	Director, Advanced Research Projects Agency, Department of Defense, ATTN: Lt Col Weidler, The Pentagon, Wash 25, DC
1	Director, Defense Research & Engineering, The Pentagon, Wash 25, DC
10	ASTIA (TIPDR), Arlington Hall Sta, Arlington 12, Va
	AEC ACTIVITIES
1	US Atomic Energy Commission (Technical Reports Library, Mrs. J. O'Leary for DMA), Wash 25, DC
	President, Sandia Corporation, Sandia Base, N Mex
1	ATTN: Document Control Division
1	ATTN: Dr. Tom Cook
1	Chief, Technical Information Service Extension, US Atomic Energy Commission, Box 62, Oak Ridge, Tenn
1	Director, University of California Lawrence Radiation Laboratory, Technical Information Division (Mr. Clovis Craig), P. O. Box 808, Livermore, Calif
1	Director, Los Alamos Scientific Laboratory (Helen Redman, Report Library), P. O. Box 1663, Los Alamos, N Mex
	OTHER
1	Administrator, National Aeronautics and Space Administration, 1520 H Street, NW, Wash 25, DC
1	Director, National Bureau of Standards, Central Radio Propagation Laboratory, Boulder, Colo
1	Central Intelligence Agency (OCR/LY/ILS), Wash 25, DC
1	Institute for Defense Analysis, Room 2B257, The Pentagon, Wash 25, DC
3	OTS, Department of Commerce, Wash 25, DC
1	General Electric - Tempo, ATTN: Dr. Hendrick, 735 State Street, Santa Barbara, Calif
3	Lockheed Missile & Space Division, ATTN: Dr. Meyerott, 3251 Hanover Street, Palo Alto, Calif
1	E. H. Plesset Associates, ATTN: Dr. H. Mayer, 1281 Westwood Blvd, Los Angeles 24, Calif

DISTRIBUTION (con't)

No. Cys	
1	Republic Aviation Corporation (MSD), ATTN: Mr. H. Rosner, 223 Jericho Turnpike, Mineola, Long Island, NY
1	General Dynamics/Convair, ATTN: Dr. D. Hamlin, 3165 Pacific Highway, San Diego 12, Calif
1	University of Chicago, Institute of Air Weapons Research, Chicago 37, Ill THRU ASD (WWRP Mr. Gard), Wright-Patterson AFB, Ohio
1	State University of Iowa, ATTN: Dr. J. Van Allen, Iowa City, Iowa
1	Stanford University, ATTN: Dr. R. Helliwell, Radio Science Lab, Stanford, Calif
1	Stanford Research Institute, ATTN: Dr. Allen Peterson, Menlo Park, Calif
1	Official Record Copy (SWRPA, Lt Schiff)